University of Warsaw

Spatiotemporal Light Manipulation for Nonlinear Microscopy

PhD Thesis

Paweł Szczypkowski

Supervisors:
Dr Radek Łapkiewicz & Prof. Tadeusz Stacewicz

November 25, 2025

Preface

"I wish that I was more important to you than physics.."

I dedicate this thesis to the most beloved person who said it. Assuring – she is more important.

Streszczenie

Niniejsza praca prowadzi czytelnika przez współczesną optyczną mikroskopię nieliniową. Najpierw przedstawia ogólne wyzwania w mikroskopii oraz zarysowuje istotne osiągnięcia w dziedzinach mikroskopii nadrozdzielczej i obrazowania przez ośrodki rozpraszające. Następnie prezentuje powszechnie stosowaną skaningową mikroskopię dwu-fotonową, wraz z opisem mikroskopu zbudowanego na bazie projektu Benjamina Judkewitza. Mikroskop umożliwia skanowanie z szybkością 30 klatek na sekundę, oraz pozwala na skanowanie wiązką Bessela czy zastosowanie techniki "Image Scanning Microscopy". Mikroskop został wykorzystany w eksperymentach biologicznych do obrazowania in-vivo neuronów wrażliwych na dopaminę.

W dalszej części opisano układ do trójwymiarowej nadrozdzielczej mikroskopii wykorzystującej fluktuacje intensywności fluorescencji (SOFI). Do wzbudzenia wykorzystano ogniskowanie czasowe zapewniające oświetlenie szerokim polem (pole widzenia ok. $50 \times 50 \mu\text{m}^2$) ograniczone w wymiarze wzdłuż osi optycznej obiektywu do $\simeq$2,4 μm. Ograniczenie osiowe poprawiono do $\simeq$1,2 μm korzystając ze wzbudzenia linią i skanowania w jednym wymiarze. Po połączeniu z techniką SOFI uzyskano $\simeq$420 nm rozdzielczości osiowej, co umożliwia wiarygodne rekonstrukcje w trójwymiarze przy ograniczonym wybielaniu poza płaszczyzną obrazowania.

W kolejnej częsci opisano nieliniowe obrazowanie ze wzbudzaniem światłem rozproszonym (NISE). Jest to nowa technika zapewniająca obrazowanie nadrozdzielcze przez ośrodki silnie rozpraszające. Wykorzystanie cząstek lawinowych pozwoliło osiągnąć rozdzielczość 560 nm – ponad dwukrotnie lepszą niż teoretyczny limit 1,2 μm – w warunkach, w których żadna standardowa metoda nie umożliwia obrazowania. Tak zaskakujący rezultat był możliwy dzięki zrozumieniu i wykorzystaniu statystyki intensywności i efektu pamięci dla światła rozproszonego, oraz wysoko nieliniowej odpowiedzi luminescencyjnej. Wzbudzenie wysoko nieliniowych luminoforów przez światło rozproszone, oraz odpowiednie skanowanie prowadzi do nieinwazyjnego i nadrozdzielczego obrazowania obiektów całkowicie ukrytych za mocno rozpraszającymi, nieprzezroczystymi warstwami. Rozwijana dalej technika NISE może mieć

znaczący wpływ zarówno na badania podstawowe, jak i stosowane: od obrazowania biomedycznego i funkcjonalnego (np. badania struktury i aktywności mózgu in-vivo), przez optogenetykę, inteligentne dostarczanie leków za pomocą światła (zlokalizowane uwalnianie związków głęboko w tkankach), terapię fotodynamiczną, obliczenia analogowe za pomocą światła, aż po obróbkę materiałów (gdzie wysokie nieliniowości występują naturalnie).

W całej pracy nacisk został położony na odtwarzalność eksperymentów, dostarczając praktycznych instrukcji budowy i użytkowania poszczególnych układów eksperymentalnych. Łącznie wyniki te pokazują, że nieliniowość otwiera ścieżki do głębszego i nadrozdzielczego obrazowania, a co ważniejsze – stanowi znakomite środowisko dla nowych, ciekawych pomysłów w mikroskopii, które po zastosowaniu mogą mieć duży wpływ na świat w którym żyjemy.

słowa kluczowe: Mikroskopia nieliniowa, Mikroskopia dwufotonowa (TPSM), Ogniskowanie czasowe, SOFI (nadrozdzielcze obrazowanie wykorzystujęce fluktuacje intensywności), Nadrozdzielczość 3D, Obrazowanie głęboko w tkankach, Obrazowanie za pomocą światła rozproszonego, Optyczny efekt pamięci, NISE (nieliniowe obrazowanie ze wzbudzaniem światłem rozproszonym)

Abstract

This thesis guides through contemporary nonlinear optical microscopy. First, it introduces hurdles in microscopy and outlines the relevant works in the fields of super-resolution microscopy and imaging through scattering media. Then it presents the gold-standard technique of two-photon scanning microscopy and a homemade microscope based on Benjamin Judkewitz's design. The microscope can scan at 30 frames per second, and its flexible design supports additional modalities, such as Bessel-beam or two-photon ISM scanning. The microscope was used for end-user experiments for in vivo calcium imaging of dopamine-sensitive neurons.

Next, I describe another custom setup for 3D super-resolution optical fluctuation imaging with temporal focusing, introducing the key concepts of each method. The setup provides axial sectioning of $\simeq$2.4 μm (temporal focusing excitation), improved to $\simeq$1.2 μm in a temporal focusing line-scan variant. When combined with super-resolution optical fluctuation imaging, it delivers $\simeq$420 nm of axial sectioning, enabling reliable volumetric reconstructions with reduced out-of-focus bleaching.

The central part of the thesis is a detailed description of Nonlinear Imaging with Speckle Excitation (NISE). The novel technique provides super-resolution through highly scattering media. The use of avalanching particles enables achieving a resolution of 560 nm, which is more than 2 times better than the 1.2 μm theoretical limit in environments where no standard method can provide imaging. Such a result is possible due to uniting two fundamental properties of scattered light: speckle statistics and the angular memory effect, with a highly nonlinear optical response. This combination yields, rather surprisingly, super-resolution, low-background, non-invasive imaging of objects completely hidden behind a strongly scattering, opaque layer. Further developed NISE has a potential impact across fundamental and applied research: from bio-medical imaging and sensing (in vivo brain structure and activity studies) to optogenetics, smart drug delivery (targeted optical uncaging of drugs deep inside tissues), photodynamic therapy, optical computing, and material processing (where high nonlinearities occur naturally).

Throughout, the thesis emphasises reproducible, custom designs and provides practical build guides and instructions for using the specific experimental setups. Collectively, these results show that nonlinearity offers viable routes to deeper, higher-resolution imaging. More importantly, nonlinear microscopy is a perfect playground for interesting ideas, with significant implications when applied.

Keywords: Nonlinear microscopy, Two-photon microscopy (TPSM), Temporal focusing, SOFI (super-resolution optical fluctuation imaging), 3D super-resolution, Deep imaging, NISE (Nonlinear Imaging with Speckle Excitation)

Contents

List of Abbreviations

2f 2f relay (single lens 1-to-1 imaging)

4f 4f relay (two-lens Fourier imaging system forming conjugate planes)

2P-ISM Two-photon scanning microscope with image scanning microscopy

AOM Acousto-Optic Modulator

AO Adaptive Optics

APD Avalanche Photodiode

CLSM Confocal Laser Scanning Microscope

CW Continuous-Wave (laser operation)

DMD Digital Micromirror Device

DM Deformable Mirror

ESA Excited State Absorption

FLIM Fluorescence Lifetime Imaging Microscopy

FOV Field of View

FPS Frames Per Second

FWHM Full Width at Half Maximum

GFP Green Fluorescent Protein

GSA Ground State Absorption

IR Infrared

ISM Image Scanning Microscopy

MINFLUX MINimum emission FLUX microscopy

NA Numerical Aperture

NIR Near-Infrared

NISE Nonlinear Imaging with Speckle Excitation

OCM Optical Coherence Microscopy

OCT Optical Coherence Tomography

OD Optical Density

PALM PhotoActivated Localization Microscopy

PBS Polarizing Beam Splitter

PMT Photomultiplier Tube

PSF Point Spread Function

ROI Region of Interest

sCMOS scientific Complementary Metal–Oxide–Semiconductor (camera sensor)

SEM Scanning Electron Microscope

SIM Structured Illumination Microscopy

SiPM Silicon Photon Multiplier

SLM Spatial Light Modulator

SNR Signal-to-Noise Ratio

SOFI Super-resolution Optical Fluctuation Imaging

SPAD Single-Photon Avalanche Diode

STED STimulated Emission Depletion microscopy

STORM Stochastic Optical Reconstruction Microscopy

TF Temporal Focusing

TPSM Two-Photon Scanning Microscopy

UV Ultraviolet

WF Wide-Field

Chapter 1

Motivation

Why did I choose microscopy as my field of research, if there is so plenty of extremely interesting areas in optics? My answer is: the generality of microscopy. Microscopy is an interdisciplinary field with broad applications, and its main ideas translate easily to other fields of physics and beyond. I am Pawel Szczypkowski, and I invite you, dear reader, to my story of microscopy, in particular – nonlinear microscopy.

1.1 Nonlinearity as the Key to Advancement

And God said, "Let there be light," and there was light.
God saw that the light was good, and he separated the light from the darkness.

Genesis 1:3-4

This is how I became acquainted with optics during the first lecture, "Podstawy Fizyki III," conducted by Prof. Czesław Radzewicz. From then on, I see light everywhere, and I hazard the statement that light is a subtle foundation of the universe. It shapes our perception, enables life, and stands at the very core of modern physics. Perhaps this fundamental role of light was what drew me to optics during my master's studies and later throughout my PhD.

I fell in love with optics because it lies at an abstraction level that is both intellectually satisfying and experimentally accessible. It allows one to connect mathematical description with physical intuition, and to design, build, and measure with one's own hands. Moreover, optics remains an exceptionally versatile and applied field – bridging fundamental science and technology, from quantum optics to medical imaging.

Yet when one looks for a direction in which to advance the field, it becomes evident that many of the most impactful ideas in optics have already been developed. Optics is, in many respects, a mature science. Its roots reach back to the systematic formulation of geometric optics in the 10th century by Ibn al-Haytham (Alhazen)[1], while the theoretical framework of modern optics was established primarily in the 17th–19th centuries[2]. Throughout this long history, the field evolved within the linear regime, which has been extensively explored and underlies the vast majority of classical optical phenomena and devices.

The situation changed with the invention of the laser in the 1960s [3, 4], which provided light of unprecedented intensity and coherence. Under such conditions, the assumption of linearity broke down, enabling, for example, second harmonic generation [5], and nonlinear optics emerged. This relatively young branch of optics revealed that light can modify the properties of a medium through which it propagates, influence itself while propagating through the medium, and generate new frequencies [6].

Since then, nonlinear optics has become the foundation of many of the most remarkable advances in modern photonics. Frequency mixing allows the generation of almost arbitrary wavelengths [7], expanding the accessible spectral range far beyond natural emission lines. Mode-locking [8] in lasers and nonlinear pulse shaping have enabled femtosecond [9] and attosecond time resolution [10], opening windows into ultraintense laser pulses [11] and ultrafast dynamics, such as electron motion [12]. Nonlinear processes are essential for optical computing [13] or single-photon generation [14] to the joy of everyone working in quantum science. Nonlinear processes also underpin the generation of X-rays [15], the operation of ultrafast spectroscopy [16], and even the patterning of nanoscale structures in lithography, where the nonlinear response of photoresists defines sub-wavelength features [17] and is the foundation of the modern digital world.

In microscopy – the domain of this thesis – nonlinear interactions have also become a cornerstone. Over the last two decades, nonlinear fluorescence microscopy has become a standard tool for deep in vivo imaging [18, 19]. In particular, Raman microscopy [20], second-harmonic generation imaging [21], and other nonlinear modalities such as nonlinear structured illumination [22], nonlinear wavefront shaping [23], or STED [24], and finally two- or three-photon scanning mircoscopy [25, 26] have greatly expanded our ability to probe biological structures and processes beyond the limits of linear techniques.

Nonlinear interactions thus remain a fertile and promising direction for new discoveries in optics. They allow light not only to reveal matter but also to sculpt and manipulate it in fundamentally new ways. My fascination with the richness of nonlinear phenomena, together with the conviction that they still hold vast unexplored potential, motivated me to pursue my research in this direction. The results from Chapter 5 of super-resolution imaging through scattering layers seem to confirm that advancing microscopy through nonlinearity was the correct intuition.

1.2 To Overcome the Light Scattering

When we see an object, we typically rely on scattered light. If you read this text on paper, photons are scattered by the paper's microstructure before reaching your eyes. By contrast, on a display, light from emissive pixels travels directly to the eye, and any additional scattering blurs the content regardless of how well it is written.

I encourage the Reader to make an experiment now. Place a matte, plastic sleeve (attached in the paper version) around a centimetre above the text. Alternatively, place a sheet of paper a few millimetres away from the screen. In both cases, the text becomes illegible. Now press the sleeve against the paper or the paper against the screen, and the letters reappear. The key point of this experiment is that the

scattering medium (the matte sleeve or the paper sheet) scatters light in both cases, but the second situation shows that the information about the text can survive through the diffuser. This observation motivates my specific research problem: can we image the object hidden behind a scattering medium, using nonlinearity, and what resolution can we achieve?

To address this question, an introduction to the field of imaging through scattering media is in place. My personal note is that imaging through scattering media is a central challenge in contemporary optics. From a physics standpoint, the material details of the scattering medium are secondary [27]. Paper, fog, clouds, skin, and bone all scatter light. If the process is deterministic and could be counteracted, the potential impact is obvious. If we could "see" through such media, it could enable non-invasive diagnostics deep within biological tissue, improve detection of early-stage pathologies, allow optical inspection of concealed structures in materials science, and open new avenues in remote sensing and security applications [28–31].

Here, a second demonstration may help clarify the problem. Illuminate the matte sleeve with a laser (included in the printed version), and about 1 meter from the sleeve, observe the random interference of the scattered light – the speckle pattern.

Interest in such speckle patterns for optical imaging first reached astronomy in 1970 [32]. Understanding the speckles and their properties enabled the suppression of atmospheric aberrations in telescopes. The most essential properties of speckle patterns are well studied and well described in classical speckle theory [27]. Such a good understanding of light scattering (more precisely, light propagation in scattering media) enabled, in the 1990s, methods like optical diffusive imaging [33] to show promise for biomedical imaging [34]. However, optical diffusive imaging is not used in microscopy; instead, it is used for imaging larger (millimetre-scale) objects.

The modern era of imaging through opaque scattering media began in 2007 with the breakthrough of Vellekoop and Mosk [35]. They demonstrated that it is possible to focus light through an opaque scattering layer using only iterative wavefront optimisation. Crucially, no prior knowledge of the scatterer was required. In their setup, a laser illuminated a spatial light modulator (SLM), the modulated light propagated through a diffuser, and the scattered light behind the diffuser was recorded. By maximising a feedback metric – the brightness of a target point on a camera the incident wavefront was iteratively optimised. This yielded a sharp, high-contrast focus behind the scatterer and effectively ignited the field of wavefront shaping [23].

At this point, obtaining a focus behind a scattering medium may not seem equivalent to imaging. Yet, if the scatterer is treated as a random phase plate, the optimised SLM pattern and the scatterer together apply a spatially varying quadratic phase, effectively forming a lens. This "phase plate picture" is an approximation, but it remains surprisingly powerful. The range of validity of this approximation is governed by the optical memory effect [36], which states that small tilts of the incident wavefront produce correlated translations of the speckle pattern. The memory effect plays a role analogous to the paraxial approximation for scattering media. Within this regime, scanning the optimised focus across a fluorescent or luminescent sample enables formation of an image [37].

Since the early demonstration of focusing, two complementary families of ap-

proaches have emerged. The first manipulates the incident wavefront until a desired signal is recovered. The second infers the hidden information computationally from scattered light correlations stemming from the optical memory effect.

In wavefront-shaping methods, an SLM, Digital Micromirror Device (DMD), micro-electro-mechanical systems, or acousto-optic modulator (AOM) imprints spatial phases (and sometimes amplitudes) on the beam [38–41]. A feedback signal drives focus optimisation. Examples include maximising a second-harmonic [42] or two-photon signal [37], maximising the variance of the recorded field [43], or using an acoustically tagged guide star to localise the excitation in depth [44, 45].

Complementary to feedback-driven methods, there exist approaches characterising the medium by measurement or inference of the transmission matrix [46, 47]. The transmission matrix formalism expands the phase-plate toy-model into a linear operation acting on the incoming field: $E^m_{out} = \sum_n k_{nm} E^n_{in}$. The k_{nm} is a random complex coefficient connecting the input field in the nth mode E^n_{in} with the output field E^m_{out} in the mth mode. Once the input-output mapping is known, one can synthesise inputs that form foci or images at will.

On the other hand, hardware-light and purely computational strategies leverage the optical memory effect. For thin or weakly scattering layers, small tilts or shifts of the beam incident on the scatterer produce translated speckle patterns [36, 48]. This translation correlation allows for the inversion of the hidden object from intensity correlations alone. Bertolotti and co-workers showed that object structure can be retrieved by calculating a cross-correlation [49]. Katz and colleagues used the same speckle correlations to enable single-shot imaging through scattering layers [50]. These approaches reduce hardware demands and enable fast acquisition, though they rely on memory-effect, and usually are capable of reconstructing binary images (e.g., logos). Recently, I also contributed to this research field with a technique capable of imaging through a dynamic scattering medium with a minimal amount of light [51].

Hybrid schemes bridge these ideas. Holographic probing of the scattered field can seed wavefront optimisation [52]; conversely, structured or temporally coded illumination can enhance computational inversion [53]. With so many of the techniques, it can seem unwise to enter such a diverse field. Yet, the field of imaging through scattering media still awaits broader recognition through novel, practical methods. Quoting [30]: "The topic of imaging in complex media has evolved rapidly, producing many astonishing results, but with a few exceptions, these results have not yet percolated to the wider imaging community. One major reason for this is that many approaches only work well in some very specific circumstances, which those working on real-world applications may find too restrictive."

This thesis is motivated by that landscape. High-resolution imaging through scattering – and, more generally, under demanding conditions – offers a high scientific payoff, yet must also fit the practical needs of end users, and be generally applicable. It is why I began with a well-established, applied microscopy technique to understand such needs, constraints, and practical difficulties. Then I explored a niche technique and learned super-resolution. Finally, I performed experiments to overcome light scattering with high optical nonlinearity. With an entirely different approach, it is possible to acquire super-resolution images through scattering lay-

ers. Even though only one chapter (Chapter 5) is dedicated to imaging through scattering, the path of my earlier experiments naturally led to this result.

1.3 Thesis Outline

This thesis is meant to fulfil three goals: first, to inspire the reader. Second, is to keep the knowledge accessible and reproducible so that rebuilding the setups is straightforward and the know-how is not lost. Third, is to communicate my contributions scientifically. The last point is not here to prove that I am a scientist, but to share what I think is worth sharing.

In the spirit of these three points, I wrote each of the seven chapters. Before jumping into the quick outline of these chapters, let me convey the main message of this thesis that glues all the ideas from seemingly different chapters: Optical nonlinearity is fantastic and worth investigating.

Chapter 2 begins with fundamentals. I introduce the Abbe diffraction limit – a must-criterion in any general work focused on microscopy. Section 2.1 also contains the traditional ways to circumvent diffraction and their connection to nonlinearity. The final section of Chapter 2 (Section 2.2) introduces the depth–resolution trade-off that is the challenge for modern microscopy. It describes in detail the motivation of chapters 3 and 5.

Chapter 3 focuses on two-photon microscopy. I first discuss why two-photon excitation is needed and where its limitations arise (section 3.1). I then describe my experimental setup based on Benjamin Judkewitz's project (section 3.2). I try to be as detailed as possible so that one could learn as much from the text as I learned during the construction of this setup. I include concise instructions and figures of merit of the microscope. Additionally, I dwell upon auxiliary results like: preliminary results of two-photon image scanning microscopy (section 3.3) and Bessel-beam excitation (section 3.4). I assess why, in practice, these avenues proved less impactful than expected. The chapter concludes with the explanation (in understandable language) of the collaborative study "Opposing effects of rewarding and aversive stimuli on D1 and D2 types of dopamine-sensitive neurons in the central amygdala" [54] (section 3.5).

Chapter 4 turns to temporal focusing two-photon excitation and Super resolution Optical Fluctuation Imaging. I present the results of my publication "3D super-resolution optical fluctuation imaging with temporal focusing two-photon excitation." [55] accompanied by unpublished results. The chapter introduces both modalities with the minimum theory required to understand their strengths and limits (sections 4.1 and 4.2). I then detail the optical layout and explain the particular elements' placement for optimal operation of the setup (section 4.5). I report the main results and extend them with a line-scanning variant (unpublished), explaining when line scanning is advantageous. The chapter closes with potential developments and an outlook for this platform (section 4.6).

Chapter 5 introduces an entirely new approach to nonlinear imaging based on giant optical nonlinearities, namely: Nonlinear Imaging with Speckle Excitation

(NISE[1]). The central result shows that the high nonlinearity can be used to overcome strong scattering and achieve super-resolution imaging through scattering media. I introduce the concept, giving an understandable intuition and providing the theoretical background needed to understand NISE and why it works so well (section 5.1). I describe the experimental setup and all of its specific constraints (section 5.2). I try to make this chapter as detailed as possible, explaining the theory, experiment, and additional implications (section 5.4), losing the scientific form slightly, into a more textbook-like style. I feel justified to do so as the body of work is well described in the publication "Overcoming Light Scattering with High Nonlinearity" [56]. In Chapter 5, I focus on understanding the idea and its consequences rather than the results, because NISE proposes a completely new paradigm for imaging through scattering media. In my view, that is the most impactful part of the thesis and suggests an entirely novel route toward robust imaging through scattering media and subsequently deep-tissue imaging.

Chapter 6 offers conclusions and an outlook. I synthesise the main findings across platforms, and outline the next steps that follow most naturally from the results (section 6.3).

Chapter 7 (Appendix) completes the thesis. It consolidates user-level documentation for the setups and software, including calibration routines and data-acquisition workflows.

In sum, the thesis is designed to be suggestive, reproducible, and precise. My research goal was to lay the foundations for techniques usable for high-resolution imaging under demanding conditions.

I try to structure the text similarly to the oral presentations – using my expertise in presenting this form is the most natural for me. This is why some of the intros to sections may seem odd, as they contain "the teaser". I invite you, dear Reader, so we go through this fascinating story about spatio-temporal light manipulation for nonlinear microscopy together.

[1]You can read as 'naIs' or 'naIsI'

Chapter 2

Introduction to Microscopy

2.1 Abbe Diffraction Limit

What is this?

We obviously can see a horizontal line. However, if we zoom in, then maybe it is not a line, but a row of dots:

.....

We could zoom in even further and observe individual pixels or ink drops. Unfortunately, we can not zoom in indefinitely. Because light is a wave, infinite zoom is impossible: the propagation of the wave spreads the spatial information [57] and limits how precisely we can see, or better said – distinguish several objects that are close to each other. Such loss of precision is governed by diffraction; thus, the example with a dotted line should resemble a 1D diffraction grating. Based on such an example, and on the reasoning of Ernst Abbe, let us develop an intuition about the diffraction limit in imaging [58, 59]. We illuminate the grating with a monochromatic laser beam, and we want to image the grating (see figure 2.1). The beam splits into multiple diffraction orders with angles of propagation β following the grating equation:

$$\frac{m\lambda}{d} = sin(\alpha) + sin(\beta), \tag{2.1}$$

where m is the diffraction order, λ is the wavelength of the angle incident at α, and d is the spacing between the grating lines. α and β are measured with respect to the grating's normal. If we collect at least the first diffraction order with our imaging system, we can say whether it is a grating or an absorbing line. Such a picture gives us an intuition that the most dense grating visible is with $d = \frac{\lambda}{sin(\alpha_{max})+sin(\beta_{max})}$, where β_{max} is the maximum angle at which we still can collect the light with our optical system. β_{max} is the maximum angle at which we can illuminate our grating. Additionally, our grating could be immersed in some medium with a different refractive index n. We can either say that this medium bends the marginal ray towards the centre of our lens (see figure 2.1 c). Alternatively, we may think of it as changing the effective wavelength that influences the diffraction angles if the

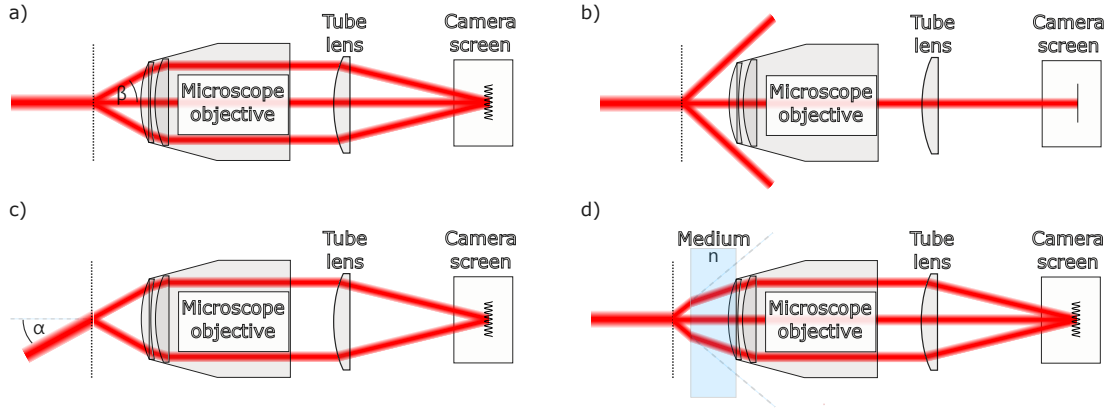

Figure 2.1: Schematic for grasping the idea of a diffraction limit and its scaling. (a) A laser beam illuminates a grating with period d. When the microscope objective has a sufficiently large numerical aperture to collect the first diffraction order, propagating at an angle α with respect to the optical axis, the resulting image forms a sinusoidal pattern. (b) For a smaller grating period, the first diffraction orders fall outside the collection cone of the objective and are therefore not captured. In this case, the image on the camera reduces to a uniform line. (c) Tilting the illumination to an angle β increases the effective collection angle for the first diffraction order, allowing the structure to be resolved. (d) Introducing a medium of refractive index n greater than that of the surrounding environment between the objective and the sample bends the rays toward the optical axis, again enabling the first diffraction orders to be collected and thus imaging is possible.

grating is submerged in the immersive medium. In such a way, we get the equation for the best resolution: $d = \frac{\lambda}{nsin(\alpha_{max}+n\beta_{max})}$. Defining NA $= nsin(\alpha_{max})$, we arrive at the diffraction limit for a bright-field microscope:

$$d = \frac{\lambda}{NA_{illumination} + NA_{detection}} \tag{2.2}$$

Where λ is the wavelength of the illuminating beam, $NA_{illumination}$ is the numerical aperture of the illumination optics, while $NA_{detection}$ is the numerical aperture of the detection optics. This derivation can give us a good intuition of the diffraction limit. For the sake of completeness, I must mention the criterion for distinguishing two incoherent emitters (e.g. two fluorophores) derived by Rayleigh for astronomy[60]:

$$d_{max} = 0.61\frac{\lambda}{NA} \simeq \frac{\lambda}{2NA} \tag{2.3}$$

For the derivation, I invite to read section 7.1.

It took roughly a century from Abbe's original formula to show, experimentally, that the diffraction limit is not absolute but rather obsolete. Any technique that produces an effective point image smaller than $\lambda/(2NA)$ is termed super-resolution, and such techniques matter because, at visible wavelengths, the resolution is on the order of hundreds of nanometers – the scale of many biological structures and processes. The practical importance of overcoming this bound was underlined by Eric Betzig, William E. Moerner, and Stefan W. Hell receiving the Nobel Prize in Chemistry (2014) for super-resolved fluorescence microscopy. As for their importance, it is also worth describing the major super-resolution methods briefly in this

introduction: In localisation approaches (Betzig), emitters are not allowed to radiate simultaneously within the same diffraction-limited spot: photoactivation or photoswitching ensures only isolated molecules are "on" at a given time [61, 62]. A PSF is fitted to each isolated spot, and the emitter position is assigned to the centre of the fit with the precision dependent on the number of detected photons N as $1/\sqrt{N}$. In Hell's approach (STED), a doughnut-shaped depletion beam quenches fluorescence everywhere except near its intensity zero, shrinking the effective emission region below the diffraction size [24]. Apart from the Nobel-awarded methods, there are a few worth mentioning. E.g., MINFLUX, developed in S. Hell's group, uses switching (as in PALM), but localises molecules by probing them with a doughnut at a few positions and inferring their location from the measured low-photon signal [63]. This achieves very high localisation precision with fewer photons than standard localisation techniques (PALM, STORM), reaching the localisation precision of 1-3 nm [64]. These techniques, however, usually struggle with fast data acquisitions. Either one needs to scan (STED), allow only a sparse subset of molecules to emit light at a given time (PALM), or both (MINFLUX). In contrast, there exists relatively fast (wide-field), ingenious super-resolution imaging by structured illumination microscopy (SIM) [65]. Illuminating a sample with a known grating, with different positions and angles, and a bit of postprocessing yields a wide-field image with twofold resolution gain with respect to the Abbe limit in its linear form and larger gains in nonlinear variants [22]. The alternative could be to use an ordinary wide-field microscope and utilise only the particular characteristics of the fluorescent labels. Super-resolution Optical Fluctuation Imaging (SOFI), described in section 4.2, does exactly that [66]. Interestingly, SOFI is not required to work only in the wide-field modality, but can be used in the most popular type of microscope in biology – in the Confocal Laser Scanning Microscope (CLSM) [67, 68]. One notable improvement of CLSM, also used in [67, 68], is the Image Scanning Microscopy (ISM)[69]. ISM introduces $\sqrt{2}$ improvement with respect to the regular CLSM. Utilising shifted pinholes or a bunch of small detectors, appropriate postprocessing provides better signal and resolution [69]. The aim of developing another super-resolution method was what initially motivated me, yet upon understanding the needs of bio-imaging, it turned into the aim of developing high-resolution imaging in demanding conditions. Under such conditions (deep volumetric imaging or imaging through scattering media) most of the described methods struggle to deliver super-resolution.

2.2 Depth-Resolution Trade-off

As our knowledge of biological systems expands, we are compelled to develop new optical tools that can image increasingly complex structures in situ and non-invasively. L'appétit vient en mangeant. In most relevant cases, these targets are intrinsically three-dimensional, which immediately raises the bar for data quality and system design. Three-dimensional imaging is substantially more demanding than usual 2D imaging of a specimen under a cover slip, because one must simultaneously control axial confinement, photostability, and detection efficiency while preserving both lateral and axial resolution.

Three-dimensional fluorescence microscopy faces several recurrent challenges [70]. The first is out-of-focus light, deteriorating the in-focus features. The second is photobleaching, which irreversibly influences the samples. In 3D, bleaching fluorophores outside the plane of interest is especially a hurdle, limiting the time for the 3D volume acquisition. The third is non-uniform resolution – axial vs lateral. Usually, we want to localise certain features in 3D, which obviously requires good resolution in all 3 dimensions (in standard approaches, the axial resolution is 2 times the lateral one). The fourth and the fifth challenge, being the point of this section, are the loss of resolution with increasing depth. Most samples scatter and absorb light, and both the excitation and fluorescence emitted by the sample are influenced by scattering and absorption. Leaving aside that longer working distance (depth) usually means lower NA, more fundamentally, the effective NA for the remaining ballistic (not scattered) light decreases with depth. The decrease of NA inevitably leads to broadened detection and excitation PSFs [71].

For high-resolution deep imaging, it is therefore essential to mitigate all of these effects, among which tissue absorption and scattering are typically the most severe issues. A compact characterisation of the medium is helpful at this point and involves two ingredients: (a) spectral absorption and the associated "biological windows", (b) the mean free path, which quantifies scattering event rates.

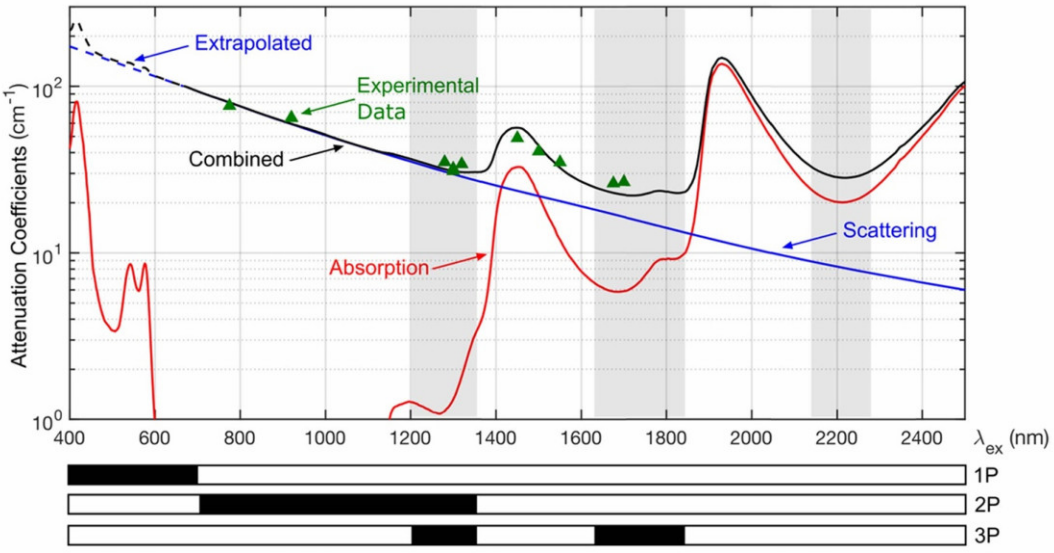

Figure 2.2: Absorption and scattering coefficients in biological tissues. Figure from [31]. The red line depicts the combined absorption coefficient of water [72] and blood [73]. The blue line represents the calculated (Mie theory) scattering coefficient for a mouse cortex phantom [26] composed of polystyrene beads at a concentration of 5.4×10^9 ml^{-1}. The black line corresponds to the combined scattering and absorption coefficient (mean free path). Green triangles show experimental measurements of the combined scattering and absorption coefficient for mouse brain [26, 73–76]. Dotted blue and black curves indicate extrapolated regions of the scattering and effective attenuation coefficients, respectively. In grey – regions showing windows for deep tissue imaging. The black bars below the plot mark the spectral regions typically used for one-, two-, and three-photon excitation.

Absorption attenuates intensity as $I(d) = I_0 \cdot \exp(-\alpha(\lambda)z)$, where z is the depth and $\alpha(\lambda)$ is the absorption coefficient; when $\alpha(\lambda)$ is large, deep imaging at that wavelength becomes impractical regardless of other optimizations. Figure 2.2 adopted from [31] sketches absorption and scattering coefficients in biological tissues, highlighting the relatively small absorption coefficients in the near-infrared (NIR). This analysis makes NIR excitation desirable for depth. Yet, Abbe's resolution criterion introduces a competing constraint: with $d = \lambda/(2NA)$, resolution depends directly on wavelength, so longer wavelengths inherently degrade the PSF spot size.

In most conventional modalities, scattering generates an unwanted signal that reduces the signal-to-noise ratio and severely degrades image quality. At the single-photon level, a photon travelling inside tissue is either absorbed or scattered; the mean free path l_p specifies the average distance after such events happen and is given by

$$l_p = \left(\frac{1}{l_s} + \frac{1}{l_a}\right)^{-1}, \tag{2.4}$$

where l_s and l_a are the scattering and absorption lengths, respectively (the inverses of scattering and absorption coefficients). In practice, imaging beyond roughly two to three mean free paths with regular methods is rarely successful, not because of a formal prohibition but because regular methods utilise ballistic light that decays exponentially with depth (z):

$$I_{ballistic}(z) = I_0 \cdot exp\left(-\frac{z}{l_p}\right). \tag{2.5}$$

At large depths, there is not enough ballistic light to image with. Such constraints invite a further question: if imaging becomes impossible after some depth, what happens to resolution along the way? Surveying gold-standard techniques that achieve exceptional resolution (mentioned in section 2.1) reveals a common pattern: most methods that achieve outstanding resolution are unable to do so in harsh scattering conditions at large penetration depths, because they rely on ballistic light. A schematic "depth–resolution tradeoff" is illustrated in Figure 2.3 across representative techniques. Although not well-defined, the depth-resolution trade-off appears to be a challenge – similar to the Abbe diffraction limit. Let breaking this depth resolution limit be our challenge (my and yours, dear reader). In chapter 5 I show how to obtain super-resolution using scattered light, however, it is not completing this challenge yet. I hope this thesis inspires you, dear reader, to develop new ideas that overcome the depth-resolution trade-off.

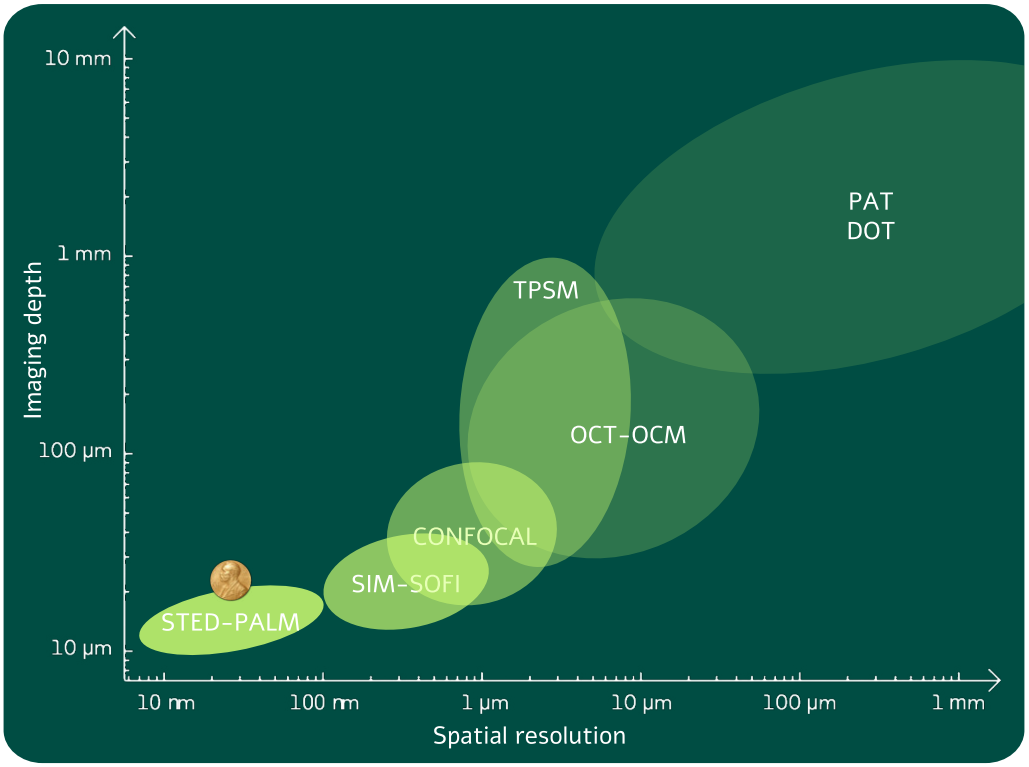

Figure 2.3: The "depth-resolution" trade-off. Comparison of the most popular techniques and their capability to image deeply. STED [24] and PALM [62], although reaching high resolutions, quickly become unfeasible with 3D specimens. STED require a doughnut beam with little to no aberrations – conditions impossible to achieve in scattering samples. PALM stops working when PSFs from different molecules overlap (as is usual for out-of-focus signal). SIM offers slightly better depth but is limited by the fidelity of the grating projected at the image plane. SOFI improves the detection PSF that enlarges with depth. Confocal (CLSM) excite the molecules in the whole volume, and at larger depths, the out-of-focus signal (also originating from the scattered light) enters the pinhole, overwhelming the signal. Two-Photon Scanning Microscopy (TPSM) [25] is limited by the usage of infrared radiation and fixed $\sqrt{2}$ resolution improvement with respect to the diffraction limit and is the most promising technique for deep-imaging thus described in the next chapter. Optical Coherence Tomography (OCT) [77], Optical Coherence Microscopy (OCM) [78], are not compatible with fluorescence thus not considered here. Photoacoustic Tomography (PAT)[79] relies on NIR excitation with the photoacoustic effect being linear (no resolution improvement due to nonlinearity), similarly to Diffuse Optical Tomography (DOT) [80]. Both are strictly bounded by the Abbe limit. Credit: Sylvain Gigan, Radek Lapkiewicz.

Chapter 3

Two-Photon Scanning Microscopy

3.1 The Gold Standard for Bio-imaging

One of the things I like most about physics is that we can set up simple experiments and then draw our own conclusions from what we see. A very simple, but surprisingly informative, experiment is to check by ourselves which colours of light can pass through a piece of biological tissue (validation of figure 2.2 on your own skin). Turn on the flashlight (double click on the second button of the attached laser pointer, or use your phones' LED). The LED light is white, so it contains most of the visible wavelengths. Place your fingertip over it. The light that makes it through your finger is red. We have just confirmed that the longer wavelengths get through a biological tissue better than shorter ones.

This everyday observation connects directly to multiphoton microscopy. If longer wavelengths are attenuated less in the tissue than shorter ones, it is better to image with red light rather than green or blue. More precisely, absorption and scattering are both relatively small in the NIR spectral region, so the NIR light should be the most suitable for deep imaging. Two-photon scanning microscopy (TPSM) does exactly that. By using near-infrared light to excite standard fluorophores via a nonlinear two-photon process, TPSM retains the advantages of familiar visible-wavelength dyes while benefiting from improved NIR light transmission through tissue [71].

The key physics is simple – two-photon absorption which rate grows with the square of the instantaneous light intensity [71, 81, 82]:

$$R_{2\mathrm{P}} \propto I^2. \tag{3.1}$$

To get a strong 2P fluorescence signal, we should increase the intensity I. The increase, however, should be subtle, as high average power at the sample risks heating and damaging the specimen. TPSM achieves high intensity without high average power in two ways. First, it focuses the infrared beam very tightly, which concentrates the effective excitation into a tiny spot. Second, it uses ultrashort laser pulses (typically femtosecond-long), which increase the peak power while keeping the average power constant [25].

Under these conditions, the excitation is confined to a small volume around the focus (see Figure 3.1). Importantly, a larger beam or weak, scattered light

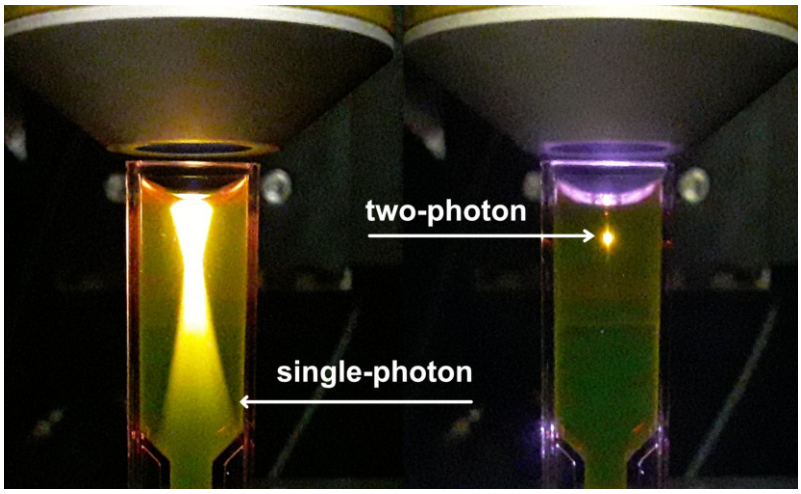

Figure 3.1: Comparison of the one-photon excitation with two-photon excitation. The one-photon excitation (left), excites the whole volume of the fluorescent sample, while for the two-photon excitation, the volume is confined to a small focus (right). Source: [83]

away from the focus does not have sufficient intensity to excite the fluorophores meaningfully. As a result, the out-of-focus background is strongly reduced both laterally and axially, and bleaching is confined to the plane of interest. Additionally, the lateral size of the excited spot is smaller by a factor of $\sqrt{2}$, compared with linear excitation at the same wavelength and numerical aperture.

There is even another bonus to two-photon excitation: Once we have this tightly confined excitation spot, we do not care about the detection optics so much. We obtain the image by scanning the spot across the sample, for example, with galvanometric mirrors. The emitted fluorescence is measured with sensitive bucket detectors such as Photo Multiplying Tubes (PMTs). Since almost all the fluorescence signal originates from the small focal volume, there is no need for a confocal pinhole, as in CLSM, which requires high stability and precise alignment. In TPSM, we collect as many photons as we can with a bucket detector and build the image point-by-point. In practice, TPSM can deliver clear structural and functional images at depths of about 500 μm without corrections [84].

There is, however, a depth-related cost that we have to manage carefully. The fraction of ballistic (unscattered) excitation light decreases exponentially with depth (see equation: 2.5), so to maintain a usable fluorescence signal, one is tempted to increase the excitation power [85]. Beyond a certain point, the mean power on the sample can become physiologically unsafe[1].

For biological imaging, lower mean power is generally better, while a higher signal is always welcome. The nonlinearity helps here because it is the peak power, not the mean power, that drives the two-photon fluorescence excitation rate at fixed duty cycle [86]. While keeping the same mean power, we can raise the peak power by reducing the laser repetition rate (fewer, more energetic pulses) or by shortening

[1]Leaving aside damage to the sample, at some point, the needed excitation power is so large that the labels on the surface of the specimen will be excited, even though the beam is not focused there – see ref. [85].

the pulse duration (higher peak power for the same pulse energy).

Neither approach is a complete solution, and both come with trade-offs. Very short pulses are broadened by dispersion of the optics, and by propagation through the sample [87] and perfectly compensating for this at the sample plane is technically challenging (yet possible [88]). Alternatively, very low repetition rates create sampling problems for live imaging. To see the numbers, consider video-rate imaging at 30 frames s^{-1} (FPS) with 512×512 pixels: that is roughly 7.9×10^6 pixels per second. An 80 MHz femtosecond oscillator provides about 10 pulses per pixel at that frame rate, which is enough for a stable signal and some averaging. A 1 MHz source would deliver only about 0.13 pulses per pixel, so it could not illuminate every pixel in a single pass. In addition, higher peak intensities increase nonlinear bleaching[2] and the risk of multiphoton damage, which must be kept within safe limits for live samples.

Even with these limitations, TPSM remains the gold standard for deep, in-vivo fluorescence imaging because it matches what tissue "likes" optically (infrared transmission and confined excitation) with what biology needs practically (established fluorophores, sensitive detection, and minimal out-of-focus exposure).

In the rest of this chapter, I will describe how I built a reliable TPSM open platform. This instrument follows the design shared by Benjamin Judkievitz (also described in [90]), to whom I am especially grateful, as it enabled experiments on living mice, and was extremely entertaining to build. After adapting his design to our needs, we recorded neural activity in response to controlled stimuli. The exemplary images obtained with my TPSM are shown in Figure 3.2.

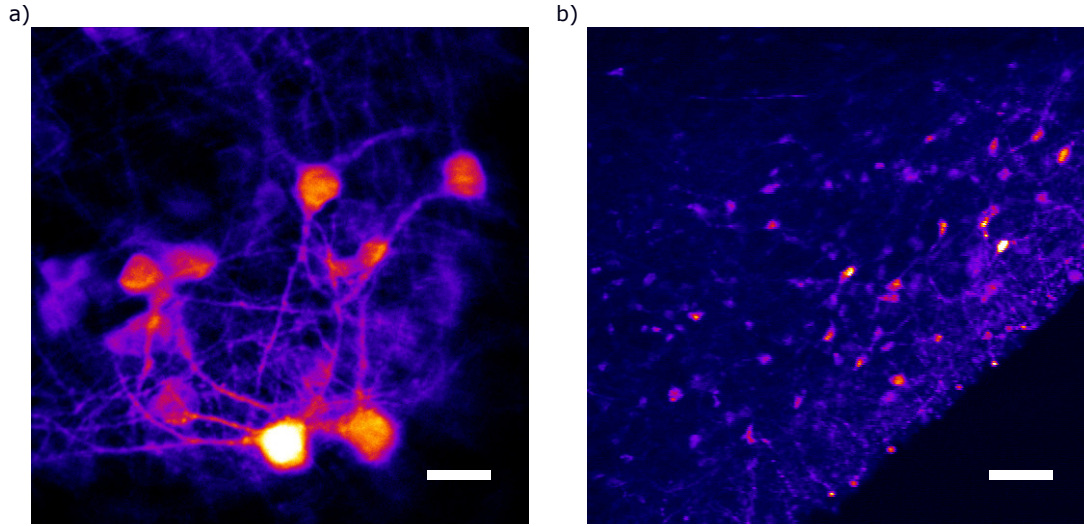

Figure 3.2: The exemplary images from my TPSM. (a) high resolution images of neurons imaged in-vivo in central amygdala (through a GRIN lens). Image created by averaging 100 scans. Scalebar 20μm. (b) Large FOV neurons on brain slice used for ex-vivo activity study. The image is the average of 1000 scans. Scalebar: 100 μm. Credit to both images: L. Bijoch.

[2]Notably, proper pulse shaping can reduce bleaching [89].

3.2 Operation of my TPSM

I write this section with my colleagues from the Nencki Institute of Biology in mind, so that after reading it, they can use the microscope knowing how their TPSM works. First, I must admit that assembling this microscope was a very enriching experience, especially given the need to overcome all the extraordinary issues – e.g., the mouse sometimes defecates, and one needs to cover everything appropriately to avoid contaminating the optics. Such things do not happen either in an optical laboratory or while designing a microscope on paper. This "on the paper" design is shown in Figure 3.3 together with the photo of the exctual setup. The rest of this section describes the beam path, fluorescence path, and wide-field, which will reference Figure 3.4.

3.2.1 Excitation Laser

The microscope driving force is a Halite920 femtosecond laser (from the Polish company Fluence Technology), operating at a central wavelength of 920 nm. In other words, with the 2-photon excitation two photons with energies $\frac{hc}{\lambda}$ ([3]) are absorbed simultaneously, delivering twice as much energy to the fluorescent molecule, namely: $2\frac{hc}{\lambda}$. Effectively, the two-photon excitation with 920 nm central wavelength is equal to the one-photon excitation with half of the two-photon wavelength: 920/2 = 460 nm. The Stokes shift [91] dictates that the emission from such a molecule is shifted to the longer wavelengths, so the best-suited fluorescent molecules for our laser would be the ones emitting green light (GFP[4]-like proteins). The maximum laser power is 1.5 W, while during daily experiments, only a fraction ($\simeq$ 300mW from the laser output) is used. The pulses from Halite920 have a width of around 200 fs which enables efficient two-photon excitation. In general, the shorter the pulses, the better, e.g, company Toptica offers 920 nm lasers with less than 100 fs pulse width – FemtoFiber Ultra 920. The shorter pulse in FemtoFiber should enhance the signal; however, Halite920 has a different repetition rate (20 MHz) than Toptica's (80 MHz). It means that with the same mean power (the power that is heating the specimen), pulses from Halite920 have higher peak power than the ones from FemtoFiber.

[3] h being Plancks constatnt, c is the speed of light, and λ is the wavelength – in our case 920 nm.
[4] Green Fluorescent Protein

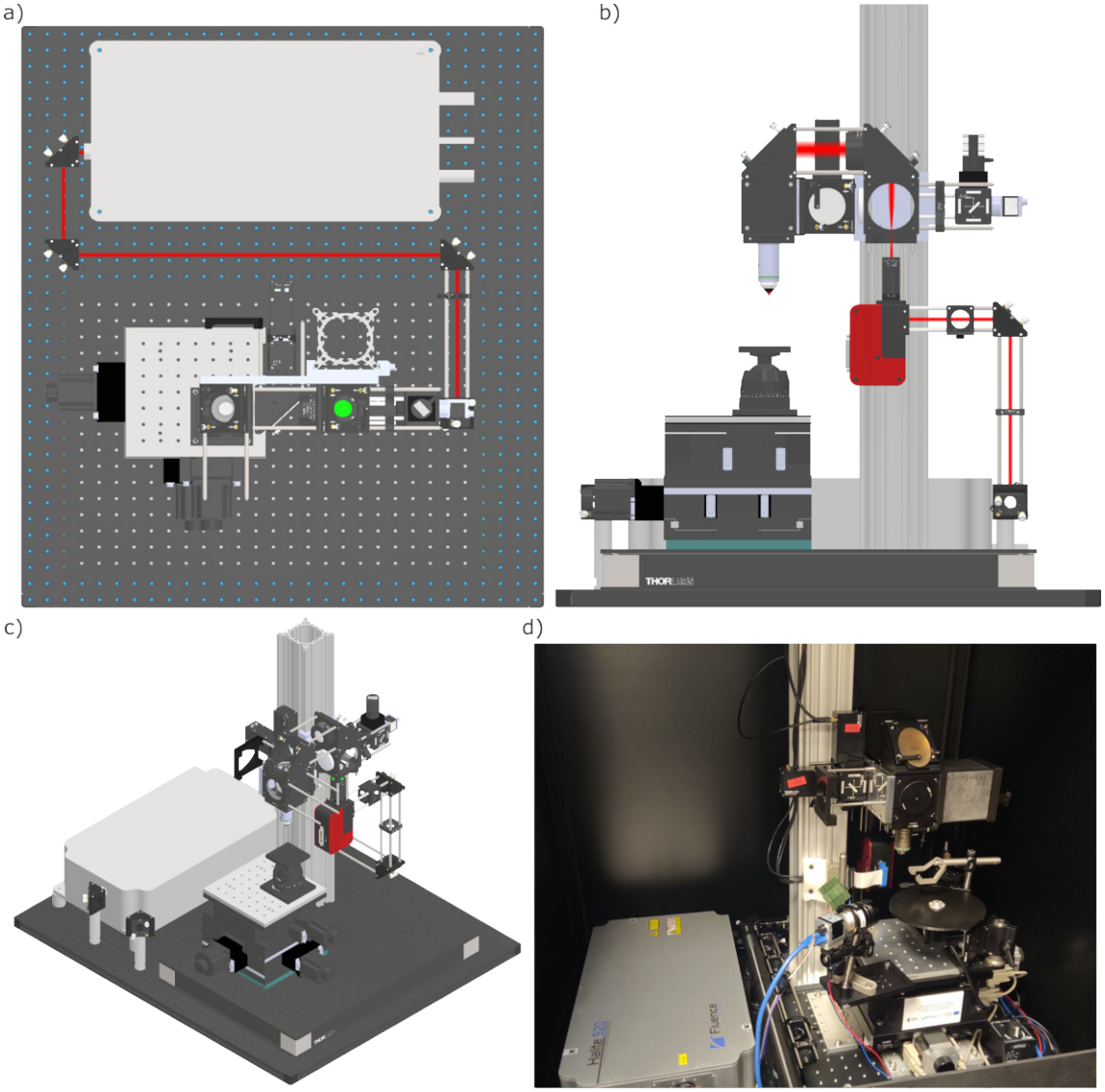

Figure 3.3: My implementation of Benjamin Judkewitz's TPSM design. Based on the shared design and CAD files from Thorlabs, I created the final assembly in Autodesk Inventor Pro. (a) Top view, with the depicted red excitation beam path. (b) Front-view illustrating the further excitation beam path. (c) Perspective view of the setup. The region beneath the objective in CAD drawings does not represent the final experimental configuration, which includes a head-fix assembly and a rotating disc; these elements are visible in the photograph of the actual setup (d). The entire excitation pathway is enclosed using 3D-printed tubes and custom components mounted on cage rods to minimise dust deposition on optics and to suppress stray light reaching the detectors.

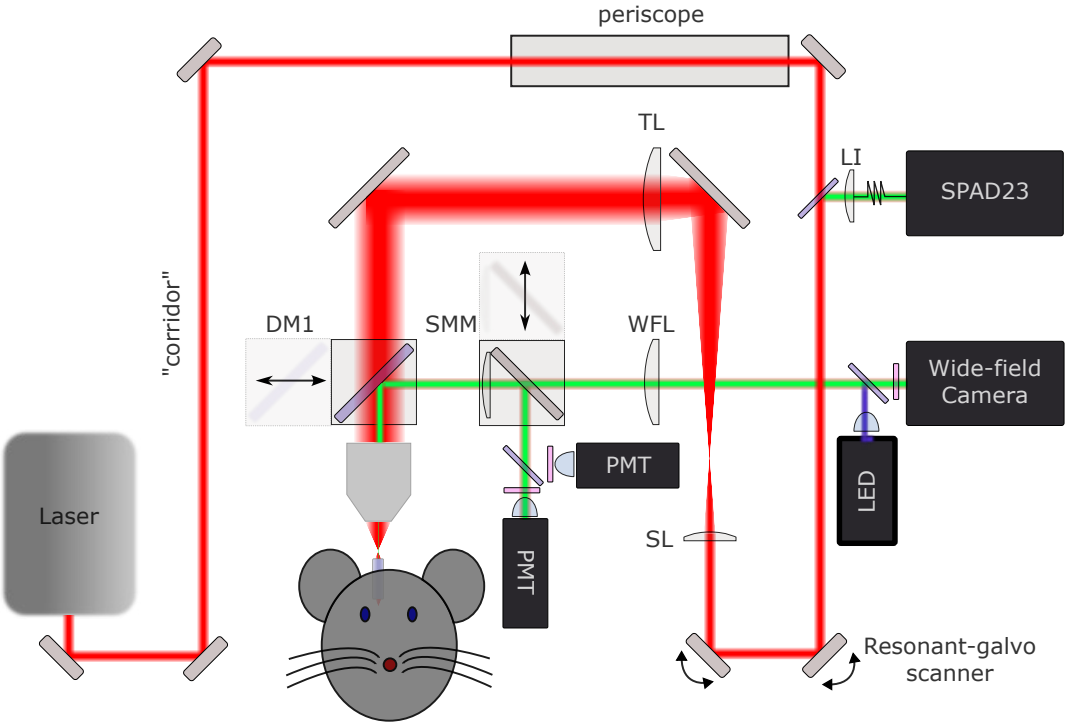

Figure 3.4: The optical scheme of the TPSM. Laser beam (red) passes through a meter-long "corridor", is elevated by the periscope and enters the main body. The beam enters the Resonant-galvo scanner, and is focused with a Scan Lens (SL), and collimated with a tube lens (TL), increasing its diameter 4 times. Next, the beam enters the objective and focuses. The focus is relayed into the deep parts of a mouse's brain with a GRIN lens. Alternatively, one can place a sample in the objective's focus. The whole stage under the objective can move in 3D and can be controlled by a "joystick". The fluorescence (green) from the examined structure is collected with the objective and can be directed to the PMT path or to the descanned SPAD23 path. Such a switch between the detection paths is achieved by sliding the dichroic mirror DM1 in or out. The default position of DM1 is directing the fluorescence through a 100 mm lens that, together with aspheric condensers placed before each of the PMTs, assures optimal signal collection with either red or green channel PMTs. This 100 mm lens and a mirror constitute the Sliding Mirror Module (SMM) that can be repeatedly removed from the fluorescence path. While the SMM is removed, the wide-field tube lens (WFL) creates an image on the wide-field camera. Before the camera, a dichroic mirror provides an additional channel for LED illumination for one-photon excitation. With the DM1 removed, the ballistic fluorescence follows the excitation beam path and, after a dichroic mirror, is focused with a 200 mm lens (LI) onto the SPAD23 array. On the scheme, the distances are arbitrary, especially visible with the placement of SPAD23, which in reality is placed in the focus of LI.

3.2.2 The Excitation Beam Path

Putting your hand in the strong femtosecond beam is never a good idea; however, when working with optical setups, sooner or later it will happen unless you know exactly where the beam is. In figure 3.3 a,b,c, I put graphical representation of TPSM to resemble as close as possible the real setup to make the beam tracking easier. Additionally, this description will be useful to avoid any harm. We start analysing the beam path from the laser, as it is the easiest to track from there. Exiting from the laser, the beam is reflected from two steering mirrors (see Fig. 3.3 a). Manipulating both of them is usually enough for proper alignment. The two steering mirrors direct the laser beam onto a meter-long "corridor" (see Fig. 3.4) where additional optics (e.g. Bessel beam module[5], or AOM) could be placed. After this "corridor", the mirror reflects the beam behind the microscope column and the beam bounces upwards [6]. After exiting the periscope, a single mirror directs the beam to the scanning module. Before the module, there is a dichroic mirror that can be used for descanned detection, for example, for two-photon ISM (see section 3.3). Passing through the dichroic mirror, the excitation beam enters the scanning module that we are going to take a closer look at.

Scanning module

The scanning head is one of the core hardware devices in our TPSM, and we use an 8 kHz Galvo-Resonant Scanner (Thorlabs: LSK-GR08/M). It consists of one resonant mirror and one galvo mirror. The difference between the mirrors is such that, with the galvo mirror, one can select the rotation angle with high accuracy. The resonant mirror, on the other hand, constantly oscillates at a fixed frequency (in our case, 8 kHz), and the control voltage changes only the amplitude of these oscillations. The reflective surface of the resonant mirror is circular, and I use it (the circular mirror surface) as the alignment checkpoint. When the beam is roughly in the middle of this mirror, the alignment is usually completed unless something extremely bad happened upstream (see the detailed alignment instruction in section 7.2.2). The scanner is controlled by two analog voltage inputs: one to select the position of the galvo mirror, used for the so-called slow-axis, and one for the amplitude of resonant mirror deflection. Additionally, the Galvo-Resonant controller has a TTL output for the resonant signal synchronisation. Going back to the beam path, the galvo mirror voltage must be close to 0.0 V during any beam tracking or alignment. The high deflection angle of the galvo mirror causes the beam to clip and can be used as a shutter not to expose the specimen with unwanted light, but can also cause an "everything-is-wrong" moment. When the galvo deflection angle is set to zero, the

[5]The Bessel beam module can be seen, near the black plastic tube in the photo of the setup – Figure 3.3 d.

[6]Before and after this periscope mirror, there is a place for two lenses to form a 4f magnifying telescope (e.g. with $f = 125$ mm and $f = 250$ mm, $M = 2$. By choosing an appropriate first lens and keeping the second lens fixed, this magnifying telescope can be used to adapt the beam size for different objectives, as for deep-imaging, NA of around 0.6 is optimal [92]. For our objectives (Nikon 10x NA = 0.3, and Nikon 20x, NA = 0.5), I did not observe much difference in resolution while using the magnifying telescope and not. Thus, in the final setup, the lenses are removed to limit the setup's complexity.

beam exits perfectly upwards. Next, the scan lens (Thorlabs: SL50-CLS2) collects the beam exiting from the scanner at different angles (in schematic 3.3 c, the scan lens is acronymed as SL). Around 30 mm from the lens, there's a small beam focus that, for large laser power, can easily burn holes in the probing paper, which should be avoided. After the lens, the expanding beam reaches an upper part of the turret, reflects from the mirror up to the Tube lens (Thorlabs: TTL200MP, in scheme 3.3 c acronymed TL) setting the final size of the beam (4 times larger than the beam entering the scanning head). After the tube lens, the collimated beam reflects from a mirror, passes through a dichroic mirror, and enters the objective.

3.2.3 PMT Path

We now track the fluorescent light that comes from the position of the focused laser spot in the sample. This fluorescence is collected by the objective and then separated from the residual excitation laser back reflections with a 2-inch dichroic mirror (Thorlabs: DMLP650L, in scheme 3.3 c acronymed DM1). Next, it passes through a 100 mm plano-convex lens, which enhances signal collection efficiency. The lens and further mirror are mounted in a single kinematic mount constituting the Sliding Mirror Module (SMM in scheme 3.3 c) With SMM inserted, the fluorescence bounces from the mirror, passes the shorpass filter (Semrock 665/SP HC Brightline, F37-665), and is directed to the dichroic mirror (Beamsplitter HC BS 562, F38-562) that splits green and orange/red fluorescence. Then any residual light is rejected by a bandpass filter placed in front of each PMT (Orange/Red channel – Semrock 607/70 BrightLine HC, F39-608, and Green channel – 525/50 BrightLine HC, F37-516). Before each of the PMT's active areas, an aspheric lens (Thorlabs: ACL2520U-A) is mounted to confine the fluorescence light to the sensor's area effectively. Ideally, the lens with $f = 100$ mm in the PMT path, and the aspheric lens, should create an imaging system that images the entire aperture of the objective onto the PMT's sensor.

3.2.4 Image Formation

To understand how image formation with a resonant galvo scanner works, let us focus on the figure 3.5. The beam deflection after the resonant mirror translates into the shift of the position of the focus. This focus is scanned with a ziz-zag pattern across the sample (simplified in Fig. 3.5 a). Due to resonant mirror characteristics, its angle is a sinusoidal pattern in time (Fig. 3.5 b, top row). At every turn-off of the resonant mirror, the controller outputs the rising edge of the TTL signal, also called the line trigger (second row of Fig. 3.5 b). This line trigger is used to form a single row of the final image (fast axis). The scanning in another direction (slow axis) is handled by steering the galvo mirror with a step-like pattern (third row in Fig. 3.5 b). In our TPSM, while steering the galvo with a step-like pattern, the mirror is moving with a constant speed (as if it was directed by a constant linear slope) due to inertia. Every step of the steering voltage is synchronised with the TTL signal at the end of the line (fast-axis turn-around). The galvo mirror is then steered by as many steps as the final image's height in pixels, while the resonant

mirror completes half as many cycles. Each cycle creates two rows of the image. All the even rows are taken from left to right, while the odd rows are taken from right to left (red arrows in c and d in Fig. 3.5). In image processing, it is necessary to invert every second row to achieve proper image formation. Additionally, when creating the images from zig-zag patterns (with the need for row inversion), there is most often a need for appropriate position shifting of the odd rows with respect to even rows (schematically shown in Fig. 3.5 d). There is usually a slight difference in turning speed between left and right turns, which causes a constant offset between the rows. Interestingly, the row-to-row shift is a common issue independent of the scanning system – scanning with a piezo stage or a galvo-galvo system with a long turnaround time still introduces this effect.

At the end, we left the divisions of rows into particular pixels. The maximal number of pixels is limited by the sampling rate of the DAQ card measuring the PMT signal (bottom row of Fig. 3.5 b), but more practically by the repetition rate of the laser. On the other hand, due to Nyquist sampling theorem [93] we should divide the image in pixels with the size at least twice smaller than the diffraction limit. To do so, we need to convert the time basis on which we collected the samples of the voltage from the PMT into a pixel basis that represents the appropriate positions. We do it by inverting the sinusoidal dependence of the resonant angle on time. The inverse function is the arcsine, which is approximately linear for arguments between -0.7 and 0.7. For simplicity, we choose only this (linear) part of the scan for our pixels (red arrows in Fig. 3.5 c).

Two important notes follow from such image formation. One is that during the turn-arounds, the laser spends more time illuminating the sample, which increases bleaching in those regions, which we do not image. Additionally, sometimes the PMT we use is overexposed even though there are no bright objects in our preview.

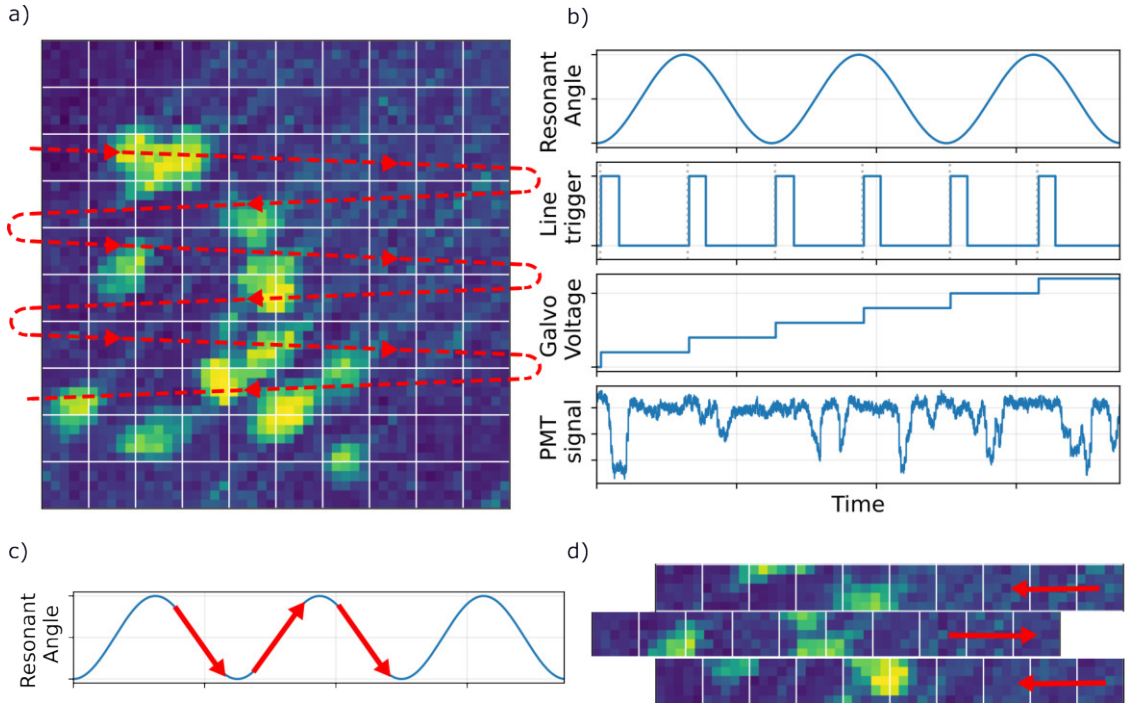

Figure 3.5: The timing, synchronisation, and pixel assignment in resonant-galvo scanning microscope. a) the sample (Hippocampal neurons stained with m-cherry) is scanned across with a zig-zag pattern – red dashed line with arrows depicting the direction of the scan. Panel (b) represents the synchronisation graphs. From the top: the resonant mirror deflection angle, TTL line trigger, galvo mirror steering voltage, and the time signal from the PMT detector. Note that a higher fluorescence signal corresponds to a lower voltage – inverted characteristics of PMTs. In (c), red arrows mark the regions from which the rows of the final image are created. (d) The rows created by left or right propagated scanning beam (marked with red arrow) are shifted with respect to each other. To obtain a final image, one has to perform an appropriate "phase-shift" of the odd rows.

3.2.5 Synchronisation of Peripheral Devices

The master for all synchronisation is the line trigger, as it stems from the resonant mirror's inherent resonant frequency. However, it is uncomfortable to use for synchronising with other devices, such as cameras. For that, the imaging software (ScanImage) provides a so-called frame trigger with the rising edge coinciding with the first line of the scan. I measure this trigger with Teensy (Arduino-like board) and output all the synchronisation signals from this board. In particular, I output the trigger signal for the camera monitoring the mouse face that operates at 60 FPS. In this way, images from the camera are synchronised with the images from the microscope. Other devices just add on to the shared timeline of the microscope, and camera frames (for more details, go to section 7.2.1)

3.2.6 Wide-field Path

The wide-field modality is extremely helpful even in scanning microscopes, and I advise always including it in any microscope. For a particular application of my TPSM for imaging amygdala neurons using a GRIN lens, the wide-field preview is invaluable. With a preview (e.g., using white light), it is possible to locate and position the GRIN lens surface appropriately. In the preview, the SMM is slid out of the fluorescence light path. The fluorescence then goes through a 200 mm lens (WFL in scheme 3.3 c), imaging the sample onto the camera sensor (Bassler acA2440-75um). The camera is positioned so that the sharp fluorescence image is formed at the focus of the infra-red excitation light. Before the camera, a dichroic mirror is also placed to provide wide-field excitation with a UV LED.

3.3 Two-photon ISM

The first motivation for building an open, modular platform was to implement two-photon image scanning microscopy (2P-ISM) with a SPAD array [94, 95].

To test the feasibility of 2P-ISM, I used PI SPAD23 – an array of 23 single-photon avalanche diodes (SPADs) that can be treated as 23 independent detectors corresponding to 23 effective pinholes displaced laterally. With appropriate ISM processing (shift-and-add using the measured pinhole offsets), one expects a lateral resolution improvement by a factor of approximately $\sqrt{2}$ relative to the native diffraction limit at the emission wavelength [69].

In TPSM with a non-conjugated galvo-scanner setting, however, this concept is not straightforward. Because the detector array is stationary in space, the image of the infrared-excited focal spot on the array must also be stationary as the beam scans the sample. To provide that, a descanned (d-scan) detection geometry is required. In d-scan, the fluorescence retraces the excitation path back through the scanners but in the reverse direction; after passing the galvo pair, a dichroic mirror separates the backwards-propagating fluorescence from the forward-propagating excitation, and a single lens images the fluorescence PSF onto the detector array. In the ideal case, this renders the PSF position on the SPAD array independent of the scan angles.

Two practical issues compromised this idealisation. First, chromatic aberrations between the NIR excitation and the visible fluorescence are significant. Second, our scanner module was not a conjugated galvo system. Without proper objective pupil conjugation, beam steering introduces residual displacement in the d-scanned arm, so the image of the PSF on the SPAD array drifts with scan angle.

These two points make the implementation harder, but not fundamentally impossible. Chromatic aberrations, for example, could be compensated by making the excitation beam divergent or convergent before the scanning module (the focus position shifts then axially with only a slight increase of its lateral size). The angle-dependent shifts could be compensated either in postprocessing or with additional optics (e.g., a weak cylindrical pair to image only a particular scanning mirror).

The decisive factor that led me to abandon the Two-photon ISM was the photon budget. The descanned path imposes additional losses due to the longer fluorescence path, and the quantum efficiency of SPADs also reduces the signal-to-noise ratio compared to PMTs. More importantly, though, the ISM utilises only ballistic fluorescence photons. In volumetric scattering samples, ballistic fluorescence is attenuated exponentially with depth due to scattering, and the signal at the detector becomes too small for practical frame rates and reliable ISM reassignments. Two-photon ISM might work acceptably on thin samples, but in that regime, conventional one-photon ISM already performs well while being simpler and more efficient. Although two-photon excitation does reduce out-of-focus bleaching, these gains did not seem to offset the complexity and signal losses in our implementation.

Nevertheless, I put SPAD23 in my TPSM, in the descanned path. It could prove handy for some additional measurements, e.g. FLIM on thin brain slices. To acquire images with SPAD23, I installed the DM1 on a movable platform. It can slide on 6 mm rods in and out of the excitation beam path. With the DM1 removed,

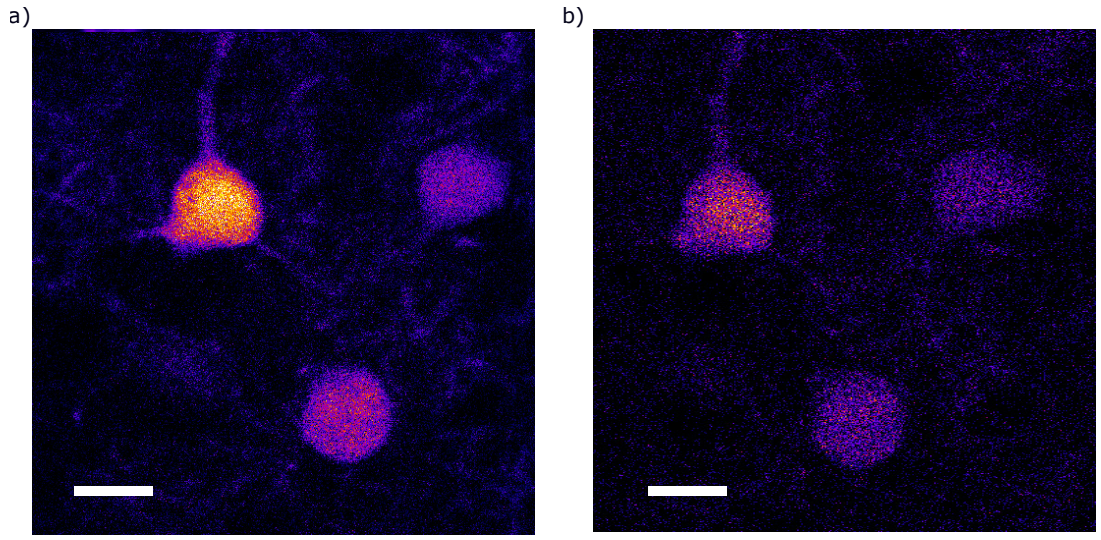

Figure 3.6: Comparison of images obtained with PMT and SPAD23. Image of neurons stained with Thy1-GFP collected with (a) PMT, and (b) SPAD23 in descan. Images are averaged over five scan frames. The maximum signal in (b) corresponds to 5 detected photons. Credit for data analysis of images from SPAD23: Aleksander Krupiński Ptaszek. Scalebars approx. 20 μm.

the fluorescence bounces back through the excitation path, being separated from the excitation laser with a dichroic mirror (Thorlabs DMLP650R) after exiting the Resonant-galvo scanner. The d-scan is finalised with a LI 200 mm lens, effectively creating a PSF with a size of around 50μm. With the single SPAD having 23 μm, the PSF visibly occupied roughly 8 SPADs with a stationary beam. Upon scanning, the spot translated on the array reaching the side of the array for the largest FOV ($\sim$ single detector shift). Together with Aleksander Krupiński-Ptaszek, we measured neurons stained with thy1-GFP in a brain slice. Figure 3.6 illustrates the comparison of the signal images acquired with PMT (Fig. 3.6 a), and with SPAD23 (Fig. 3.6 b). The presented images are averaged over five scans, and the signal from the SPAD23 is summed across the entire detector array (23 SPADs). Worth noting is that SPADs are binary detectors, meaning they either detect a photon or do not. In contrast, the PMT signal can be proportional to the fluorescence intensity, providing greater contrast than binary detection. In the brightest region, SPAD23 detected on average only one photon (per whole array), which highlights how weak the descanned signal is.

This experience led to a broader conclusion: "confocal + two-photon" is, in most cases, a bad idea. The central virtue of two-photon excitation is that it rejects out-of-focus signal at the excitation stage. Adding a confocal pinhole and, by extension, a d-scanned ISM just reduces the total detected signal and turns to the ballistic light.

3.4 Scanning with the Bessel Beam

Because my two-photon microscope is flexible and open, I also experimented with modifying the excitation path to increase imaging throughput. In particular, I tested two-photon excitation with a Bessel beam instead of a standard Gaussian focus [96]. The idea follows reports of volumetric calcium imaging using elongated foci [96–98]: neurons in the brain are relatively sparse in 3D, while calcium imaging benefits from seeing as many neurons as possible at once. Since it is impractical to extend the 2D field of view indefinitely for technical and sampling reasons, the idea is to project a sparse 3D distribution of neurons onto a single 2D frame, thereby increasing the number of simultaneously imaged cells. The technical route is to replace the tight focus in a scanning microscope with a "needle-like" focus that extends along z. This elongated focus is the hallmark of a Bessel beam and is particularly attractive under multiphoton excitation, as the side lobes of the Bessel function are then suppressed relative to the strong central lobe.

The Bessel beam in the microscope is obtained by illuminating the objective's back focal plane with a ring [96]. The Fourier transform of a ring is approximately J_0 profile whose lateral width remains diffraction-limited when the ring fills the entrance pupil of the objective. In practice, one creates the ring by placing an axicon in the excitation path; the axicon converts the input beam into a cone of light that, after "colimation" with a lens, creates a ring in the lens focus.

My first tests used the axicon (AX1205-B) alone to generate the ring, but the resulting Bessel focus quality was unsatisfactory. There were strong azimuthal nonuniformities and stray structure that translated into artefacts in the excitation PSF and, therefore, the images. I added an annular aperture (Thorlabs R1CA1000) after the axicon to spatially filter the cone and define a clean ring at the objective pupil. A simple telescope adjusted the ring radius so that the ring just filled the back aperture, which gave the best lateral resolution for a given objective. With this refinement, the expected needle-like focus appeared, and the concept worked as intended.

Despite this, routine Bessel-beam imaging proved impractical on our in-vivo platform. First, the annular aperture rejects a significant fraction of the power, so the required input power of the laser was the maximum it could deliver (around 1.5W). Second, proper ring formation is alignment-sensitive: the annular aperture must be well centred with respect to the axicon, with even small drifts degrading the PSF quickly. While a trained user can realign in 1 minute, this is error-prone for an end user and requires regular retuning. Third, the GRIN lenses used to image neurons deep in the brain introduce aberrations that further distort the Bessel beam. Based on feedback from dr Łukasz Bijoch, who performed experiments with a living mouse, the power level posed a risk of harming the mouse, while the incremental gain of visualising a few extra neurons did not justify the operational complexity and safety concerns. The comparison of neurons imaged ex vivo with a Bessel beam and with a simple Gaussian focus is shown in Figure 3.7. Although there are a few cell somas better visible with the Bessel beam (encircled with red in Fig. 3.7), the signal is weaker, and the background is strongly elevated, compared to scanning with the Gaussian beam.

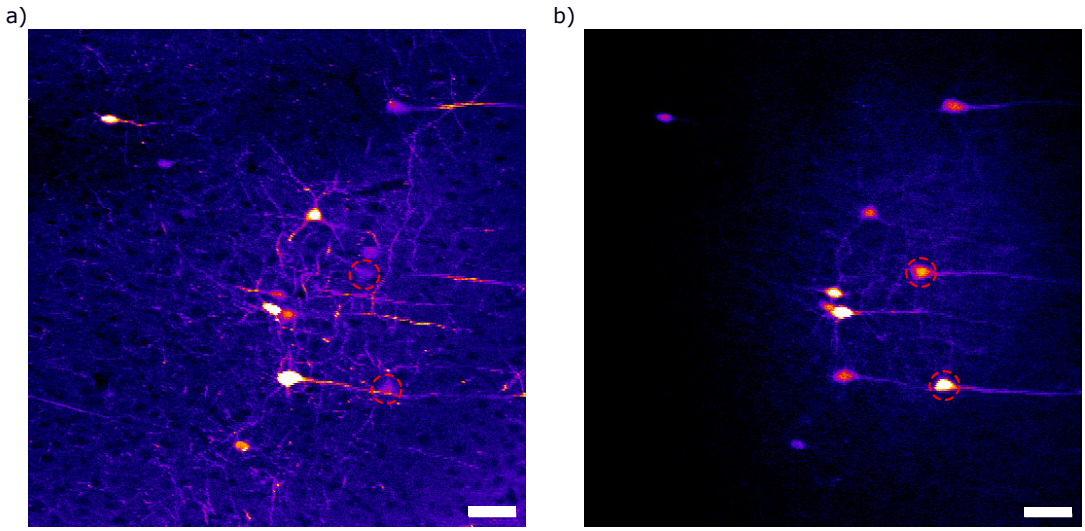

Figure 3.7: The comparison of scans performed with the Bessel Beam and the Gaussian beam. a) is the result of the scan with the Gaussian beam. The contrast of the image and the background is elevated to show the weak signal from the out-of-focus neural cells encircled with red. These somas are clearly visible in the image obtained with scanning with the Bessel beam (b).

For these reasons, we removed the Bessel module from the "corridor" in the excitation path. The module consisted of an axicon mounted in a translational (y–x) mount, a relay lens to set the ring radius, and an annular aperture mounted in an x–y mount. All components were assembled in a 30 mm cage system on two flip mounts, allowing the entire branch to be inserted or bypassed reproducibly. In practice, insertion was repeatable about five times before a touch-up alignment was needed. I also tested phase mask extensions instead of an axicon, all giving similar results: slightly extended focus at the cost of much higher excitation power.

3.5 In-Vivo Imaging of Neural Activity

I have heard that some physicists are this kind of people, who think they can become experts in any field. Unfortunately, I cannot say that I am an expert in the studies of the mouse brain conducted in the Nencki Institute of Science. In this section, let me briefly describe the outcome of the cooperation with Lukasz Bijoch, Justyna Wiśniewska, Karolina Hajdukiewicz, and Anna Beroun ([54]), and I will do my best to make it understandable, but I will hold from drawing more conclusions that the principal investigators did. Let's begin with the popular motivation of this study: Many addictions, strong ones (e.g., from cocaine) or some milder ones like those from sugar, are thought to be connected to dopamine and dopamine-sensitive neurons. Such neurons are widespread throughout the brain; in particular, recent studies [99–104] revealed that they are also present in part of the brain called the central amygdala. The central amygdala is a part of the brain associated with decision-making; thus, this study aimed to determine whether targeted silencing of

a specific neuronal population can mitigate addictive behaviour. In our study, we focused on two distinct classes of neurons in the central amygdala that are sensitive to dopamine: DRD1 and DRD2 populations. The research thesis was that the one population is responsible for so-called appetitive behaviour – they are more active when a positive stimulus is presented. In comparison, the others are more active in response to some aversive stimuli. To measure that, one needs to have a way to image the neural activity, and to measure it deep (the central amygdala is located around 2 mm beneath the brain surface).

GCaMP for activity measurement

Neurons communicate with each other with voltage impulses. To measure these impulses, special proteins were developed. There exist proteins that measure voltage directly [105, 106], but another approach is to measure the chemical cause of the increase in electric potential, namely, the increase in the concentration of Calcium ions in the neural cell [107]. With specially engineered proteins, it is possible to quench the fluorescence if there aren't many calcium ions in the vicinity of the protein. At high calcium ion concentration, fluorescence becomes significantly more intense, and changes in brightness can be used to assess neural activity. The proteins that generate this fluorescence signal are called GCaMP and are produced by specific cells after targeted viral infection.

GRIN lens

At depths as large as 2 mm, there is no non-invasive method that can provide neural activity imaging with subcellular resolution. In such cases, imaging is being done by inserting a thin GRIN lens to reach the desired structure. A GRIN lens is a lens that utilises radially changing refractive index, thus acting as a lens without any curvature at the surfaces perpendicular to the optical axis. Grin lenses can then be relatively long (e.g 4 mm), and act as a relay for the microscope focus (like a 2f system).

3.5.1 Results

In my opinion, the most interesting result from the measurements with my microscope is the observation that there is indeed a correlation between the activity of certain groups of neurons in the central amygdala upon different stimuli. It can mean that this part of the brain, even though being primitive, distinguishes what is physiologically pleasing (cocaine and sugar) or not (bitter taste of quinine). In Figures 3.7 and 3.8, the data gathered by Lukasz Bijoch with my TPSM is presented. The figures are packed with information; however, I will try to explain everything in the simplest possible terms and break this complex experiment into smaller chunks.

As mentioned, we examined two populations of neurons in the central amygdala, namely DRD1 and DRD2, and the influence of cocaine and sugar. Let's begin with cocaine.

Cocaine studies (Fig. 3.7)

The experiments were conducted such that the mouse was first habituated – got used to the GRIN lens implemented, the experimental room, and the experimental conditions. Later, a control injection of solution with saline was performed, and the baseline sample of neural activity was taken. The recording of neural activity lasted around 20 minutes and began right after the injection. In subsequent days, the activity experiments were conducted after cocaine injection (2nd, 3rd and 5th days), with another control saline injection on the 4th day. The neurons in the central amygdala of a certain type of DRD1 and DRD2 were stained using GCaMP8m calcium indicator. From the time-traces of intensity from particular cells, the average firing rate of each cell was calculated. Later analysis revealed that DRD1 neurons increase their activity with cocaine. On the other hand, the DRD2 neurons decrease their activity during the first-time cocaine injection, presenting the opposing effects of cocaine on these two populations of neurons. However, the effect of decreased activity for DRD2 neurons was visible only during the first time injection and returned to the level before cocaine injection in subsequent days. Extremely compressed figure 3.7 encapsulates that finding. As the complex description of this figure in the main text would hide the main message, I leave a very detailed figure caption explaining every panel.

Sugar and Quinine studies (Fig. 3.8)

Similarly to cocaine, mice were prepared for neural activity imaging for 20 minutes. This time however, instead of injections, the solution of sucrose or quinine was pumped to a licking ports. The time when the mouse licked the solution was established based on the recordings of the mouse's facial expressions (the licking timestamp was precisely determined by machine learning software), and comparison with the TPSM was possible due to the proper synchronisation of the TPSM with the camera recording the facial expressions. On average, DRD1 cell activity decreased after sugar consumption, while DRD2 activity increased. Additionally, the DRD2 cells increased their activity just before the lick, with the following large dip in activity right after the lick.

Again, describing the figure in detail in the main text would be disruptive for the coherency of narration, so the detailed explanation of the figure is placed as a precise and descriptive caption.

It is quite odd that from these studies we could not draw any straightforward conclusions, simplifying the whole complicated situation. This study showed me that sometimes the world is not as simple as I wanted it to be, which can be intimidating. Fortunately, it leaves room for endless exploration.

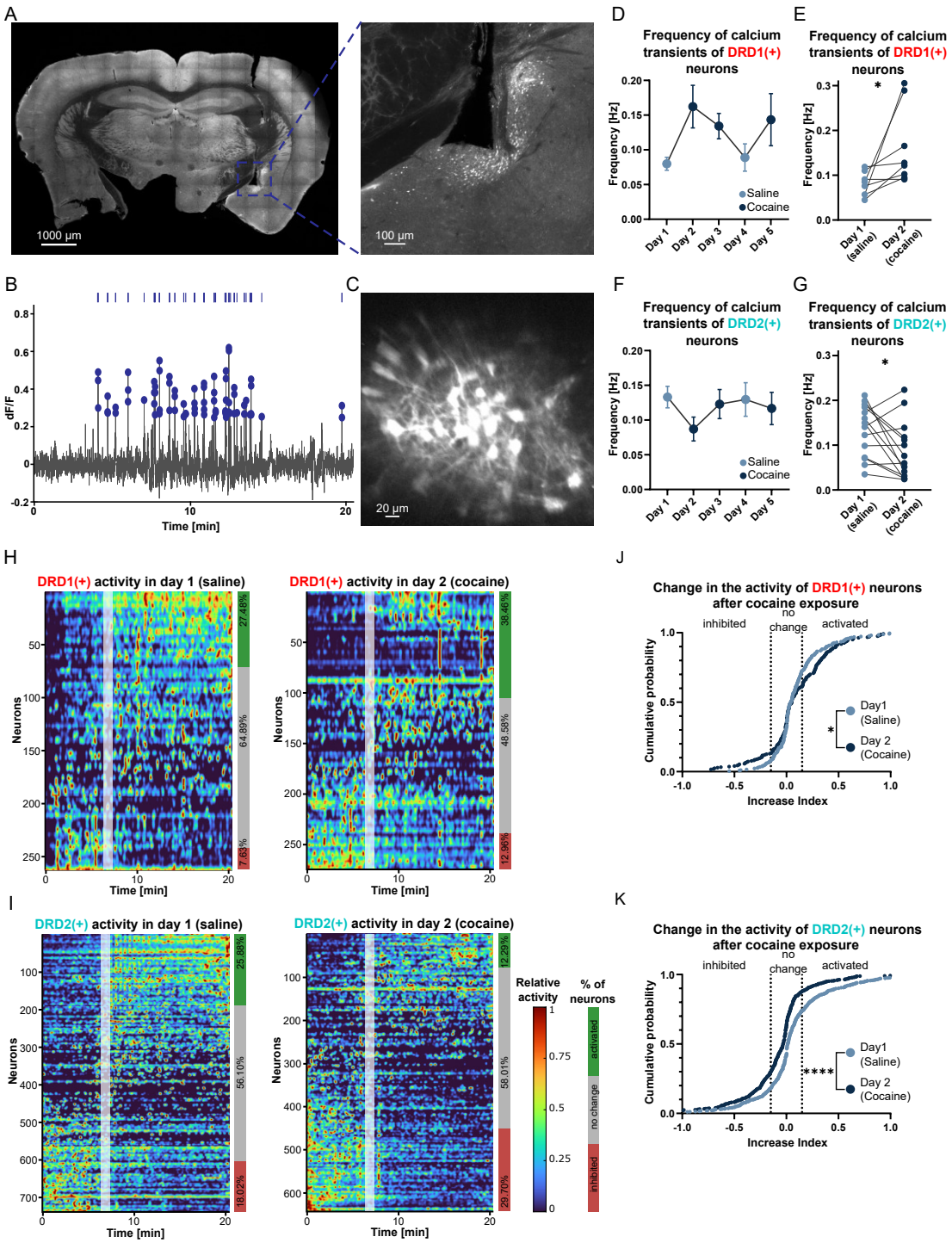
A
1000 µm
100 µm
B
dF/F
Time [min]
C
20 µm
D
Frequency of calcium transients of DRD1(+) neurons
Frequency [Hz]
Saline
Cocaine
Day 1
Day 2
Day 3
Day 4
Day 5
E
Frequency of calcium transients of DRD1(+) neurons
Day 1 (saline)
Day 2 (cocaine)
F
Frequency of calcium transients of DRD2(+) neurons
G
Frequency of calcium transients of DRD2(+) neurons
H
DRD1(+) activity in day 1 (saline)
DRD1(+) activity in day 2 (cocaine)
Neurons
Time [min]
27.48%
64.89%
7.63%
38.46%
48.58%
12.96%
J
Change in the activity of DRD1(+) neurons after cocaine exposure
inhibited
no change
activated
Cumulative probability
Increase Index
Day1 (Saline)
Day 2 (Cocaine)
I
DRD2(+) activity in day 1 (saline)
DRD2(+) activity in day 2 (cocaine)
25.68%
56.10%
18.02%
12.29%
58.01%
29.70%
Relative activity
% of neurons
activated
no change
inhibited
K
Change in the activity of DRD2(+) neurons after cocaine exposure

Figure 3.7: The results of calcium imaging from [54]. On a patched microscope photo of the brain slice (A), the examined amygdala region is visible and marked with a blue square. In the zoom-in image, an empty space left from the removed GRIN lens can be seen. Beneath, and around that empty space, the neurons filled with fluorescent dye (in white) can be distinguished, and some of them were imaged through a GRIN lens (C). If we plot the fluorescence intensity trace from a single cell, we'd obtain an exemplary activity trace (B). We can create time spectrograms containing activity frequency calculated on a 3 s interval and place them on a single heat map (H&I), combining the activity of all imaged neurons (also from different mice). Each activity is normalised by the value of the highest frequency occurring for a particular cell during the whole session. These heatmaps have a white rectangle marking the onset of the seventh minute. After around 7 minutes from the injection, the pharmacological effects of cocaine, as increased locomotor activity or dilated pupil, started to show up. When measuring the change of neural activity, this 7-minute threshold was taken into account. Comparison of the mean frequency after the cocaine/saline injection revealed that the mean activity of DRD1 neurons increased with cocaine. On the other hand, the DRD2 neurons decrease their activity during the first-time cocaine injection, presenting the opposing effects of cocaine on these two populations of neurons. However, the effect of decreased activity for DRD2 neurons was visible only during the first time injection and returned to the level before cocaine injection in subsequent days. The mean neural activity for the particular day is presented in D, F. The difference in activity between 1st and the second day averaged within a single animal for all the researched mice is presented in E and G. It was also possible to spot particular neurons that contributed the most to the changed activity. For this, the relative increase of the mean activity before and after the 7-minute threshold was established. More than half of the imaged neurons did not change their activity after the injection. The red-grey-green bars at the sides of the activity heatmaps H&I show the percentage of the neurons that changed their activity in the whole batch (red – relative activity decrease by more than 0.15, grey – no change, green – relative activity decrease by more than 0.15). Plots J and K show the cumulative probability that the relative change of intensity (here: Increase Index) is smaller than a certain value. In J it can be interpreted that after cocaine injection, some DRD1 decrease their activity, but more, increase it substantially with respect to saline control. In K, the cumulative probability plot points that there are higher chances to find cells which are less active after the cocaine injection with respect to the control sample. "*" on E,G,J depicts statistical significance with a p-value smaller than 0.05. In case of K, the p-value is smaller than 0.0001. The statistical tests performed in E, G were paired t-tests, while in J, K – Kolmogorov-Smirnov tests. Figure credit: Lukasz Bijoch, adopted from [54]

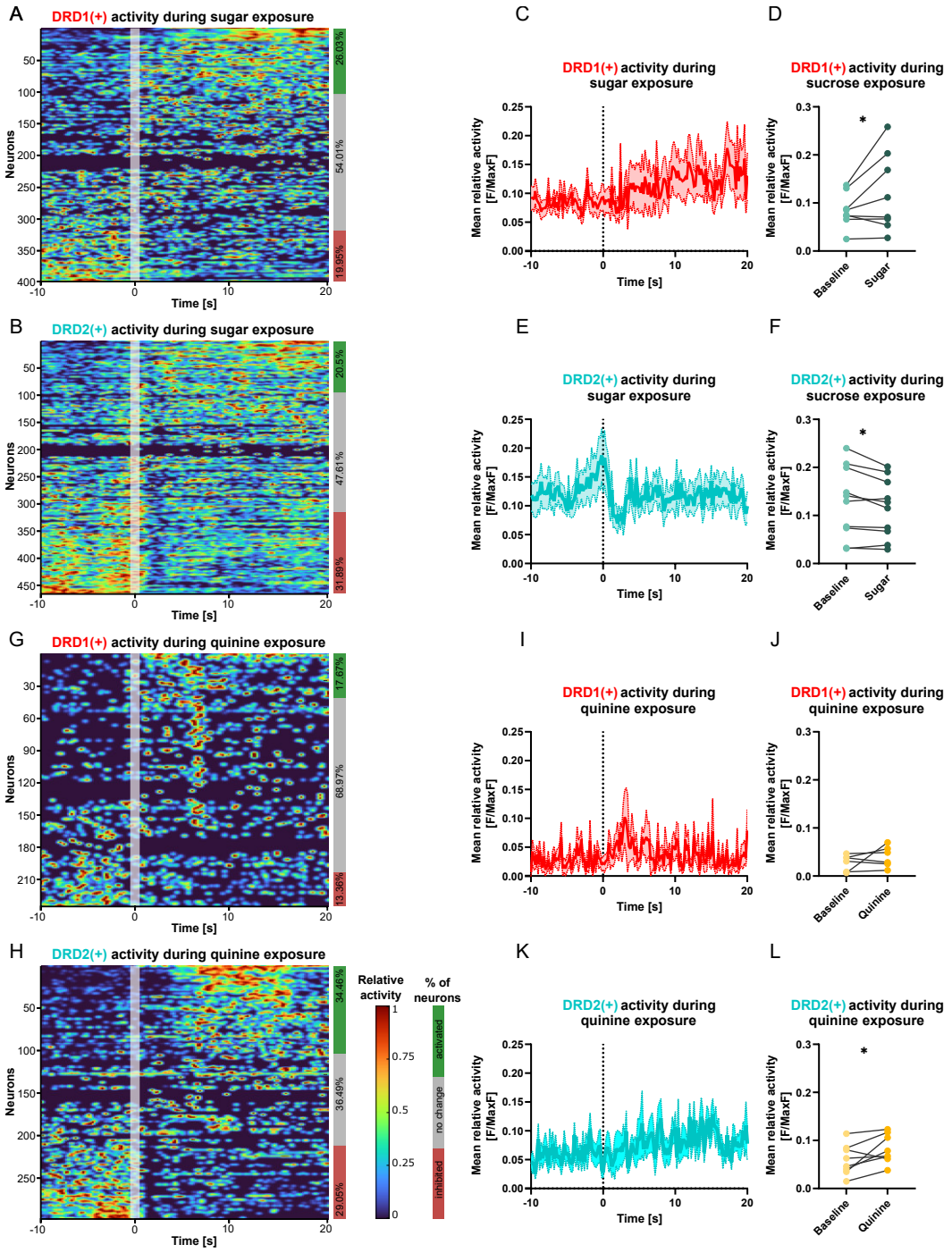
A
DRD1(+) activity during sugar exposure
B
DRD2(+) activity during sugar exposure
C
DRD1(+) activity during sugar exposure
D
DRD1(+) activity during sucrose exposure
E
DRD2(+) activity during sugar exposure
F
DRD2(+) activity during sucrose exposure
G
DRD1(+) activity during quinine exposure
H
DRD2(+) activity during quinine exposure
I
DRD1(+) activity during quinine exposure
J
DRD1(+) activity during quinine exposure
K
DRD2(+) activity during quinine exposure
L
DRD2(+) activity during quinine exposure
Neurons
Time [s]
Mean relative activity [F/MaxF]
Baseline
Sugar
Quinine
Relative activity
% of neurons
activated
no change
inhibited
26.03%
54.01%
19.96%
20.5%
47.61%
31.89%
17.67%
68.97%
13.36%
34.46%
36.49%
29.05%

Figure 3.8: Results of Calcium activity imaging of DRD1 DRD2 neurons under sugar and quinine exposure. A, B, G, and H are the spectrograms of cellular activity. The frequency was established on a 3 s basis from 10 Hz imaging (due to averaging), and normalised by the maximum value for a particular cell creating each heat-map. A white rectangle on the heat maps depicts the timestamp of licking the given 7.5% sucrose solution or 0.01 mM quinine solution. The licking timestamp was recovered from the mouse facial expression recording. With red-grey-green rectangles on the side of the spectrograms, the grouped population of neurons that decreased (red), did not change (grey) or increased (green) their relative activity after the stimuli with respect to the time before the stimuli. The threshold for every category was 0.04 of the relative frequency change. In C, E, I, and K, the means or relative activity are plotted, with the standard deviation region depicted with higher transparency. Interestingly, in E there is a visible increase of activity of DRD2 neurons just before the lick, followed by a sudden decrease after the lick consistent across all the measured neurons. Such a characteristic is not visible with quinine licking. On average, the activity of DRD1 neurons increases after sugar consumption, while the activity of DRD2 neurons decreases. In contrast to positive, sucrose stimuli, the exposure to negative stimuli – quinine – increases the activity of DRD2 neurons. The statistical tests did not confirm the inverse or the same thesis for DRD1 neurons. The individual averages for the mean relative activity are shown in D, F, J, and L. In D, F, and L, the statistical differences were measured with a paired t-test, resulting in a p-value smaller than 0.05, depicted with "*" on the plots. Figure credit: Łukasz Bijoch, adopted from [54].

Chapter 4

Two-photon Wide-field – Temporal Focusing

In this chapter, I will describe the combination of two methods – Temporal Focusing (TF) and Super-Resolution Optical Fluctuation Imaging (SOFI). Although this may seem quite an easy combination (which is why I wanted to pursue this idea after my Master's thesis), what I hope will be interesting in this chapter is the physics underlying both techniques.

4.1 Introduction to Temporal Focusing

In my first year of studies, I was surprised by the following statement I heard during a lecture: the fact that the night sky is dark is evidence that the Universe is either expanding or finite. Even though it is completely unintuitive, the reasoning is simple. Assume a uniform, average density of stars that emit light, and recall that the intensity from a point source falls off as $1/r^2$ (r is the distance from the source). If we now integrate the contribution of light from all the stars over an infinite, uniform Universe, the radial r^2 part of the Jacobian from the volume element cancels the $1/r^2$ intensity decay, and the integral diverges at infinite limits. In result, the night should be as bright as a day.

This methodology has an analogue in fluorescence microscopy of thick, volumetric samples. If we excite the entire volume at once, the volume scaling vs inverse square law accumulates an overwhelming out-of-focus signal, losing the ability to image any structures or strongly elevating the background. Therefore, three-dimensional imaging requires sectioning. By sectioning, I mean the ability to reject out-of-focus light so that only the plane of interest contributes to the recorded image – in our astral analogy, sort of a red-shift causing the distant stars (emitters) to not contribute to the signal that we are interested in.

Figure 4.1 illustrates the core issue: under one-photon excitation, the entire sample volume is excited, making, e.g., wide-field imaging difficult due to out-of-focus background. In contrast, the main character of this chapter – temporal focusing restricts excitation to molecules located near the focal plane, thereby providing intrinsic optical sectioning.

In the previous chapter, TPSM already provided sectioning; however, here,

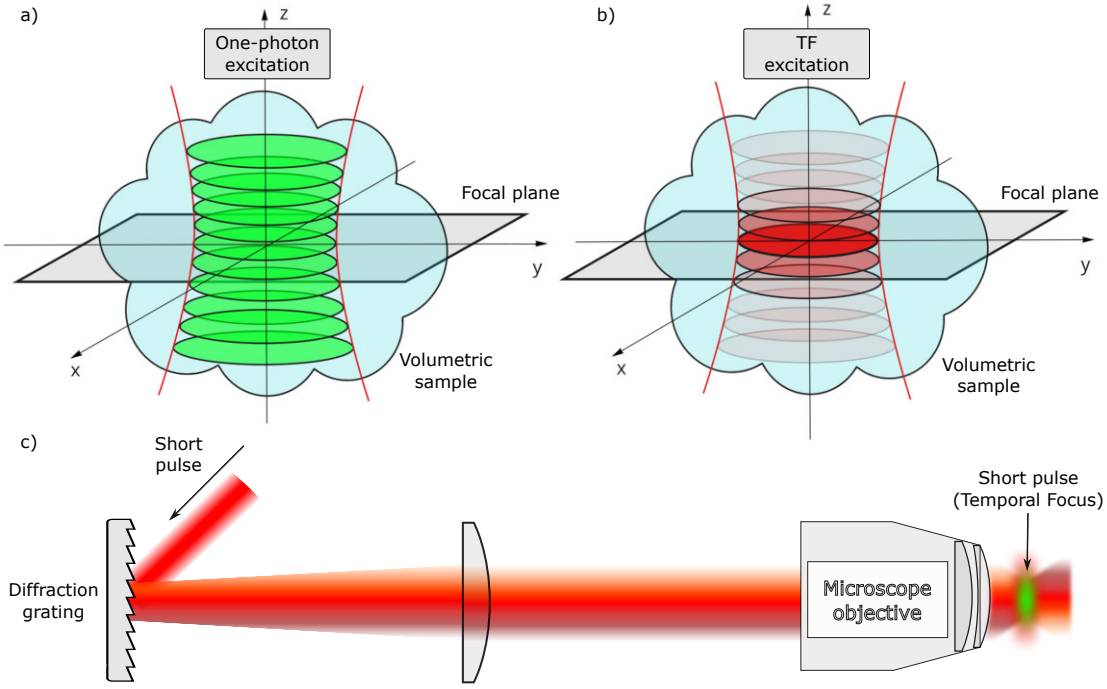

Figure 4.1: Problem solved by Temporal Focusing (TF) – sectioned wide-field excitation. (a) One-photon excitation (green) propagating along the optical axis (z) through a volumetric sample (blue). Fluorophores throughout the entire volume are excited, generating a strong out-of-focus background. (b) Temporal focusing excitation (red), which produces efficient excitation only for molecules located near the focal plane. The (x, y, z) axes indicate the lateral and axial directions, with z being collinear with the objective's optical axis. (c) The scheme of the temporal-focusing setup. A short pulse reflects from a diffraction grating. The first-order diffraction beam goes through a 4f setup consisting of a lens and a microscope objective. Spectral pulse components are split spatially, which elongates the pulse. After the objective, the pulse becomes short again, only in the temporal focus. This provides axially confined two-photon wide-field excitation.

I want to introduce another method of two-photon excitation that does it without the need for expensive scanning modules. This method is called Temporal Focusing (TF) [108, 109]. Temporal focusing is designed to excite fluorophores efficiently only in the plane of interest, but importantly – a relatively large wide-field area is being illuminated at one time. TF may be attractive for 3D microscopy for two reasons. First, bleaching is concentrated in the region we image, rather than throughout the volume. Second, TF operates in wide-field, so only the axial coordinate (z) needs to be scanned for 3D imaging; moreover, in the TF setting, this scan can be fast [110].

At first glance, it is not obvious how one can obtain such sectioning in a one-photon wide-field microscopy. For example, SIM does it (in a very non-straightforward way). By accident, the experimental setups for SIM and TF are similar, but this time, following the main theme of the thesis, we will use a nonlinear excitation.

The core idea is to change the pulse duration along the direction of propagation

in the sample so that the pulse is long everywhere, except in the image plane, where it is short. Shorter pulses produce a higher two-photon excited fluorescence signal at a constant pulse energy. Therefore, by controlling the pulse length as a function of z (no energy is lost during propagation), we control where the two-photon excitation is efficient. Such pulse-width control can be achieved by maintaining the spatial extent of the excitation beam, enabling wide-field (WF), sectioned excitation.

TF in more detail

Practically, we change the pulse length by introducing geometrical (spatio-spectral) dispersion with a diffraction grating placed in the excitation path of a wide-field microscope (see schematic in Fig. 4.1 c). The grating surface is imaged onto the plane where we want to excite the fluorophores. Such imaging of the grating causes the pulse to be spatially chirped and hence temporally elongated away from the grating's image plane, whereas at the plane conjugated to the grating, the pulse is shortest. The pulse width is being "imaged" by the $4f$ system that provides direct phase imaging.

In phase language, the pulse is shortest when all wavelength components arrive in phase; when their phases differ, the pulse broadens. Mathematically, temporal broadening is driven by the second derivative of the spectral phase: $\frac{d^2\phi(\lambda)}{d\lambda^2} \neq 0$. In TF, one can analytically compute $\phi(\lambda)$ imposed by the grating–4f combination, and estimate the pulse duration change away from the temporal focus. Under standard assumptions (Gaussian spectrum, transform-limited input pulse), imaging the grating onto the sample with a 4f system of angular magnification M and using a grating of line density N yields an approximate pulse-width expression (see my Master's thesis [82], and supplement of [55] for the detailed derivation):

$$\sigma_t(z) \simeq \sigma_{t_0}\sqrt{1+\left(\frac{nN^2M^2\lambda_0^3\Omega^2}{4\pi c^2}(z-z_0)\right)^2}, \tag{4.1}$$

with σ_{t_0} being the Fourier-limited pulse width, λ_0 is the central wavelength of the pulse, Ω is the spectral width, z_0 is the position of the temporal focus, and n is the refractive index of the medium in which the temporal focus is. Equally important for design is the axial sectioning for two-photon excitation, which can also be derived, being:

$$F(z) \propto \left[1+\left(\frac{nN^2M^2\lambda_0^3\Omega^2}{4\pi c^2}(z-z_0)\right)^2\right]^{-\frac{1}{2}} \tag{4.2}$$

One important thing, not apparent in the final equation but evident in the complete derivation using dispersion, is that the geometric dispersion introduced by the TF setup can compress the pulse, even if the pulse is chirped at the grating (introducing additional chirp shifts the temporal focus). The axial location of the temporal focus can be shifted by adding negative or positive dispersion before the grating. Figure 4.2 illustrates the axial shift of the temporal focus upon adding dispersion in the laser-built-in compressor. The theory using the paraxial approximation fits the experimental results well, even though a high-NA objective (NA = 1.4) was used

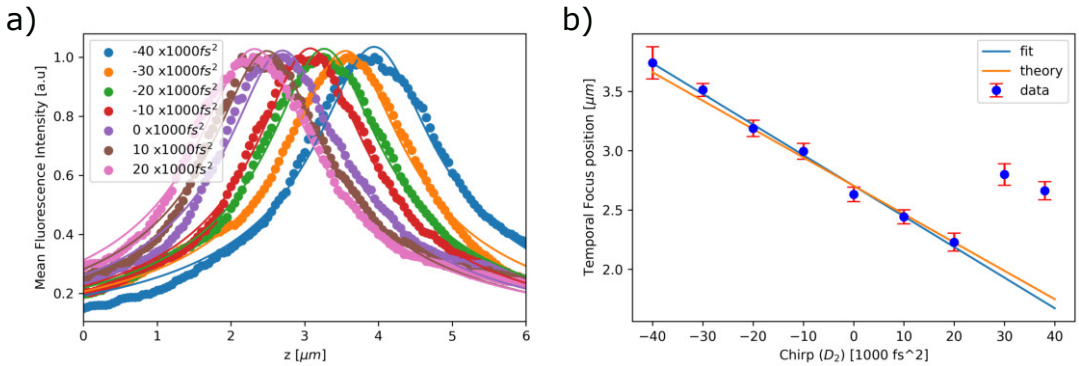

Figure 4.2: Sectioning in TF and the axial shift of temporal focus with dispersion. a) The fluorescence from a thin sample of Quantum Dots spin-coated with PMMA was recorded for different positions with respect to the objective. For every iteration, we introduced a different dispersion value using the laser's built-in compressor. We fitted $(1 + a(z - z_0)^2)^{-\frac{1}{2}}$ to get z_0 shift that is visible in plot b). We fitted a linear function to the data (blue) to get the offset. The orange line is the theoretical shift, with the slope determined by the dispersion considerations. The two anomalous data points are probably due to problems with the built-in laser compressor. Adopted from Supplementary information of my work: [55])

for the experiments. The position of the temporal focus, and, in general, the shape from equation 4.2, can be measured experimentally by translating a thin sample containing fluorescent dyes and measuring the overall fluorescence intensity at each position z.

TF and scanning

Although we argued that the whole point of TF was to abandon scanning, there is one crucial extension of TF, namely TF-line scan [111]. Instead of wide-field illumination, the excitation is focused in time and in space. The resulting line is then scanned across the sample. Such implementation provides tighter sectioning than TF alone, while focusing the laser light in one dimension reduces the laser power required for two-photon wide-field excitation. For practical imaging purposes, line-scan is then more optimal, and I also built and used it to combine with SOFI.

4.2 Introduction to SOFI

When we talk about imaging, we usually describe the signal at each pixel simply as an intensity value. Such a "convention" is reasonable because intensity is an optical quantity we can easily measure, e.g., with cameras. It is, however, not always the optimal quantity for forming an image with the highest possible spatial resolution. In Super-resolution Optical Fluctuation Imaging (SOFI), the image is built not from intensities but from correlations of intensity over time [66]. The most intuitive and straightforward to understand for physicists is the second-order correlation, which is

variance. Looking at the intensity variance rather than the mean intensity increases resolution by a factor of $\sqrt{2}$ relative to the diffraction limit [112].

For SOFI to work, the fluorescence molecules must "blink", meaning that each dye or emitter shows random, independent fluctuations of brightness in time. If emitters fluctuate independently, their temporal correlations can be used to disentangle overlapping PSFs and thereby improve resolution. To see this, let us sketch the derivation of such a second-order (variance) SOFI signal. We model the camera signal as a sum over emitters at positions $\mathbf{r}_k$, each imaged by the system PSF: $PSF(\cdot)$ and modulated by a stationary, random brightness trace $s_k(t)$:

$$I(\mathbf{r},t) = \sum_{k=1}^{K} s_k(t)\, PSF\Big(\mathbf{r} - \mathbf{r}_k\Big). \tag{4.3}$$

The movie $I(\mathbf{r},t)$ is thus the superposition of fluctuating PSFs. When we measure such a movie, we can measure pixel-wise mean in time:

$$\langle I(\mathbf{r},t)\rangle_t = \sum_{k=1}^{K} \langle s_k(t)\rangle_t\, PSF\Big(\mathbf{r} - \mathbf{r}_k\Big), \tag{4.4}$$

and variance:

$$\mathrm{Var}\{I\}(\mathbf{r}) = \langle I(\mathbf{r},t)^2\rangle_t - \langle I(\mathbf{r},t)\rangle_t^2. \tag{4.5}$$

Let us focus on the first term of the variance $\langle I(\mathbf{r},t)^2\rangle_t$, and write it explicitly:

$$\langle I(\mathbf{r},t)^2\rangle_t = \Big\langle \sum_{k=1}^{K}\sum_{l=1}^{K} s_k(t)s_l(t) PSF\Big(\mathbf{r} - \mathbf{r}_k\Big) PSF\Big(\mathbf{r} - \mathbf{r}_l\Big)\Big\rangle_t. \tag{4.6}$$

Because the $s_k(t)$ are independent across emitters, cross-terms $\langle s_k(t)s_l(t)\rangle_t - \langle s_k(t)\rangle_t^2$ for $k \neq l$ average to zero over a sufficiently long time series. Mathematically, it is equivalent to inserting $\delta_{k,l}$ into equation 4.6. That is the core of SOFI, and also there lies its beautiful simplicity, after which the resulting variance image at the camera is:

$$\mathrm{Var}\{I\}(\mathbf{r}) \approx \sum_{k=1}^{K} \mathrm{Var}\{s_k\} \Big[PSF\Big(\mathbf{r} - \mathbf{r}_k\Big)\Big]^2. \tag{4.7}$$

Note that, in this variance image, the PSFs from particular emitters are raised to the second power. Raising the excitation PSF in TPSM to the second power increases the resolution; similarly, raising the detection PSF for particular emitters increases the resolution by $\sqrt{2}$.

Such mathematical treatment (cancellation of cross terms and raising the PSF of a single emitter to a certain power) applies not only for variance, but also for higher-order correlations. Higher-order SOFI increases the resolution by $\sqrt{N}$ with N being the correlation order. E.g., Third-order correlations that still remain practical on modern cameras and further improve resolution (by $\sqrt{3}$ with respect to diffraction-limited PSF), but they demand longer acquisitions to average out higher-order cross-moments, and they are more sensitive to artefacts stemming from drift and photobleaching. In practice, well-tested software implementations (e.g., MATLAB toolboxes [113] and IGOR [114] procedures developed for SOFI) make second- and third-order processing straightforward once the raw movie is stable.

An essential advantage of SOFI is that it operates naturally in 3D. Correlations effectively take the PSF to N-th power, which improves the resolution in all three spatial directions. Moreover, the method reduces background, as out-of-focus fluorescence tends to be less correlated at any given pixel than in-focus fluorescence. As a result, correlation images exhibit an additional sectioning that could be particularly beneficial for volumetric samples. However, SOFI is rarely used for 3D imaging because a strong out-of-focus signal can introduce artefacts. That is why I decided to combine SOFI with TF – a simple, yet powerful combination – central to this chapter.

4.3 TF SOFI

The main results of combining TF with SOFI are presented in my article "3D super-resolution optical fluctuation imaging with temporal focusing." [55]. Here, I summarise those findings and include unpublished observations on the TF line-scan together with SOFI.

3D imaging

To demonstrate the feasibility of my combined approach on biological structures, I imaged quantum-dot-labelled rat hippocampal neurons (See Figure 4.3 a). Quantum dots are well-suited to SOFI because they blink over a wide range of timescales, including those accessible to scientific cameras. Representative results are shown in Figure 4.3. I imaged a full z-stack with 21 z-positions, each separated by about 300 nm. For each position, I recorded 300 frames in the ultra-low-noise mode of the QCMOS camera. I calculated the correlation signal for every movie to retrieve super-resolved images (Fig. 4.3 b). Figure 4.3 g shows the comparison between the cross-section from the mean intensity image and the SOFI image, where the SOFI image allows for better distinguishing the emitters. Additionally, the comparison of x-z cross-sections of mean image and SOFI (Fig.4.3 c and d, respectively) clearly presents that SOFI is capable of creating 3D images with better contrast than TF alone, making the TF-SOFI synergy particularly effective for 3d imaging (3d render in Fig. 4.3 h).

Truthful pros and cons with comparison to other methods

Only a few contemporary approaches provide an excitation-side sectioning, which is crucial for 3D imaging primarily because it limits photobleaching of out-of-focus emitters (see a notable summary of these techniques in [115]). Multiphoton techniques (e.g., TPSM) achieve sectioning naturally via nonlinearity, as discussed in the previous chapter. Another important class that I want to devote some time to here is light-sheet microscopy (one- or two-photon) [116–118]. In the light-sheet microscope, the sample is illuminated from the side, and detection is performed orthogonally. The illumination is performed, e.g., with a focused line (sheet) or a Bessel beam, which is scanned to provide axial confinement over a larger FOV. A general argument in favour of light-sheet over TF is the excitation power efficiency. In TF, the

excitation is wide-field, and a large FOV requires high excitation power, whereas in light-sheet microscopy, the excitation is line-like, which substantially reduces power requirements. TF can also operate in a line-scanning regime where the excitation power is highly reduced, however, at the cost of a slightly more complicated setup. Scanning with a line in TF still seems easier than a light-sheet setup. For experimental light-sheet setups, two geometries dominate. Dual-objective light-sheet, and an oblique illumination [119], "single-objective" light-sheet. A dual-objective light-sheet requires access to the specimen from the side, which can limit its applicability. In contrast, an oblique light-sheet is more compatible with standard sample formats, but requires two additional specialised objectives in the detection path for efficient fluorescence readout. I am leaving the opinion of what is simpler to the reader. Nevertheless, there are many commercial light-sheet systems, while the TF line-scan seems to be a niche. It is mainly because light-sheet provides sectioning with single-photon excitation, large FOVs, and CW lasers, whereas, due to the low efficiency of two-photon excitation, TF delivers small FOVs and requires femtosecond lasers for excitation. The second disadvantage could be solved by the advent of inexpensive, reliable, femtosecond, fiber, oscillators, but the problem of small FOV still awaits its solution in a more optimal and compact TF setup.

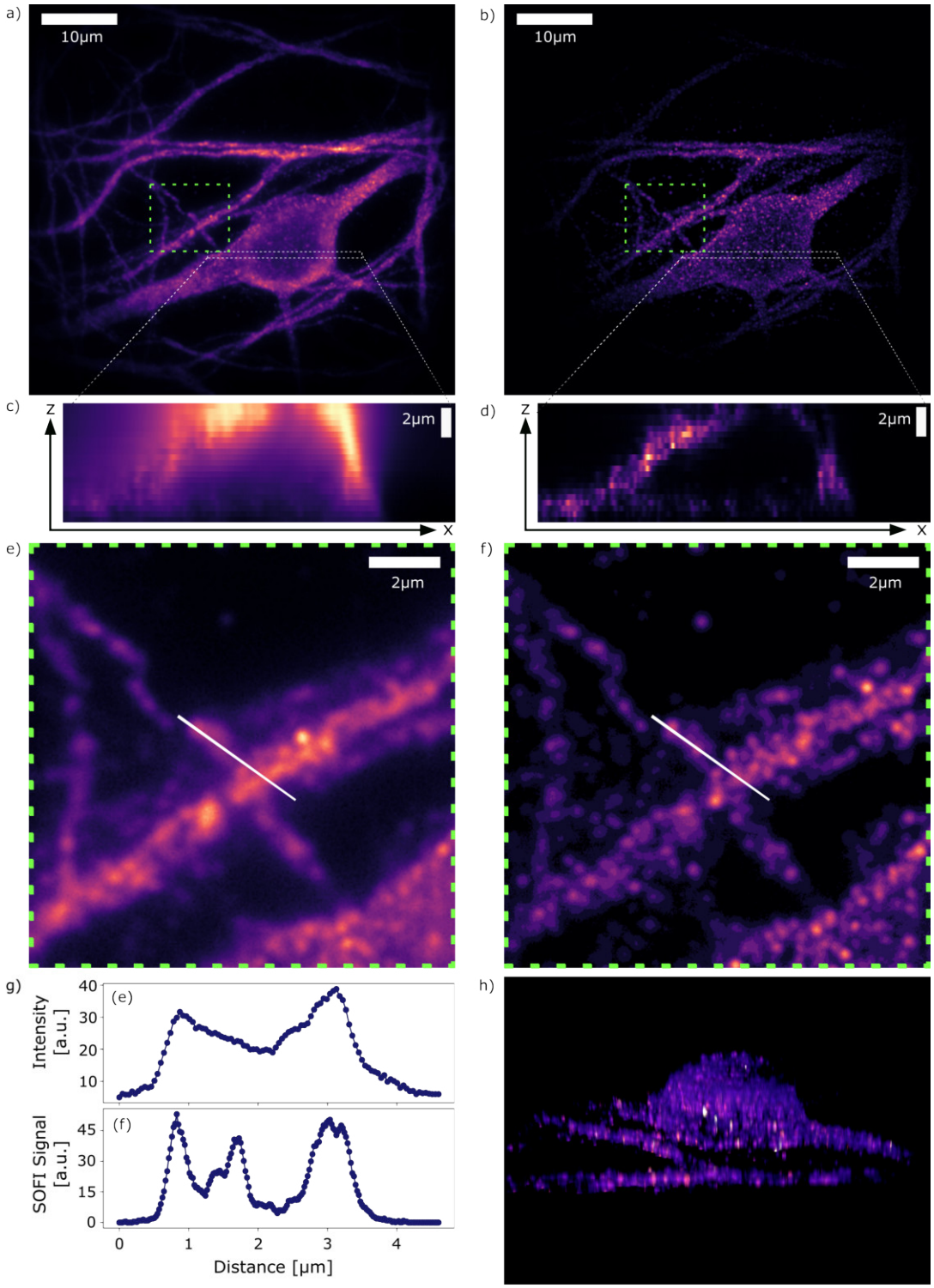

Figure 4.3: Comparison of the mean intensity images and the SOFI images of rat neurons stained with anti-MAP2 qdot-conjugated antibody obtained with wide-field two-photon excitation with Temporal Focusing. (a) and (b) display the full field of view of the mean intensity and SOFI images, respectively, revealing the soma and dendrites. (c) and (d) depict XZ cross-sections of the mean intensity and SOFI images, respectively. (e) and (f) show magnified areas of interest from (c) and (d), respectively, emphasising dendritic features. Plot (g) represents a signal along the white lines indicated in (e) and (f), illustrating the enhanced contrast and improved lateral resolution of SOFI compared to mean intensity. (h) is a 3D rendering of a neuron from SOFI images, showcasing SOFI's ability to reconstruct 3D morphology. Adopted from [55].

4.4 TF Line-scan SOFI

The motivation for testing the line-scan modality was not the effective use of power or a potentially larger FOV, but the expectation of a highly enhanced axial resolution. SOFI by itself is governed by the detection PSF, whereas line-scan TF modifies the excitation PSF. If the axial scales of the two effects were similar, they could reinforce each other. In my measurements with 100X oil objective with NA = 1.4, TF sectioning was 2.4 μm FWHM, with corresponding SOFI-TF sectioning of 480 nm. In Fig. 4.4 a, the maximal signal from TF alone is shifted with respect to the maximal SOFI signal (temporal focus is shifted with respect to the camera focus), shown here on purpose. This small shift could be the cause of the slight asymmetry in the SOFI sectioning. Worth noting is that the shift of around 200 nm still appears to influence the SOFI signal.

With the TF-LS perfectly aligned with the focus, the line-scan TF sectioning was 1.2 μm, but the SOFI-TF-Line-Scan axial sectioning was still 480 nm FWHM (See Fig. 4.4). As a result, the already strong intrinsic sectioning of SOFI could not be further tightened by adding TF or TF line-scan in terms of raw FWHM.

Despite this, the TF line-scan provided better axial confinement and also allowed for combination with SOFI, shown in Figure 4.5. A potential concern with the line-scan approach is that non-uniform excitation could introduce fluctuations, thereby mimicking a correlation signal.

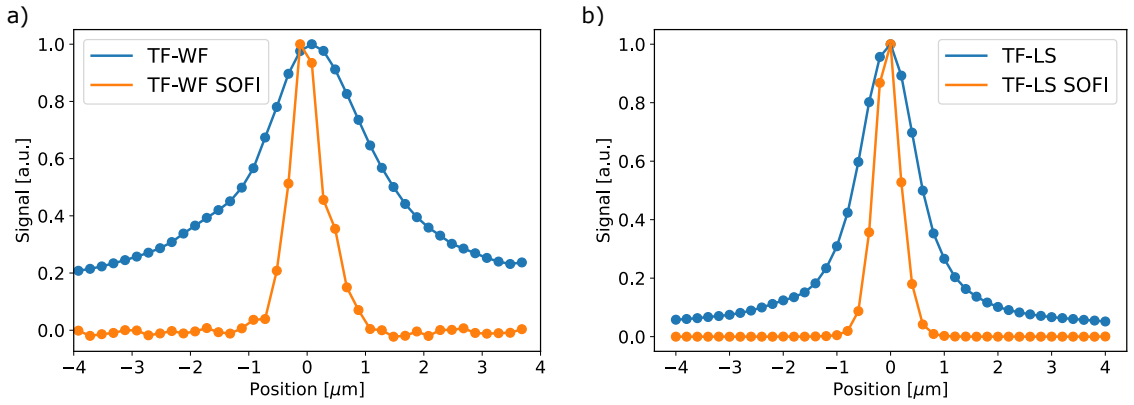

Figure 4.4: Sectioning measurements. A nearly uniform, thin sample of quantum dots spin-coated in PMMA was translated axially through the temporal focus. For each z-position, a wide-field image movie was recorded (1030 nm excitation central wavelength; 100X oil-immersion objective, NA=1.4). To obtain a single value per z, the signal was averaged over the FOV. a) the sectioning of TF alone with the full width at half maximum of 2.4 μm (blue) with SOFI signal (orange). b) the sectioning of TF line-scan with the full width at half maximum of 1.2 μm (blue) with SOFI signal (orange). The FWHMs of sectioning from TF-line-scan and SOFI were extracted from the Gaussian fits. The SOFI sectioning FWHM in a) and b) is the same and approximately 480 nm.

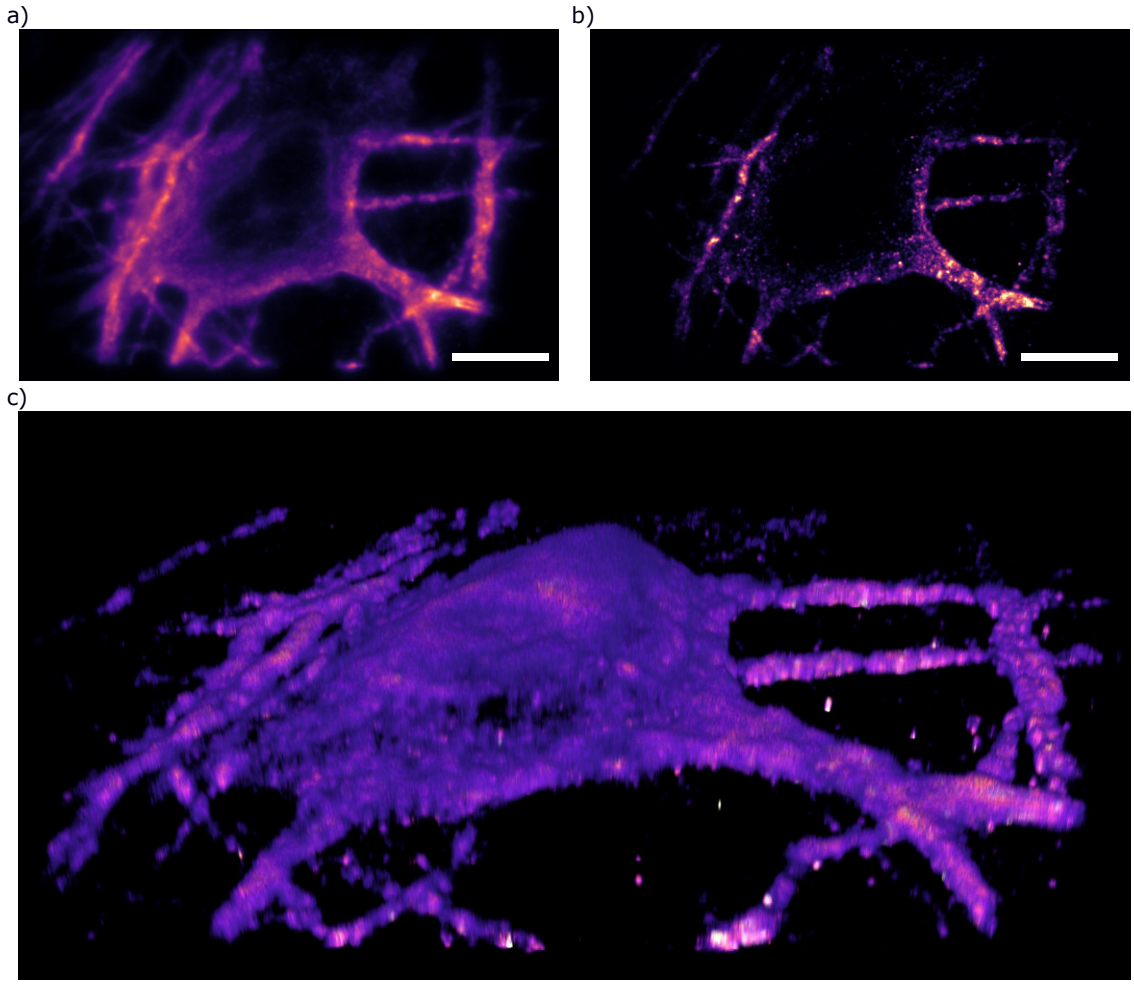

Figure 4.5: Results of imaging with TF-LS SOFI. (a) Mean-intensity image of hippocampal neural cells stained with quantum dots, recorded using synchronised acquisition between the temporal-focusing line-scan illumination and the camera. (b) Second-order SOFI reconstruction obtained from 300 consecutive frames of the same dataset, revealing enhanced structural contrast and resolution. (c) Three-dimensional rendering of the cellular structure reconstructed from the SOFI signal, using a z-step of 100 nm. The reconstructed SOFI 3D image reveals clear structural features of a single hippocampal neuron, including the soma and several dendrites. The neuron appears relatively flattened, which is consistent with the condition of the sample at the time of imaging: this measurement was performed approximately two days after sample preparation and one day after the acquisition shown in Fig. 4.3. The progressive flattening and reduced three-dimensional morphology likely indicate the onset of cellular degradation. Despite this deterioration, the TF-LS SOFI reconstruction retains sufficient contrast to resolve subcellular structures in both the lateral and axial directions. Scale bars in (a) and (b): 10 µm.

4.5 TF Experimental Setup

I built at least three iterations of the TF microscope; this section documents the latest version. The platform supports multiple modes: TF, TF line-scan, two-photon line-scan, and possible extensions with SLM for custom pulse-shaping and coherent control [120], or DMD for excitation patterning [121–123]. In Figure 4.6, the scheme of the final setup is shown.

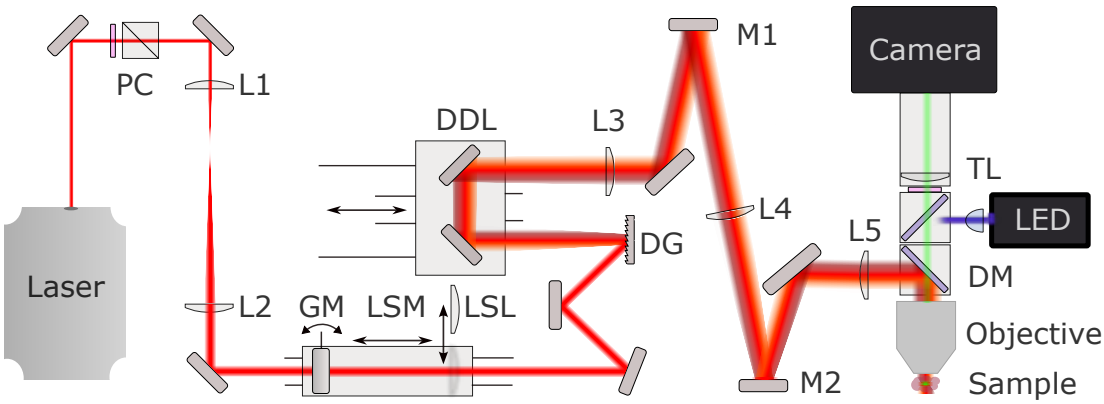

Figure 4.6: Scheme of the experimental setup for TF/TF-Line-Scan. The excitation beam from the femtosecond fibre oscillator passes through the power control module (PC), consisting of a motorised half-wave plate and a polarising beam splitter. The beam is then expanded by a telescope composed of lenses L1 ($f = 75\,\text{mm}$) and L2 ($f = 500\,\text{mm}$). Next, it is directed to the movable dovetail Line Scanning Module (LSM), where it reflects from the Galvo Mirror (GM). In the line-scanning operation mode, the beam is focused with a cylindrical ($f = 250\,\text{mm}$) Line-Scanning Lens LSL (unlike in the schematic, the LSL cylindrical lens is oriented horizontally with the power-free axis). In TF wide-field mode, the LSL lens is removed from the beam path, and the galvo mirror is disabled. The beam is subsequently routed onto a Diffraction Grating (DG, $600\,\text{lines}\,\text{mm}^{-1}$), whose normal is aligned with the first diffraction order at the central wavelength (1030 nm). The spectrally dispersed beam propagates through a Dispersion Delay Line (DDL) and is collimated by lens L3 ($f = 400\,\text{mm}$). The beam travels through L3 and L4 lenses forming a 4f imaging system with M1 mirror in the Fourier plane and M2 mirror in the grating's image plane. M1 mirror can be replaced with an SLM for spectral pulse shaping, and M2 mirror could be replaced with a DMD for patterned illumination. After reflection from M2, the beam passes through lens L5 ($f = 300\,\text{mm}$), the short-pass Dichroic Mirror (DM), and the objective. The L5 lens and the objective constitute another $4f$ system that images the grating onto the sample plane. Fluorescence from the sample is collected by the objective, routed through two dichroic mirrors and emission filters, and imaged onto the Orca Quest sCMOS sensor using a 200 mm tube lens (TL). A secondary long-pass dichroic mirror provides an additional illumination pathway for one-photon wide-field LED excitation.

2 W, 1030 nm, 200 fs, 20 MHz fiber laser (Fluence Halite 2) supplies sufficient power for TF-WF excitation while remaining turnkey and alignment-free on warm-

up. The output beam first meets a half-wave plate and a high-power PBS cube for power control. Next, a two-lens Keplerian expander increases the beam diameter to 8 mm (L1, $f = 75$ mm, L2, $f = 500$ mm). The beam then enters a custom dovetail stage carrying a periscope with a galvanometer mirror. The dovetail stage and the periscope are designed such that a cylindrical lens ($f = 250$ mm) can be inserted one focal length from the galvo mirror for line-scan operation. After the scanner, two steering mirrors direct the beam to the diffraction grating (DG with line density $N = 600$ lines·mm^{-1}). The grating angle is set so that the 1st diffraction order at 1030 nm leaves along the grating normal. The grating sits on a magnetic base to allow quick swaps to a flat mirror for non-TF tests.

The diffracted beam passes through a Dispersion Delay Line (DDL) before a 400 mm lens collimates it. The DDL is central to day-to-day usability: translating it introduces controlled geometric dispersion and gives a convenient handle for setting the precise axial position of the temporal focus. After the 400 mm lens (L3), an optical relay images the grating Fourier plane onto the objective's back focal plane. Such a relay gives the room to insert an SLM (position marked with M1 in the optical scheme) in the Fourier plane of the grating, and DMD in the grating's conjugate plane (after L4, f =300 mm in place of M2). Downstream M2, the 300 mm lens (L5) projects the dispersed spectrum of the laser to fill the entire pupil, which maximises sectioning.

The objective is mounted above a sample placed on a three-axis movable stage, with the sample attached low, close to the optical table surface for safety reasons. The objective is carried by a piezoelectric focusing stage (Mad City Labs) and coupled to the custom part with SM1 thread and inserts for cage rods. Light travelling to or from the objective is turned by a protected-silver mirror in a kinematic 45 ° cage mount (Thorlabs C45P not marked in the schematic). That mount ties into cage rods, which pass through a cube holding a dichroic mirror DM on a kinematic plate (Thorlabs: C6WR and B4C, DM: DMSP900R); the same rods connect downstream to a magnetic filter mount (DFM32R1/M). The filter cube is placed on two machined posts and bolted to the table. One side port provides 1P-WF diode excitation; the forward port carries fluorescence toward the wide-field camera. Although being compact, cost-effective, easy to assemble, and allowing to achieve lateral resolution of 274 ± 18 nm, the main body is not very stable and should be upgraded[1].

Line Scan

Line-scan operation adds one more constraint: the spatial and temporal focuses must coincide. In practice, we iterate: first translate the Line Scanning Module LSM along the dovetail to obtain a sharp physical line at the dense thin sample of the fluorophores (with the mirror replacing the grating), then refine pulse compression via the laser compressor or the DDL, until the line brightens maximally at best focus. In this modality, the objective's entrance pupil is intentionally overfilled along one axis by the "spatial" beam forming the line. In contrast, the orthogonal axis is filled by the pulse's spectral components from the grating.

[1] Listening to music on a loud-speaker resulted in focus shift along with the beat.

To mitigate the non-uniform, time-varying excitation, the scanning line must be synchronised with the camera readout. Additionally, with the proper synchronisation, one can use a rolling shutter to create a "digital pinhole" that rejects out-of-line background and sharpens resolution along the scan direction [124, 125].

4.6 Outlook for the TF Setup

My setup also leaves room for many TF extensions. First, one can place an SLM in the grating's Fourier plane to shape spectral phase and amplitude. This enables coherent control of two-photon excitation (e.g., adjusting the chirp to tune axial sectioning or compensating residual dispersion dynamically) and, more generally, programmable control of where, along z, the pulse compresses. Second, an SLM or a DMD in the grating's image plane enables patterned excitation, illuminating selected regions of interest or projecting patterns onto the desired plane. This also allows for experiments with scattering media, as TF with patterned illumination has already been shown to be robust with weakly scattering samples [121, 123].

The primary reason for discontinuing the development of the TF-SOFI setup was the challenge of sample preparation. In our implementation, we relied on quantum dots, yet staining volumetric biological specimens such as brain slices with quantum dots proved impractical. The procedure was long, prone to non-uniform penetration, and the samples degraded rapidly, creating a substantial barrier for biological imaging with TF combined with SOFI. These constraints also impeded further experiments in scattering volumetric samples, as well-prepared specimens were difficult to obtain. Importantly, the limitation stemmed from the fluorescent labels compatible with SOFI and with two-photon excitation at 1030 nm, rather than from the TF excitation scheme itself. Meanwhile, an additional and highly practical direction has emerged: the possibility of integrating fluorescence-lifetime imaging (FLIM [126]) into the TF setup.

FLIM measures the excited-state lifetime of fluorophores, providing additional information about the chemical surroundings of the imaged molecules. Lifetime depends on the local environment and interactions, so FLIM can provide more detail from almost the same data. For example, it was shown that high-speed wide-field FLIM can give the possibility to measure the brain activity of a fly [127]. [128]

Such a result was possible with an electro-optical gating [128]. A natural route toward TF-FLIM would therefore be to integrate electro-optical gating into the TF scheme, or conversely, adapt TF to such gating. An alternative approach is to employ modern SPAD-array cameras, such as SwissSPAD2 – a 512×512 array of single-photon avalanche diodes. These detectors can generate a global gate of approximately 10 ns and shift the gate position with 50 ps resolution. By stepping the gate relative to the excitation pulse, one can sample the fluorescence decay at each pixel and reconstruct the lifetime map.

Conveniently, the TF setup already operates with a 20 MHz laser, and this repetition rate provides precisely the clock signal required to synchronise a SPAD array. As a result, the timing electronics in my implementation would be straightforward. While this direction no longer targets high-resolution imaging under demanding conditions, it offers a promising avenue for obtaining valuable photophysical information

with relatively modest effort[2].

I currently co-supervise this Master's project, conducted by Aleksander Macioch, whom I also co-supervised during his Bachelor's thesis on FLIM measurements in CLSM using the SPAD23 array [129].

[2]SPAD arrays have currently very low photon detection efficiency (less than 15%), so such an experiment would still be rather a proof of concept, waiting to be applied for the development of better detectors.

Chapter 5

Nonlinear Imaging with Speckle Excitation – NISE

Before jumping into this chapter, I must confess that for me it is the most interesting part of my doctoral work – a favourite child. The experiments behind it were fun to design, extremely satisfying to run, and probably the most impactful. I hope you, dear reader, will find them equally compelling.

Figure 5.1 poses the problem we will solve: high-resolution imaging of labelled objects completely hidden behind opaque scattering layers. To achieve that, we will use nonlinear labels, laser scanning, and luminescence detection with a bucket detector.

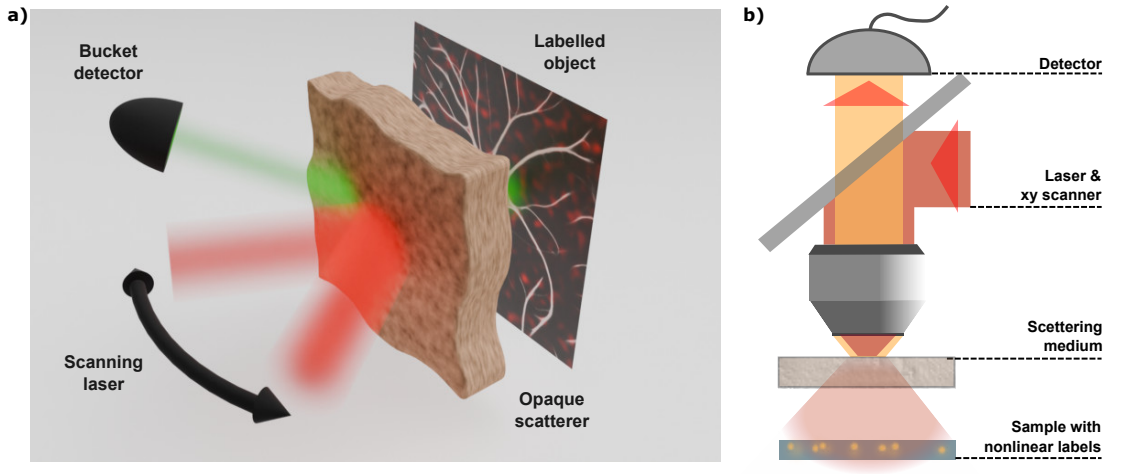

Figure 5.1: Physical principle and experimental implementation of NISE. (a) A laser illuminates the scattering layer under different incidence angles. Behind the opaque scatterer lies the hidden object to be imaged (white). The red granular pattern represents the speckle field exciting the nonlinear luminophores, while the resulting green luminescence is collected with a bucket detector. (b) Experimental realisation of NISE. The excitation laser (red) enters the microscope body, is reflected by a dichroic mirror, and illuminates the scatterer. The speckle pattern generated after propagation through the scatterer excites the nonlinear labels. The laser scanner is arranged such that changing its angle shifts the speckle pattern laterally. For each illumination angle, the emitted luminescence (yellow) is separated from the excitation path and collected by a detector.

I find that the best possible introduction to this chapter is the short summary co-authored by R. Łapkiewicz, P. Wasylczyk, A. Makowski, W. Zwoliński, and me:

"While scattered light conveys most of the information we perceive, scattering may also blur or attenuate that information before it reaches our eyes or detectors. The problem is acute in many applications, such as in high-resolution microscopy of biological tissue, where scattering degrades both resolution and signal-to-noise ratio. We demonstrate that uniting two intrinsic properties of multiply scattered light: speckle formation [27] and the angular memory effect [36] with the extreme nonlinearity of photon-avalanche nanoparticles (ANPs) [130] yields, rather surprisingly, super-resolution, low-background imaging deep inside strongly scattering samples. Because the strategy relies solely on fundamental spatial and statistical properties of speckle fields, and on the high-order nonlinear response of the luminophores, it can be applied to any speckle-forming propagation, from biological tissue to multicore fibres, and to any type of labels that exhibit a sufficiently steep power-law dependence of luminescence intensity on the pump intensity. In our experiments, a standard laser-scanning microscope was adapted for excitation with a continuous-wave 1064 nm laser and detection of the 800 nm up-conversion emission of the ANPs. The ANPs, inorganic nanocrystals doped with lanthanide ions, exhibit a steep nonlinear dependence of the emitted luminescence on the pump intensity [130], ideal for our approach. After traversing a scattering layer placed behind the objective (e.g. a 500 μm brain tissue slice or an optical diffuser not transmitting any ballistic light), the beam reaches the sample, containing nonlinear labels, as a speckle field whose individual grains remain diffraction-limited. Remarkably, as we demonstrate in our work, the random speckle illumination of a highly nonlinear sample results in a single, localised, sub-diffraction excitation spot. Owing to the angular memory effect, small tilts of the incident beam translate the entire speckle pattern laterally without altering its structure, allowing a conventional raster scan deep below the scatterer surface. The integrated signal collected in epi-configuration yields a high-contrast image whose excitation point-spread function is narrowed below the diffraction limit; we achieve a lateral resolution of 560 nm FWHM that is more than 2 times better than 1.2 μm theoretically achievable Abbe limit with our wavelength and microscope objective (see Fig. 5.11). Crucially, our technique: Nonlinear Imaging with Speckle Excitation (NISE), does not resort to wavefront shaping, adaptive optics, complicated optical setups, or iterative image reconstruction algorithms (see Table 5.1 for a comparison with existing frameworks). In terms of performance, NISE offers super-resolution, beyond the reach of current methods: $\sqrt{N}$ resolution enhancement due to the Nth order nonlinearity, as well as immunity to aberrations. The imaging depth, improved by higher-order nonlinear responses, has the potential to exceed that of multiphoton microscopy. The frame rate is limited by the pixel dwell time (1 ms in our setup, due to the nonlinear response buildup time), not by computational or wavefront optimisation overhead. Importantly, our framework may be implemented on a conventional scanning microscope and is readily compatible with other techniques, which opens avenues for hybrid approaches and applications in optical imaging and beyond."

Table 5.1: List of techniques for imaging through scattering media with comparison to our framework.

Existing Method	**How it works**	**In comparison, NISE ...**
Multiphoton Microscopy [25, 26]	Fluorophores are excited with a strong pulsed light, and fluorescence from raster-scanned ballistic focus is collected via a bucket detector.	... does not require ballistic light at all, offering deeper penetration; additionally, it can also work in the regime where multiphoton microscopy operates.
Iterative feedback wavefront-shaping [35, 131]	A Spatial Light Modulator shapes a sharp excitation focus while its quality is being iteratively probed.	... does not require lengthy optimisation nor recalibration.
Transmission Matrix [46, 132]	The Transmission Matrix is measured with controlled input modes, and its inverse is used to acquire the image.	... does not need to retrieve the information about the scatterer, and works without a heavy computational load.
Blind Computational Imaging [133, 134]	Camera frames acquired under random illumination are used to unmix the object from the scatterer computationally.	... does not require large datasets and high algorithmic complexity.
Speckle Correlation [49, 135]	Correlations and randomness of speckle pattern(s) are used to retrieve the image of simple objects using iterative algorithms.	... works independently of the object complexity.
Computational holography, phase conjugation [52, 136]	The electric field of scattered light is measured, and the influence of the scatterer is compensated by wavefront shaping.	... does not require a complicated setup (interferometric stability).
Ultrasound-guided approaches [28, 137]	Ultrasound creates a guide star for adaptive wavefront-shaping.	... delivers optical super-resolution.

This chapter develops a full narrative around NISE – Nonlinear Imaging with Speckle Excitation. I begin by explaining why the central observation is, at first glance, unbelievable, but later trivial: that sufficiently high optical nonlinearity, by itself, can sort of remove the scattering layer as if it was not present in the beam path. I then trace what is exciting about this mechanism, not only the physics that makes it possible, but also the experimental elegance that makes it practical.

The most important results are presented concisely in the manuscript titled "Overcoming Light Scattering with High Nonlinearity" [56]. Rather than duplicating a conventional "Results" section, I weave the key findings into a story that hopefully makes the concept intuitive, complementary to the article, and demonstrates how it works in practice.

5.1 Understanding NISE

Understanding Speckle Excitation

Let us shine a laser through a matte document sleeve (you can try it yourself). The transmitted beam does not produce a smooth blur, but rather a granular intensity pattern known as a speckle pattern. The most straightforward and intuitive way to understand speckles is to think of them as a random interference pattern. Importantly for our analysis, such a pattern is easy to model and to simulate. Let us begin our model and simulation by illuminating a thin scatterer (e.g., with a plane wave or a Gaussian beam). A convenient approximation treats the scatterer as a random phase mask, i.e., it multiplies the incident field by $e^{i\phi(x,y)}$. Such multiplication by the random phase encapsulates the transition of light through a rough surface of the matte sleeves or paper almost directly; importantly, even thin tissue layers behave approximately in this manner. To obtain the field after our scatterer, we must perform appropriate propagation. We restrict ourselves to developed speckles – we observe the scattered light in the far-field of the scatterer. We could use Fraunhöfer propagation, but for simulation simplicity and a qualitative description, we just take a Fourier transform (equivalent to the far-field approximation). Next, squaring the modulus of the resulting field yields a speckle pattern with similar grain intensity statistics to those from the experiments (see Fig. 5.2). Later, when we dig deeper into the underlying maths of the speckle patterns, it will become apparent why the intensity statistics are essential. By intensity statistics, I mean the distribution of the maximum intensity of a distinct speckle grain in the experimental or simulated speckle pattern.

Importantly, the average speckle-grain size is governed by diffraction limit: $\langle s_{\text{grain}} \rangle \sim \lambda/(2\,\text{NA}_{\text{eff}})$, where NA_{eff} is the effective NA determined approximately by the beam size at the scatterer divided by the distance of the observation plane to the scatterer [27]. These speckle sizes are consistent with what I observe experimentally. For an effective numerical aperture of $\text{NA}_{\text{eff}} = 0.45$, the speckle size (approximated by the FWHM) in the experiment is about 1.2 μm – the same as the FWHM of the Airy diffraction spot expected for NA = 0.45 at 1064 nm.

For NISE, these two properties of the speckle pattern matter. First, its scale: grains are roughly diffraction-limited. Second, its statistics: speckles have an ex-

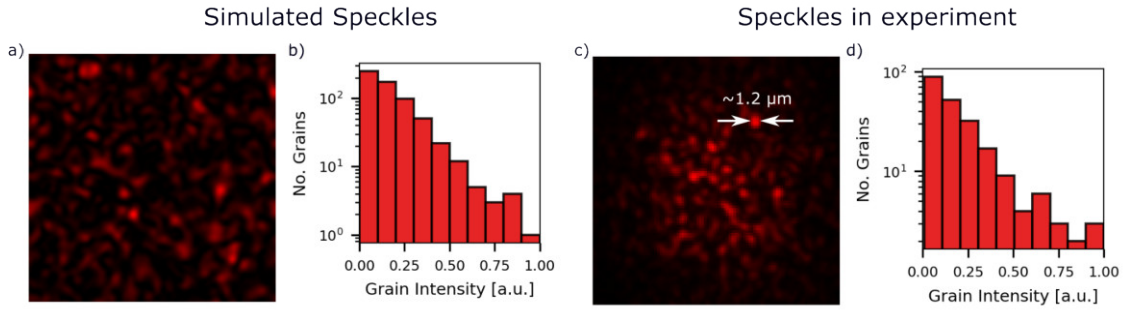

Figure 5.2: Comparison of numerical speckle simulations with the experiment. (a) Simulated speckle pattern. (b) Grain-intensity histogram of the simulated pattern; the grain counts are shown on a logarithmic scale. (c) Speckle pattern observed experimentally. The speckle-grain size is diffraction-limited (for $NA_{eff} = 0.45$ and a 1064 nm wavelength, the expected FWHM is 1.2 μm). (d) Grain-intensity histogram of the experimental pattern; the grain counts are shown on a logarithmic scale.

ponential intensity distribution, with bright grains occurring rarely. With this in mind, we now consider nonlinear excitation by such a speckle field.

For simplicity, let us assume a uniform layer of luminescent material illuminated by the speckle pattern. When the luminescence is local, we can write a general expression for the luminescence:

$$F(x, y) \propto R\{I_{exc}(x, y)\}, \tag{5.1}$$

where $I_{exc}(x, y)$ is the speckle intensity and $R\{\cdot\}$ is the material's response with the proportionality influenced by the density of luminophores. As a thought experiment, let us set $R\{I_{exc}\} \propto I_{exc}^n$ and calculate F for different n's (see Fig. 5.3). In our speckle pattern, we have a lot of speckle grains and, in particular, a single brightest speckle grain with (let us normalise the speckle pattern) intensity $S_1 = 1$a.u. We have a second-brightest speckle with intensity $S_2 = 0.8$, a third with $S_3 = 0.7$, etc. One would immediately see that the higher the nonlinearity order n, the less speckles contribute meaningfully to the signal. Eventually, for $n = 20$, essentially a single, brightest speckle survives while all dimmer grains contribute negligibly to $F(x, y)$: $1^{20} = 1$, while $0.8^{20} = 0.012 \simeq 0.0$. This seemingly simple observation became a key for NISE.

Scan and image formation

For many people unfamiliar with techniques of imaging through scattering media, scanning with a speckle pattern is an unintuitive and unexpected process. We will try to change that feeling. Let us build our intuition on the characteristics of a thin lens, but this time keep in mind that a lens can be treated as a phase object. Tilting or laterally shifting the input beam at a lens translates the focus in the sample. To some extent (within small tilts or shifts), the focus is only translated without changing the focus shape, similarly with the scatterers. When we treat them as a random phase plate, slight shifts or tilts of the beam illuminating the scatterer should translate the speckle pattern behind the scatterer without changing the pattern's shape. This translate-only behaviour is called the optical memory effect [36, 48,

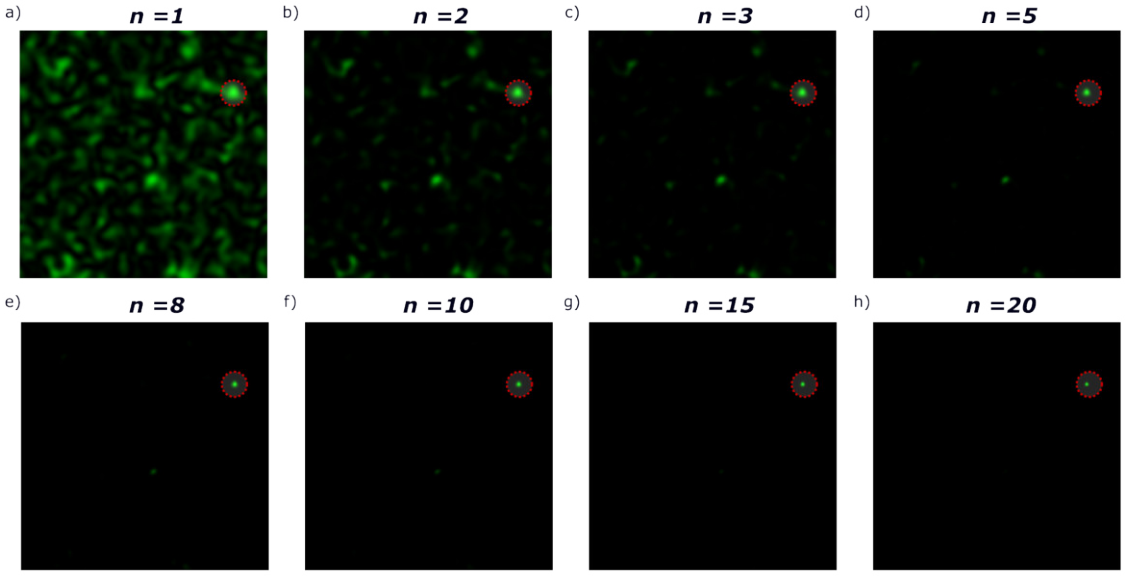

Figure 5.3: Simulated luminescence of a uniform layer of luminophores excited by a speckle field for different nonlinear orders. The emitted signal is proportional to the local excitation intensity raised to the power n: (a) n = 1, (b) n = 2, (c) n = 3, (d) n = 5, (e) n = 8, (f) n = 10, (g) n = 15, and (h) n = 20. For high nonlinear orders, only the brightest speckle contributes significantly to the total luminescence; this dominant speckle is marked with a red circle.

138] and it is the "enabling" phenomenon for most techniques of imaging through scattering media.

In NISE, we place the scatterer in the plane $z = 0$ and observe the intensity at a plane d downstream. Denote by $\Delta\boldsymbol{\theta} = (\theta_x, \theta_y)$ a small tilt of the incident wavefront at the scatterer and by $\Delta\boldsymbol{\rho} = (\Delta x, \Delta y)$ a small lateral displacement of the input beam across the scatterer. In the memory-effect range (small $|\Delta\boldsymbol{\theta}|$ and $|\Delta\boldsymbol{\rho}|$), the speckle pattern translates according to

$$I_{exc}(\mathbf{r};\, \Delta\boldsymbol{\theta}, \Delta\boldsymbol{\rho}) \;\approx\; I_{exc}(\mathbf{r} - \Delta\mathbf{r};\, \mathbf{0}, \mathbf{0})\,, \qquad \Delta\mathbf{r} \;\approx\; \Delta\boldsymbol{\theta}\, d \;+\; \Delta\boldsymbol{\rho}. \tag{5.2}$$

Thus, a small input tilt and translation shift the speckle by $\Delta\boldsymbol{\theta}\, d \;+\; \Delta\boldsymbol{\rho}$ at the observation plane. I am aware that a careful reader may already be irritated by the non-precise formulation of "small" that is used notoriously. Firstly, the small-angle approximation is the paraxial approximation – we say that $tg(\Delta\theta) = sin(\Delta\theta) = \Delta\theta$. For the memory effect, the "small" angles are even smaller, and for the tilt-only memory effect, one can find a relation giving at least some notion of how small it is [30, 36]:

$$\Delta\boldsymbol{\rho}_{\boldsymbol{max}} \simeq \frac{d\lambda}{\pi L}, \tag{5.3}$$

where λ is wavelength, and L is the thickness of the diffuser. Within a FOV restricted by the memory effect, we can proceed with the mathematical formulation of the result of the scan as the convolution of the effective excitation and the density of the labels. Let us illuminate a labelled object with label density $O(x, y)$ (unknown) with speckle field $I_{exc}(x, y)$ (random, and also unknown). The resulting luminescence is just point-wise multiplication of $O(x, y)$ and the local luminescence response of the labels $R\{I_{exc}(x, y)\}$. Unfortunately, we do not have access to such a spatial map

of luminescence because of the diffuser covering the specimen. Nevertheless, we can collect all the light coming from the sample with a bucket detector that is equivalent to:

$$Signal \propto \int_{-\infty}^{+\infty} O(x,y) R\{I_{exc}(x,y)\}\, dxdy. \tag{5.4}$$

We scan and collect the *Signal* for every position of the tilt that results in the image formation:

$$Im(\Delta\theta_x\, d, \Delta\theta_y\, d) \propto \int_{-\infty}^{+\infty} O(x,y) R\{I_{exc}(x-\theta_x d, y-\theta_y d)\}\, dxdy. \tag{5.5}$$

Mathematically the above integral 5.5 is the convolution of the Object with the effective excitation $R\{I_{exc}(x,y)\}$:

$$Im(\Delta\theta_x\, d, \Delta\theta_y\, d) \propto (O * F)(\Delta\theta_x\, d, \Delta\theta_y\, d). \tag{5.6}$$

Here, I explicitly present the luminescence response $F(x,y)$ of the uniform layer, which we based our intuition upon (Eq. 5.1, and Fig. 5.3). We can generate then the images obtained with speckle scanning for different nonlinearity orders (see Figure 5.4) Now we should notice that if the excitation consists of a single bright speckle grain (similarly to single focus), the scan of a highly nonlinear sample with a speckle pattern is equivalent to the scan with a focused beam (see Fig. 5.4 h).

The summary of this introduction is well captured with the manuscript figure 5.5.

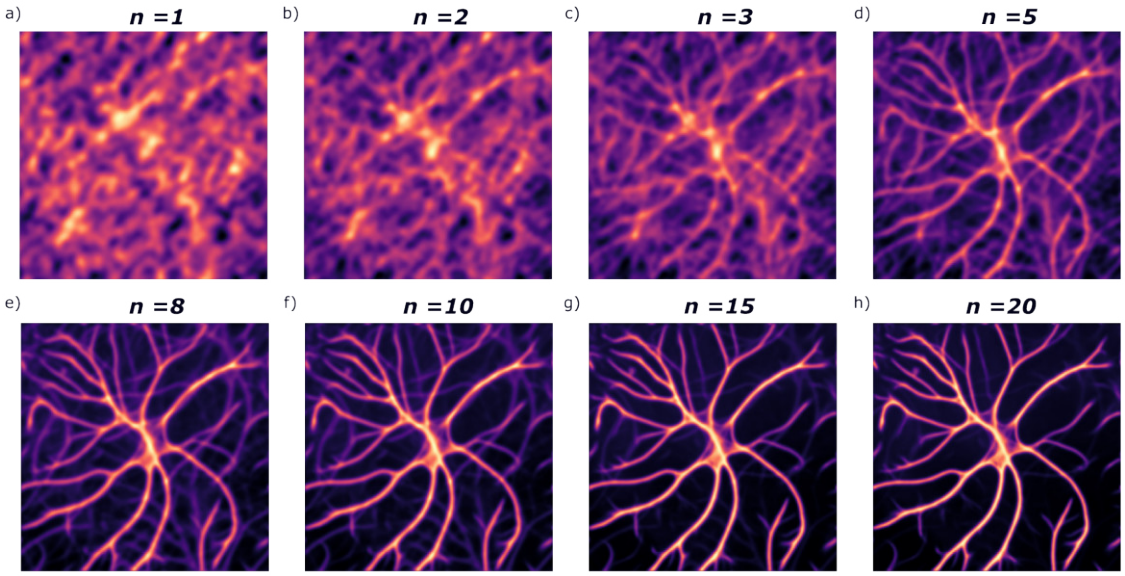

Figure 5.4: Simulated images of an object under different nonlinear responses of the staining agents. The nonlinear order n in the emission process is proportional to the local intensity I raised to the power – I^n : (a) n = 1, (b) n = 2, (c) n = 3, (d) n = 5, (e) n = 8, (f) n = 10, (g) n = 15, and (h) n = 20. Each image is obtained by convolving the nonlinear luminescence pattern from a uniform sample (Fig. 5.3) with an experimental object. The object is an astrocyte imaged with a temporal-focusing microscope operating in single-photon wide-field mode.

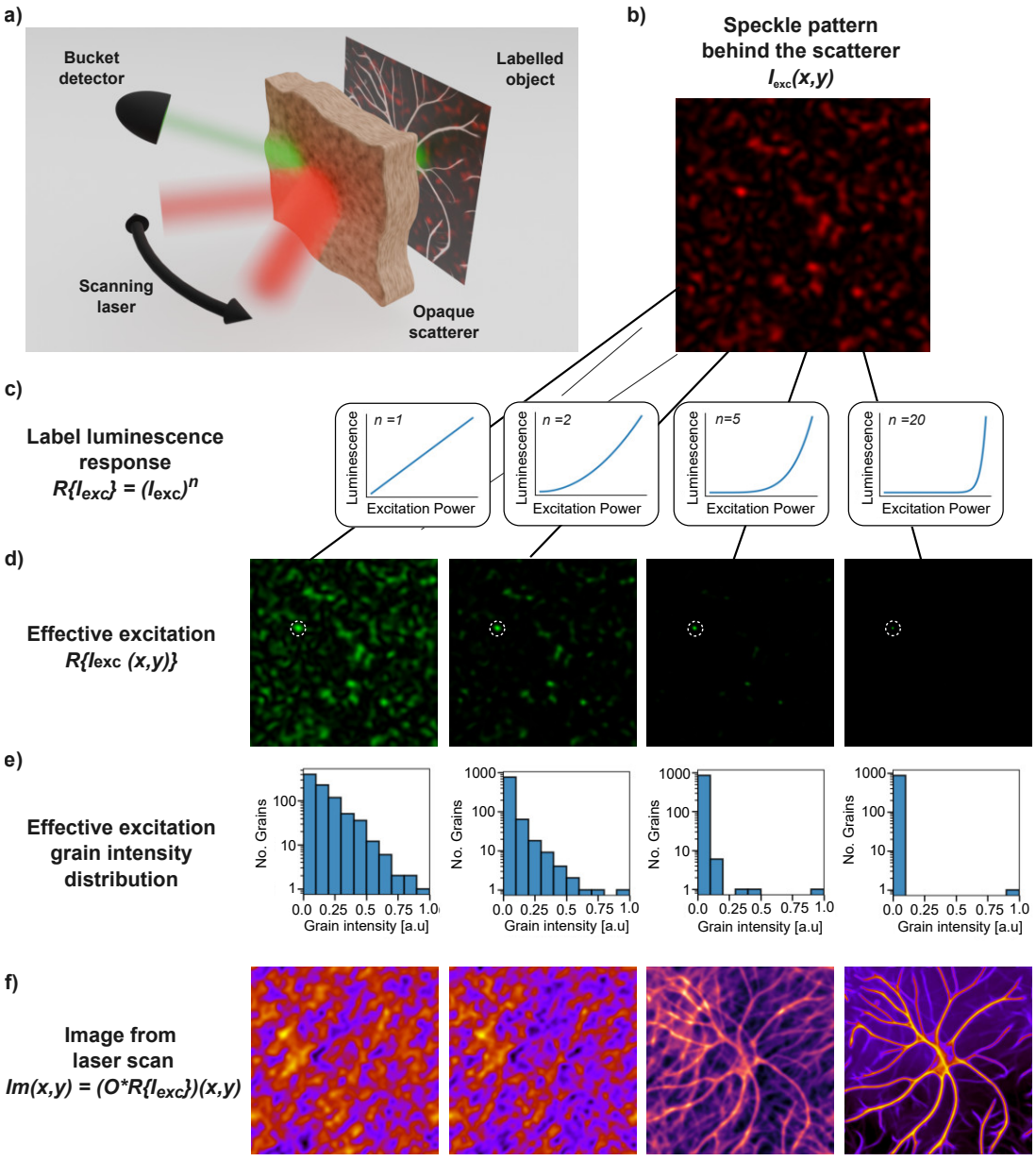

Figure 5.5: Schematics and numerical simulations illustrating the principle of Nonlinear Imaging with Speckle Excitation – NISE. Labelled object O (based on an astrocyte image) is completely hidden behind an opaque scattering layer and is illuminated with a laser light that excites luminescent labels (a). After propagation through the scatterer, the beam reaches the object as speckles (b). The effective excitation pattern depends on the nonlinearity of the label response: $R\{I_{exc}\} = (I_{exc})^n$, where $R\{\cdot\}$ is the luminescence response function, and I_{exc} is the excitation light intensity. For linear response (left column: $n = 1$), the effective excitation is a dense, grainy pattern, while for increasing nonlinearity (middle columns: $n = 2$, $n = 5$), it becomes more sparse, until it consists of a single sub-diffraction excitation spot originating from the brightest speckle (right column: $n = 20$, marked with white circle), while all the others are suppressed (d). The histograms of the effective excitation speckle grain brightness (in normalised arbitrary units) in the log scale (e). Images recorded by raster scanning of the speckle pattern across the object are given by the convolution of the object and the effective excitation: $Im(x, y) = (O * R\{I_{exc}\})(x, y)$, (f). Figure and caption adopted from [56].

5.1.1 Statistical Properties of Speckles

So far, I have kept the mathematics relatively light. In this subsection, however, we must turn the dial a bit up: not because math alone makes an argument better, but because it certifies the core claim behind NISE and shows quantitatively that the probability of the nonlinear effective excitation originating solely from the single, brightest speckle is not negligible. We will then find the probability that the brightest speckle grain is sufficiently brighter than the second brightest speckle grain. A careful but still tractable calculation not only sounds more professional; it gives intuition for why and when NISE works.

What we want to compute (and why)

We will go through the speckle statistics for NISE in the following order:

1. Find the general distribution of intensity in speckle patterns
2. From pixel-wise distribution, transition to the intensities of speckle grains
3. Find the distribution of the brightest speckle grain intensity and the second brightest speckle grain
4. Find the probability that their ratio is below a certain number.

This ratio r is the practical figure of merit. If the material response is a steep power law ${I_{exc}}^n$, then the unwanted signal from the second-brightest grain is r^n. As a reference point, if $n = 15$ and $r = 0.8$, then $r^{15} \approx 0.035$, i.e., about 3.5% unwanted contribution, which we can reasonably treat as noise. Our "toy accuracy model" is therefore: determine $\Pr(r \leq R)$ for a target R (e.g. $R = 0.8$); if this probability is $\gtrsim 0.1$, then NISE's odds of producing clean images are satisfactory.

5.1.2 The Exponential Intensity Distribution

Following Book of Goodman [27], we treat the speckles as general as possible. We assume only that the scatterer can be treated statistically. We return to the picture of speckles as random interference. We look at a single point of the speckle pattern. The field amplitude at this point can be thought of as a sum of many scattered waves (i.e., plane-waves) with some amplitude ε_m and some phase $e^{i\phi_m}$ (acquired upon propagation and by scattering events). We then write the field at a given point as a coherent sum of many (M) phasors:

$$E = \sum_{m=1}^{M} \varepsilon_m \, e^{i\phi_m}, \tag{5.7}$$

with ϕ_m being a random variable effectively uniform on $(-\pi, \pi)$. When we focus only on the real part of E: $\mathcal{R}$, we have the sum of many random variables. For large M, the central limit theorem implies that the distribution of $\mathcal{R}$ is a Gaussian distribution. Importantly, no strong assumption is needed here – it happens for thin or thick diffusers, inside or outside the scattering medium. We now turn to the strong-scattering regime, where no ballistic light is present, and the Gaussian distribution has zero mean. The imaginary part of E: $\mathcal{I}$ has the same distribution with the same variance, and we can write the complex circular Gaussian distribution:

$$p_{\mathcal{R},\mathcal{I}}(\mathcal{R},\mathcal{I})\, d\mathcal{I}\, d\mathcal{I} \; = \frac{1}{2\pi\sigma^2} exp\left(- \frac{\mathcal{R}^2 + \mathcal{I}^2}{2\sigma^2} \right) d\mathcal{I}\, d\mathcal{I} \tag{5.8}$$

with σ being the variance of this distribution. In general, we are interested in the probability for the intensity $I = \mathcal{R}^2 + \mathcal{I}^2$. We proceed to the intensity distribution using the rules of probability theory for transformation of variables [27] that yields the negative exponential probability density function:

$$p_I(I) = \frac{1}{\langle I \rangle} \, \exp\left(-\frac{I}{\langle I \rangle} \right), \qquad I \geq 0. \tag{5.9}$$

Here, we inserted the mean intensity $\langle I \rangle$ as a physical quantity we measure.

Speckle grains intensity distribution

Because the field is smooth, intensities at nearby points are correlated and interdependent. This correlation decays over a characteristic correlation area that sets the speckle grain size. If we tile the observation plane into disjoint "correlation boxes," then intensities across boxes can be treated as independent random variables. In the previous part, we did not specify the position at which we measure the intensity. We now specify this position to be the maximum intensity within a single correlation box. The same arguments as in the previous section are in play, and the maximum intensity of the speckle grain can also be approximated with the negative exponential. Here, it is a good place to highlight that:

1. the negative exponential is only an approximation, as there physically cannot be a speckle grain with infinite intensity, which is not prohibited by the long tail of the negative exponent
2. the correlation boxes are usually derived with some far-field propagation. For some cases (e.g., not fully developed speckles), the correlation areas can be different from the ones described here.
3. The mean value of $p_{\mathcal{R},\mathcal{I}}(\mathcal{R},\mathcal{I})$ is not always zero, i.e., in the case with ballistic light, and then this derivation needs to be modified.

Probability distribution of the brightest speckle grain intensity and the second brightest speckle grain

This consideration follows the reasoning by W. Zwoliński from supplementary material of [56] and from our conversations about NISE: Let us number every independent grain in the speckle pattern from 1 to N, and let $I_1 \geq I_2 \geq \cdots \geq I_N$ denote their ordered intensities (brightest to dimmest).

The probability for such a particular speckle pattern to appear is:

$$p_{I_1,I_2,\ldots,I_N}(I_1, I_2, \ldots, I_N) = p_{I_1}(I_1)p_{I_2}(I_2)\cdots p_{I_n}(I_n). \tag{5.10}$$

We care only about the brightest speckle grain intensity I_1 and the second brightest grain intensity I_2. All the other speckles can have intensities ranging from 0 to I_2. Here, we introduce a useful function of the cumulative probability density function (CDF):

$$F(x) = \int_0^x p_I(I)dI = 1 - \exp(-x/\langle I\rangle). \tag{5.11}$$

For N independent and identically distributed random variables, the joint probability density of the second brightest $I_{(2)}$, and brightest $I_{(1)}$ speckle grains is the standard order-statistics result:

$$p_{I_{(1)},I_{(2)}}(I_1, I_2) \;=\; N(N-1)\,[F(I_2)]^{N-2}\,exp(I_2/\langle I\rangle)\,exp(I_1/\langle I\rangle). \tag{5.12}$$

We integrated the probability for every individual speckle grain, except for the brightest and the second-brightest. The second brightest speckle grain can be in one of N positions, and the brightest speckle grain can occupy the same positions, except the one occupied by the second brightest speckle: $N-1$. This already contains the necessary information.

Ratio of the second to first

We are interested in $\Pr(r \leq R)$, with the ratio $r = I_2/I_1$ and R being some arbitrary threshold. Using the joint probability density (eq. 5.12) and the change of variables $(I_1, I_2) \mapsto (r, I_1)$, we write the expression for the cumulative probability:

$$\Pr(r \leq R) \;=\; \int_{I_1=0}^{\infty}\int_{I_2=0}^{RI_1} N(N-1)\,[F(I_2)]^{N-2} f(I_2)\, f(I_1)\,\mathrm{d}I_2\,\mathrm{d}I_1. \tag{5.13}$$

For compact form and easier integration, we introduced $f(I) = exp(I/\langle I\rangle)$. Noting that $f(I)\,\mathrm{d}I = \mathrm{d}F(I)$ we integrate the inner integral first:

$$\int_{I_2=0}^{RI_1}(N-1)\,[F(I_2)]^{N-2} f(I_2)\;\mathrm{d}I_2 \;=\; [F(RI_1)]^{N-1} - \;[F(0)]^{N-1} = [F(RI_1)]^{N-1}. \tag{5.14}$$

Plugging back the explicit form of F and f, we integrate over I_1. However, for clearer notation, we introduce the variable $y = I_1/\langle I\rangle$ and arrive at a compact closed form:

$$\Pr(r \leq R) \;=\; N\int_0^{\infty}\Big(1 - e^{-Ry}\Big)^{N-1} e^{-y}\,\mathrm{d}y. \tag{5.15}$$

I believe if you are a mathematician, you instantly notice the Beta integral after appropriate substitution $t = e^{-Rx}$:

$$\boxed{\Pr(r \leq R) \;=\; \frac{N}{R}\int_0^1 \Big(1-t\Big)^{N-1} t^{\frac{1}{R}-1}\,\mathrm{d}t \;=\; \frac{N}{R}\,\mathrm{B}\Big(\tfrac{1}{R},\,N\Big),} \tag{5.16}$$

where $\mathrm{B}(\cdot,\cdot)$ is the Beta function, well defined for numerical computations and preferably used by computers. For humans, though, the form with Gamma functions can be more appealing[1]:

$$\boxed{\Pr(r \leq R) \;=\; \frac{\Gamma(1/R+1)\,\Gamma(N+1)}{\Gamma(N+1/R)}, \qquad R>0,\ (\,N>1\,).} \tag{5.17}$$

Equation 5.17 is the cumulative distribution function (CDF) of the ratio $r = I_2/I_1$ for N independent speckle grains. The generality of this derivation, and the compact form of the final equation, can be surprising and thus give some doubts. However, this result entirely agrees, both with our simulations (Fig. 5.6 a) and with the experiment (Fig. 5.6 b). The most significant advantage of such analytical solutions is the predictive power and ease in drawing useful conclusions. E.g., Worth noting is the fact that the probability $\Pr(r \leq R)$ decays slowly with increasing number of speckle grains N. For large N equation 5.17 can be approximated by [139]:

$$\Pr(r \leq R) \;\sim\; \frac{\Gamma(1/R)}{R}\,N^{\,1-1/R}, \tag{5.18}$$

[1]Gamma function becomes incomprehensible for numbers as small as 300. Computation of the expression 5.17 is impossible numerically for large Ns; thus, for any computations, equation 5.16 should be used.

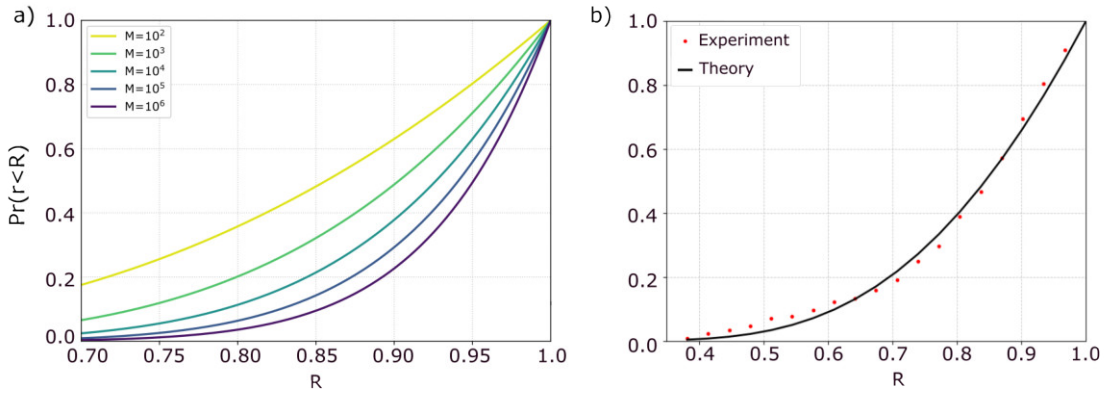

Figure 5.6: Cumulative distribution function for the ratio of the second brightest speckle and the brightest speckle grains. (a) calculated probability density function of ratio r being smaller than some arbitrary value R for different numbers of speckles N: 10^2,10^3,10^4,10^5,10^6. (b) is an experimentally determined cumulative probability function for an optical diffuser (red dots). The diffuser was rotated to get different speckle patterns. The number of different patterns in the experiment exceeds 30. The black solid line represents the theoretical fit of the function from equation 5.16. Single parameter fit for N (number of speckles) resulted in $N \simeq 80$, which is within 10% accuracy for the number of speckles that can be manually counted. Courtesy of Wojciech Zwoliński. Figure adopted from [56] 1st and last versions.

which decays sublinearly in N because $1/R > 1$. Thus, even speckle patterns containing a lot of speckle grains retain a non-negligible chance that the second-brightest speckle grain is substantially dimmer than the brightest one. For a number of speckles not reaching mathematical infinity, we can easily calculate the exact values. E.g., for $R = 0.8$ (so $r^{15} \approx 0.035$ of background), one finds:

$$\Pr(r \leq 0.8) \approx 0.53 \ (N = 20), \qquad 0.36 \ (N = 100), \qquad 0.20 \ (N = 1000).$$

Even with $N = 1000$ speckle grains, about one frame in five already satisfies $r \leq 0.8$, i.e., is effectively single-spot dominated under a 15th-order response. The higher the nonlinearity, the larger the threshold R can be, thus the higher the odds of acquiring a perfect scan.

5.2 NISE Experiment

The NISE instrumentation is, at its core, a scanning microscope. Yet to describe, understand, and systematically test all aspects of NISE, I built a dedicated setup. The goal was to know how every piece of the setup works precisely. The scheme of this setup is shown in Figure 5.7.

Excitation Path

The excitation path in the NISE instrument is more elaborate than in a standard scanning microscope, because it must support two complementary sources and preserve well-controlled pupil conjugation through several relays. I use two 1064 nm lasers: a high-stability 3 W, CW source with TTL gating for fast on–off control (to probe the rise dynamics of avalanching particles, and their luminescence response function $R\{I_{exc}\}$), and a 20 W, CW source for high-flux operation and imaging through scattering layers (In scheme 5.7 LP Laser and HP laser respectively). The 20 W laser is unpolarised, so the beam first passes a polarising beamsplitter (PBS1) to define a linear polarisation, then a half-wave plate and a second PBS for fine power tuning and stable attenuation. The 3W laser is introduced into the same path by removing a mirror from a magnetic mount. The Galilean telescope (T1, lenses: $f = -30$ mm, $f = 100$ mm) expands the beam so that the lasers have similar beam diameters, and the half-waveplate sets the polarisation to avoid attenuation at the first PBS.

After power management, a Galilean telescope (T2, lenses: $f = -100$mm, $f =$ 150mm) expands either of the beams to a few millimetres. This serves two purposes. First, it lowers the irradiance on the scan mirrors below the damage threshold. Second, it lets me match the excitation focus to the detection focal plane by adjusting the position of one of the lenses (introducing non-perfect collimation).

After such preparation, the beam enters the block responsible for scanning. The scanning block is a conjugated two-galvo system (GM_y and GM_x). One galvo mirror is imaged onto the other with a 4f relay so that the pair behaves as a single pivot at a well-defined plane (FP1, FP2). In my implementation, the 4f is built from singlet lenses (L1, L2) with focal lengths of 100 mm. With this configuration, the maximum deflection range that preserves a stationary pupil point, i.e., scan angle without lateral beam walk at the conjugate plane, is within approximately $-0.7°$ to $+0.7°$. In this range, the excitation beam remains effectively stationary at the pivot, and the paraxial approximation holds. Beyond that range, higher-order aberrations in the simple singlet relays begin to matter. An achromatic pair can extend the usable range. An f-theta or a scan lens would further linearise the spot position versus the scan angle. Scanning outside the $\pm 1°$ window is still possible, but then one must characterise the mapping from galvo angle to focal shift and apply a proper correction. Note also that for large scan angles($|\theta| > 0.7°$) the beam's position at the objective's back aperture changes enough that the transmitted power becomes mildly angle-dependent.

For the proof-of-concept demonstrations reported here, singlet-based relays were sufficient and offered the most practical balance of cost, simplicity, and performance.

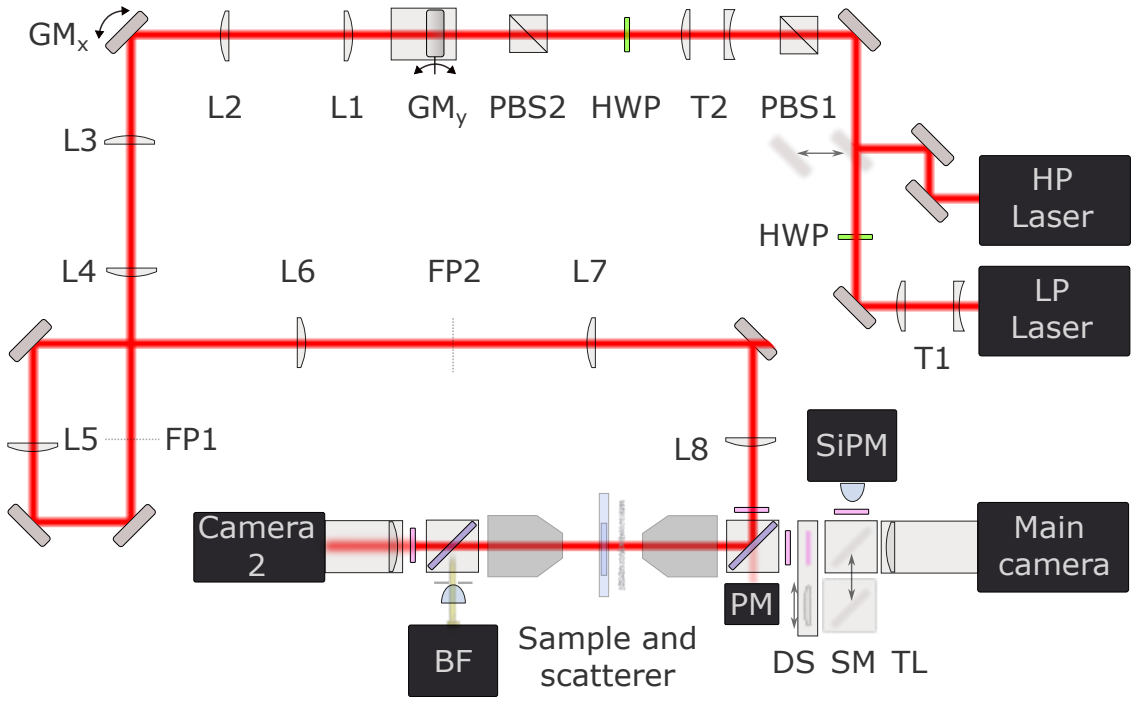

Figure 5.7: Scheme of the experimental setup for NISE. The scheme represents the real placement of the elements on the optical table (up to scaling). Two CW, 1064nm sources – Low power laser (3W) and High Power laser (20W) (LP Laser and HP Laser, respectively) are used for excitation of the nonlinear labels. The LP laser beam expands first through the telescope T1 (focal lengths: -30mm, 100mm), and then the polarisation is set to be horizontal using a half-wave plate (HWP). HP laser output is unpolarised, and after three steering mirrors, the polarisation is set to horizontal with PBS1. The third mirror is placed on the magnetic base, allowing for switching between the sources. After PBS1, the Galilean telescope T2 further expands the beams (focal lengths: -75 mm, 100mm). Afterwards, a half-wavelength plate in a motorised mount and PBS2 enables precise power control. After PBS2, the beam is elevated using a periscope that ends with a galvo mirror (GM$_y$). This mirror scans along the vertical axis. Next, a 4f system consisting of two lenses with 100 mm focal lengths (L1, L2) images the surface of the GM$_y$ onto the second galvo mirror (GM$_x$). GM$_x$ scans along the horizontal axis. After GM$_x$ scanning along the horizontal axis, the beam traverses another 4f system, consisting of lenses with 100 mm focal lengths (L3, L4), creating a galvo-conjugated plane, FP1. This plane is imaged with a 4f system onto FP2. The first lens in this 4f telescope (L5) has a focal length of 200 mm, and the second lens (L6) has a focal length of 150 mm. FP1 and FP2 are optional locations to insert the scatterer, which distorts the beam and introduces speckle excitation. FP2 is imaged onto the back focal plane of the objective with a 4f system with L7 lens ($f_{L7} = 100$mm) and L8 lens ($f_{L8} = 200$mm). After L8, the beam goes through a narrowband filter and reflects from a dichroic mirror to the objective. The leakage through the dichroic mirror is collected with a power meter (PM). After the objective, the diffuser can be placed completely covering the sample with nonlinear labels. After the sample, the excitation is imaged using an additional microscope module, which includes the objective and tube lens (TL2 with a focal length of 100 mm). This imaging process projects the sample plane onto the sensor of Camera2. Before TL2, an absorptive filter reduces the signal, and a dichroic mirror reflects most of the excitation light. This dichroic is also used to introduce the bright-field illumination with an 800 nm LED (BF). The Imaging of the sample can occur in two configurations: WF imaging with the Main camera, or laser scanning with the Silicon Photon Multiplier (SiPM). For WF, an additional spectral filter is inserted in the detection slider (DS), and the 200 mm tube lens creates an image of the sample on the Main camera. For detection with SiPM, a lens with a focal length of 75 mm is placed in DS, and the SiPM Mirror (SM) reflects the light into the SiPM detector. Before the detector, a set of spectral filters is followed by a high-NA aspheric lens.

Downstream of the scanner pair, the beam traverses three additional 4f relays. First relay (L3, L4; $f = 100$mm) followed by two longer 4f telescopes (L5, L6 f_{L5}=200 and f_{L6}=150, and L7, L8 with f_{L7}=100, f_{L8}=200mm) that complete the pupil conjugation to the objective. The second 4f with 100 mm lenses (L3, L4) ensures symmetry of the two scan axes so that GM_y and GM_x see identical optics. The third 4f (L6, L6) translates the conjugate scanner plane forward toward the microscope body; this stage reflects a legacy layout choice but remains convenient for spacing and mechanical access. The fourth 4f (L7, L8) images the scanner pivot precisely onto the objective's back focal plane, ensuring that angular deflection at the mirrors produces a pure field tilt at the pupil and a clean lateral shift of the focus in the sample.

Immediately before the beam enters the light-tight microscope body, I place a narrow notch filter (TECHSPEC 1064 CWL, OD 4.0, 10 nm Bandpass Filter) to suppress any residual wavelengths other than 1064 nm originating from either the laser or the nonlinear interactions with optical elements. This also keeps the detection bands free from the stray light.

Detection

As noted earlier, the objective is the most important element of the microscope, so the detection geometry is built around it. In the NISE setup, the objective threads into a rigid, custom body made of two magnetic cubes and one filter slide.

Inside the first cube (Thorlabs: DFM1/M), we place a short-pass dichroic with a 900 nm cut-off (Thorlabs: DMS900R) as the main separator, directing the excitation light to the objective. The first magnetic cube holds the objective horizontally, which makes it both stable and convenient for alignment with standard Thorlabs elements. In the next port (opposite to the excitation port) the residual leakage through the dichroic mirror is collected with a power meter[2] (Thorlabs PM16-121). The next port (opposite to the objective) is tightly connected with the filter slider (Thorlabs: CFS1).

The filter slider provides additional spectral selections for alternative emission bands that different types of labels may produce. Additionally, I put a focusing lens ($f = 75$mm) there to increase the amount of light directed to the detector (especially in highly scattering scenarios). Tightly connected to this filter slider is the second magnetic cube (Thorlabs: DFM1/M), which enables quick and repeatable reconfiguration between detection branches: either the camera or the Silicon Photon Multiplier (SiPM). The mirror inserted inside this cube redirects the sample luminescence onto the SiPM path (non-descanned point detection). A blank 3D-printed insert allows the light to pass through the cube to the wide-field camera path.

The SiPM path begins with a flat mirror seated in a snug 3D-printed holder (Thorlabs part DFM1T4 could be used). An additional stack of short-pass and notch filters is placed in front of the SiPM, removing any remaining 1064 nm leakage before the detector (in total, in the SiPM detection path, there are four filters: 2X FESH0900, and 2XNF1064-44). Next, a lens ($f = 25.4$ mm) focuses the lumi-

[2]This leakage was also used in some experiment for inspection of the speckle patterns created upstream the objective. Then the leakage light was imaged onto a camera with an additional lens, and the power was measured with an additional pickup in between the cube and the lens.

nescence onto the SiPM sensor. While imaging with SiPM, I insert the additional lens into the lens slider, which slightly increases the signal amount.

The camera branch is intentionally simple: a 200 mm tube lens (Thorlabs TTL-200A) forms the image on a Hamamatsu ORCA-Quest sCMOS. This path provides ultra-low-noise wide-field readout for alignment, bright-field preview, and additional experiments with focused excitation and wide-field detection. Although the camera is fully capable of detecting the weak ANP emission and operates in similar timescales as the avalanching particles, in practice, I relied on the SiPM for fast scanning measurements and used ORCA-Quest primarily for bright-field preview with large FOV, navigation around the sample, and finding a focus.

Bright-Field

To introduce bright-field illumination, I use an 800 nm LED (BF) in a Köhler-like configuration. For that, I use an additional microscope module that also functions as an additional inspection device (more about this module in section 5.2.2). The LED active area is imaged onto the back focal plane of the objective with a 30 mm lens. Right after the lens, an aperture is placed to restrict the illuminated area. The BF module is mounted on a rail and can freely move along the optical axis. The objective, acting here like a condenser lens, is mounted on an x-y translation mount (Thorlabs: CXY1A).

5.2.1 The Sample – Avalanching Particles

NISE requires an emitter whose signal grows steeply with excitation intensity – ideally, a material in which a small increase in pump intensity produces a disproportionately large rise in luminescence. The response could be in the form of $R\{I_{exc} = I_{exc}^n\}$, but not necessarily. The Rectified Linear Unit (ReLU), used nowadays in artificial neural networks, would work as well. The only prerequisite for NISE is that labels emit substantially more light above a certain threshold. Photon-avalanching particles provide exactly this behaviour. Recent work demonstrated room-temperature photon avalanching in single, Tm^{3+}-doped upconverting nanocrystals [130], with clear power nonlinear thresholds, and emission that can scale with roughly the 20th–26th power of the pump intensity [140] – precisely the kind of nonlinearity our method demands. The underlying physics is a positive-feedback loop driven by excited-state absorption (ESA) and cross-relaxation. The active luminescence centres are lanthanide ions, and in the Tm^{3+} systems of interest, our 1064 nm pump is resonant with ESA, but off-resonant with the ground state absorption (GSA). The rare events of GSA seed the avalanche. The excited ion instantly promotes to a higher state with absorption ESA of 1064 nm. From there, cross-relaxation between neighbouring Tm^{3+} ions splits one high-energy excitation into two lower-energy excitations; subsequent ESA promotes both back up, and the cycle repeats, doubling the number of excited ions each "round". The resulting chain reaction creates the photon avalanche (PA). The emitted luminescence from Tm^{3+} ions has a central wavelength of 800 nm.

For our experiments we used materials prepared by Prof. Artur Bednarkiewicz's team (with particles synthesised by Katarzyna Prorok), including both avalanching

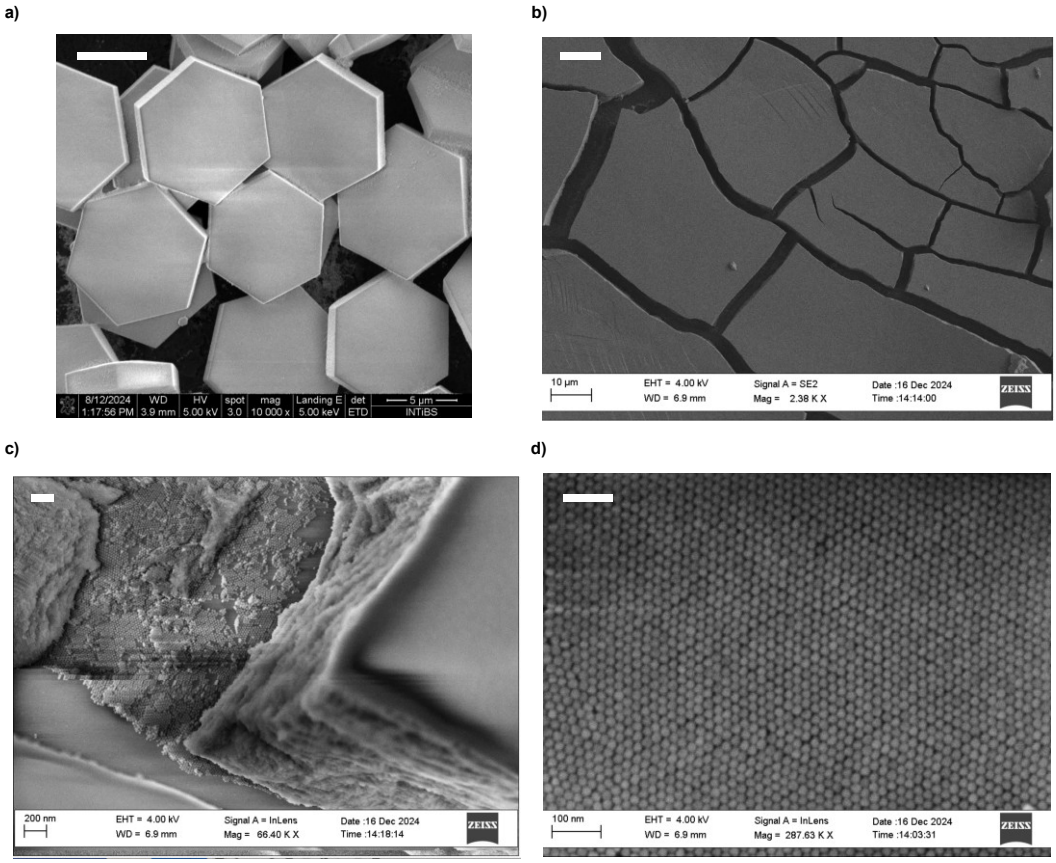

Figure 5.8: Scanning electron microscope images of the avalanching particles. (a) Avalanching microcrystals (Image credit: O.Bezkrovnyi). (b) Irregular layer of ANPs. (c) The close-up photo of the domain edge of the ANPs sample. (d) The flakes/domain regular surface. Scale bars: (a) 5 μm, (b) 10 μm, (c) 200 nm, (d) 100 nm. ANPs SEM images credit: T. Stefaniuk. Adpoted from [56]

nanoparticles (ANPs) and avalanching microcrystals (see SEM images in Fig. (SEM image in Fig. 5.8). The microscope slides were prepared by drop-casting the solution of the particles onto cleaned coverslips. I spin-coated a diluted suspension of microcrystals to obtain a sparse distribution of microcrystals. For ANPs, I allowed the droplet to dry. ANPs created regular structures with cracks (Fig. 5.8 b,c,d).

Even though the nanocrystal prepared in Wrocław had precisely the same chemical composition as the one from the publication claiming nonlinearity of 26 [130], only one sample of nanocrystals consistently delivered sufficient signal and steepness desired for NISE. The avalanching microcrystals, by contrast, were more promising, but still in our scans we observed effective nonlinearities on the order of $\sim$10 (highest slope on a log–log emission vs. power plot).

I characterised each specimen by measuring the dependence of integrated luminescence on incident power – at multiple positions on a given sample. The position dependence was systematic: edges and corners consistently showed lower avalanche thresholds than broad, flat facets (Figs. 5.9, 5.10). A likely cause is an enhanced coupling efficiency of excitation into the structure due to some photonic effects being now under investigation.

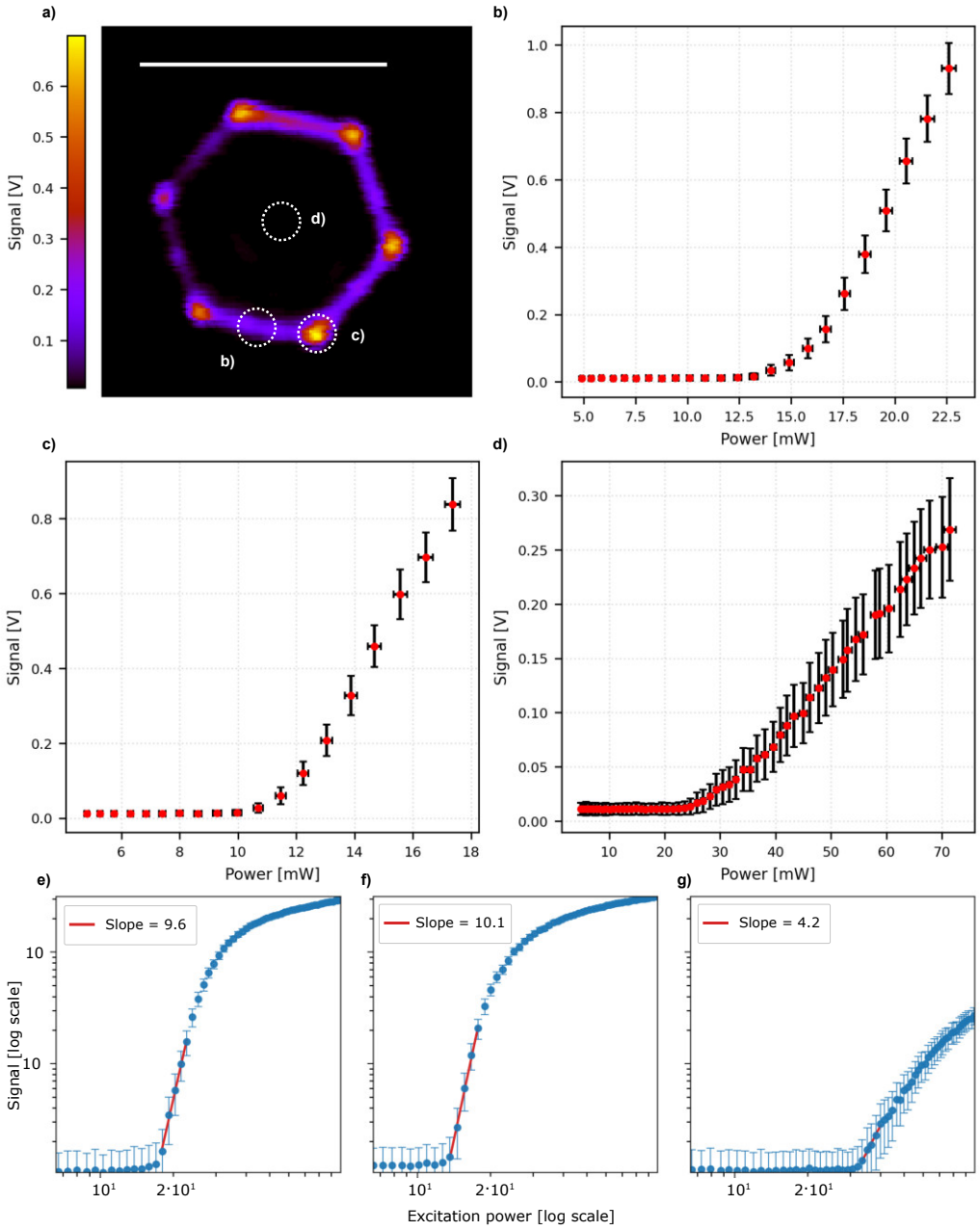

Figure 5.9: Luminescence response of avalanching microcrystals depending on the excitation position. (a) Scanning-microscope image indicating the locations where the luminescence was recorded (edge, corner, and face of the microcrystal). Scale bar: 10 μm. (b–d) Measured luminescence responses at the edge, the hexagon corner, and the face (centre) of the microcrystal, respectively. In panels (b–d), the y-axis shows the SiPM voltage signal, and the x-axis indicates the excitation power measured after a 20×, NA = 0.5 objective. (e–g) Corresponding data from panels (b–d) plotted on log–log axes. At high excitation powers, the response flattens due to detector saturation. The red line shows the fitted power-law dependence, yielding nonlinearities of $n = 9.6$ (edge), $n = 10.1$ (corner), and $n = 4.2$ (face), with a fitting uncertainty of 0.1. Panels (a–d) adapted from [56].

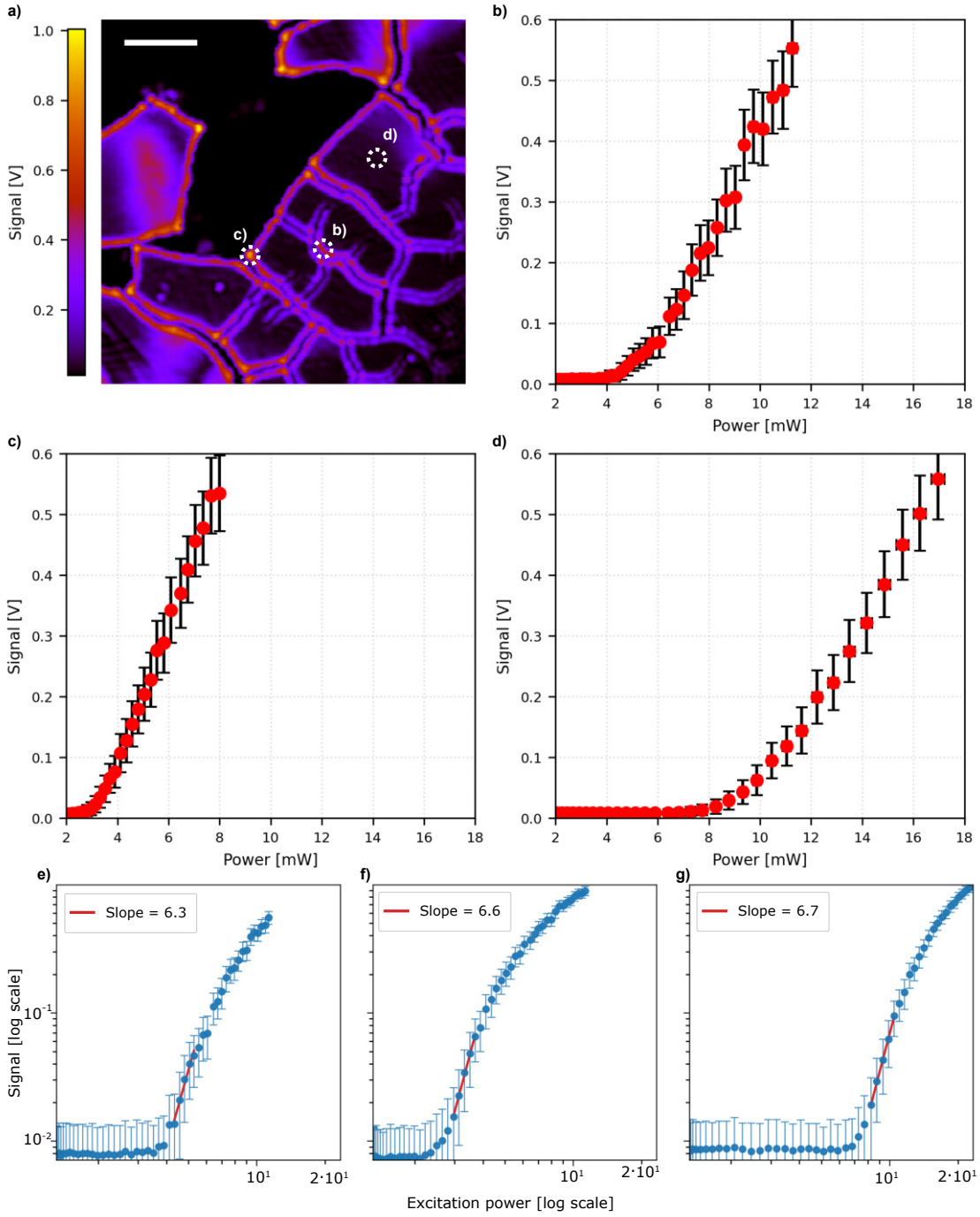

Figure 5.10: Luminescence response of an ANP layer depending on the excitation position. (a) Scanning-microscope image indicating the locations where the luminescence response was recorded (edge, corner, and face of the quasicrystalline domains). Scale bar: 10 µm. (b–d) Measured luminescence signals at the edge, corner, and face of the flake, respectively. The y-axis shows the SiPM voltage signal, and the x-axis denotes the excitation power measured after a 20x, NA = 0.5 objective. All plots share the same x-axis range for direct comparison. (e–g) Corresponding data collected in (b–d) positions plotted on log–log axes. At high excitation powers, the response flattens due to detector saturation. The red line indicates the fitted power-law dependence, with the extracted nonlinearities $n = 6.3$(edge),$n = 6.6$ (corner), and $n = 6.7$ (face); the fitting uncertainty is 0.1. Panels (a–d) adapted from [56].

5.2.2 Examination of the speckle pattern

Another important part of NISE is the speckles. To obtain speckles I used 0.5° holographic diffuser (Edmund Stock #47-988). The light after this diffuser contains less than 1% of ballistic light, and transmits more than 80% of the beam, and is spread over a relatively small area, being ideal for my experiments. During the first experiments, I put the diffuser in the Fourier plane of the objective (FP1 or FP2). In this way, in the focus of the objective, the developed speckle pattern was created. Meanwhile, using the leakage through the dichroic mirror (DM) I imaged the speckle pattern with additional camera (using 400 mm lens). While put in the Fourier plane, I was able to put the diffuser in the rotating mount so that it changed its position, giving room for statistical measurements.

In the final experiment, I put the diffuser behind the objective. I examined the speckle pattern with the additional microscope module. The module is placed on the rail and can slide freely with a precise marginal position toward the sample, regulated by the end micrometre screw. The objective with NA higher than the NA of the objective used for excitation collects the excitation light. Then, most of it is reflected by a dichroic mirror to reduce the amount of light that may go back to the sample. The leakage through the dichroic is attenuated with an additional absorptive filter (Thorlabs NENIR10A). Conversely, this filter can be exchanged with a short-pass filter, enabling the inspection of weak luminescence from the sample. The Excitation light is imaged onto a camera sensor (Bassler daA3840-45um) by a 100 mm achromatic lens. Even though the lens and the objective constitute a 4f system, the image of the speckle pattern is only a preview. The sample itself changes the excitation pattern, as the excitation light scatters on the avalanching particles. Moreover, the speckle pattern changes as the inspection module is translated along the optical axis. The precise plane in which the avalanching particles are excited can not be easily and reliably determined. Although I have full diagnostics of the speckle pattern, I cannot claim which particular speckle pattern excited the avalanching particles, except for the measurement with ballistic light and imaging through a slice of a tissue. There, I could reliably find the right focus of the inspection module based on the ballistic spot size. In the examined range, the intensity in this ballistic spot is the highest; thus, the ballistic light is responsible for the excitation of ANPs. In this case, I also removed the sample from the beam path to mitigate the sample scattering.

5.3 Super-resolution

Even though the acronym NISE does not include super-resolution, it is the intrinsic ability of this method. The speckle grains are diffraction-limited, and nonlinearity narrows the effective excitation below the diffraction limit (See supplementary information of [56]). Here, one additional comment needs to be made. It is the average size of the speckle grain, not the size of every speckle grain, that is diffraction-limited. To obtain super-resolution, one needs to have a good brightest speckle. Surprisingly, in our simulations and experiments, the brightest speckles we encountered were usually close to the diffraction limit and relatively symmetric, so I took it for granted without further formal derivation. Nevertheless, with the nonlinearities of the avalanching samples I used, the super-resolution was not so evident and quite challenging to obtain. With the microcrystals, the avalanche threshold for the vertices is lower than that of the edges. In many cases, when the brightest speckle reached the threshold for the edges, the second brightest speckle was intense enough to excite the vertices, spoiling the image quality. To obtain the result with super-resolution (Fig. 5.11), I moved the scatterer close to the sample to limit the number of speckles illuminating the sample (according to eq. 5.17, fewer speckles give a higher probability of smaller ratios). Then, I used a motorised Z-stage to move the sample along the optical axis to probe different speckle patterns automatically (the speckle pattern changes along the propagation axis). I also performed scans with different excitaion intensities. With a good candidate (no twin images within a reasonable range of powers), I manually tuned the power to be optimal. This experiment took around 6 hours.

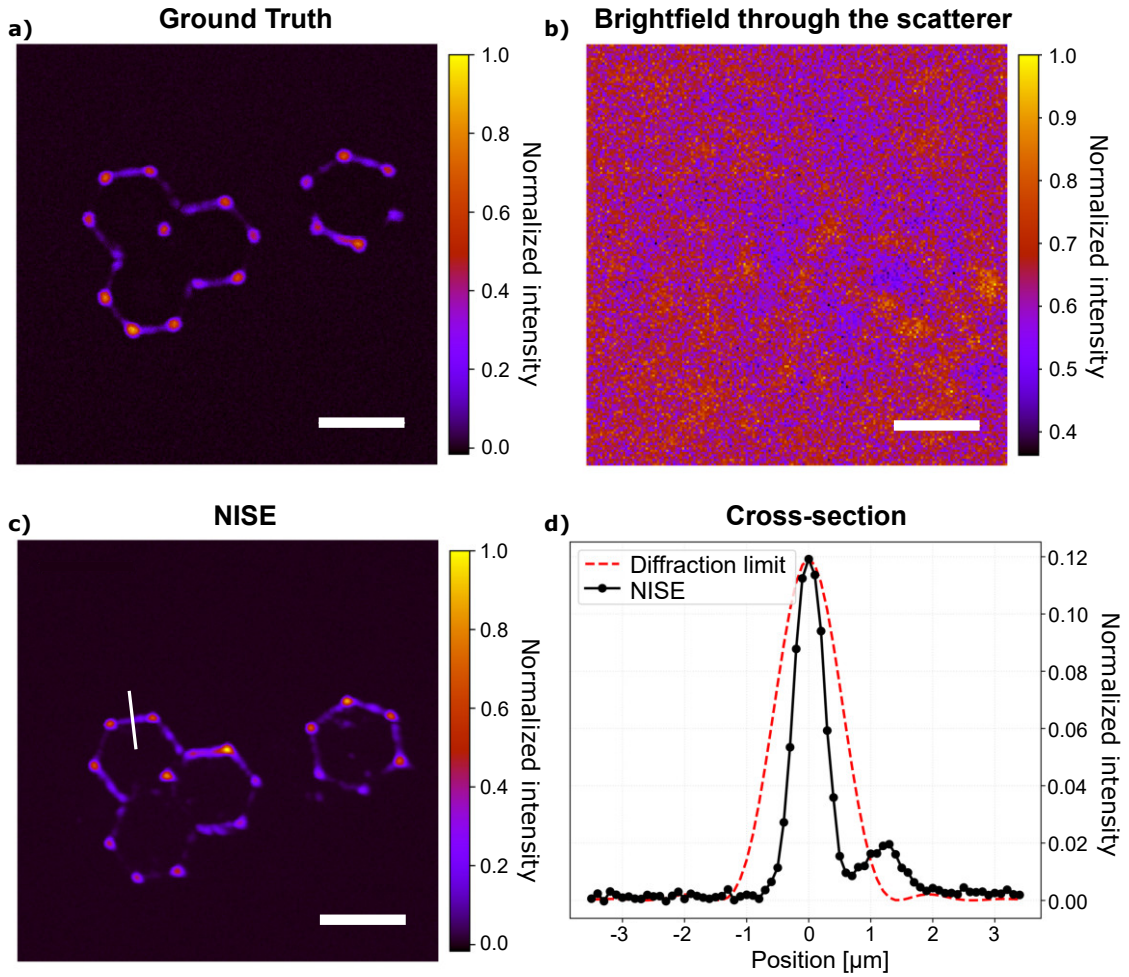

Figure 5.11: Non-invasive super-resolution imaging through an opaque scattering layer. (a) Ground truth image – laser scanning microscope image of the avalanching microcrystals recorded without the scatterer in the beam path.(b) Bright-field image of the sample recorded through a scatterer. (c) Laser-scanning microscope image of the sample recorded through the same scatterer – NISE. (d) Cross-section of the edge of the microcrystal marked with the white line on (c), compared with the theoretical point spread function for the objective with NA=0.45 and 1064 nm wavelength. The theoretical FWHM is around 1.2 μm, while the FWHM of the imaged edge of the microcrystal is around 560 nm (estimated from a Gaussian fit). Scale bars in (a)-(c): 10 μm.

5.4 Problems and Limitations

5.4.1 Twin Images

In the idealised model where the local response is a pure power law, $\mathrm{R}(I) = I^n$, it is only intensity ratio that matters. In such a model, changing the excitation power – multiplying all intensities by a constant factor rescales the bucket signal but leaves the image unchanged.

With ANPs, however, NISE works because the luminescence excited by speckle grains with intensities below the threshold is negligible compared to the luminescence originating from the brightest speckle above the threshold. Such nonlinearity has direct consequences for power tuning. Too low power (sub-threshold), results in lack of signal. As the average power increases and the brightest speckle crosses the threshold, object features begin to appear, starting where the threshold is lowest (e.g., at crystal corners). When the brightest speckle sits in the steepest part of the S-shape and most other grains remain below threshold, the image quality is the best (super-resolution). An excitation intensity that is too high is causing saturation. As power increases further, more grains cross the threshold and contribute more to image creation. The final result of the scan image becomes spoiled by "twin images" (displaced duplicates originating from different speckles). Described behaviour is shown in Figure 5.12. A similar twin image would also form with the simple power dependence of the luminescence ($\mathrm{R}(I) = I^n$) when the brightest speckle is not distinct enough from the second brightest speckle. This is one of the problems with NISE – the speckle pattern that is capable of taking a truthful scan occurs often, but not always. Scanning with a non-optimal speckle pattern introduces twin images. Usually a few scans with different speckle patterns (obtained e.g., by illuminating a different position of the diffuser) need to be performed. To know, which scan corresponds to the true, single-speckle-excited image, we would need to introduce some metric that discriminates scans with twin images. In principle, it should be possible to base such metric on autocorrelations of the scans, as the autocorrelation of the object with itself is maximum at point 0,0. With twin images, an additional local autocorrelation maxima would be present in positions when image created by the brightest speckle coincides with the image created with other speckles. Yet, such metric needs to be carefully developed, to be reliable for any object being imaged.

On the other hand, instead of looking for a good speckle pattern, a scan with twin images could be used to computationally retrieve the ground truth image. This could be achieved e.g., via iterative deconvolution or similarly as in [49, 50]. This idea, however, will need to be further studied extensively.

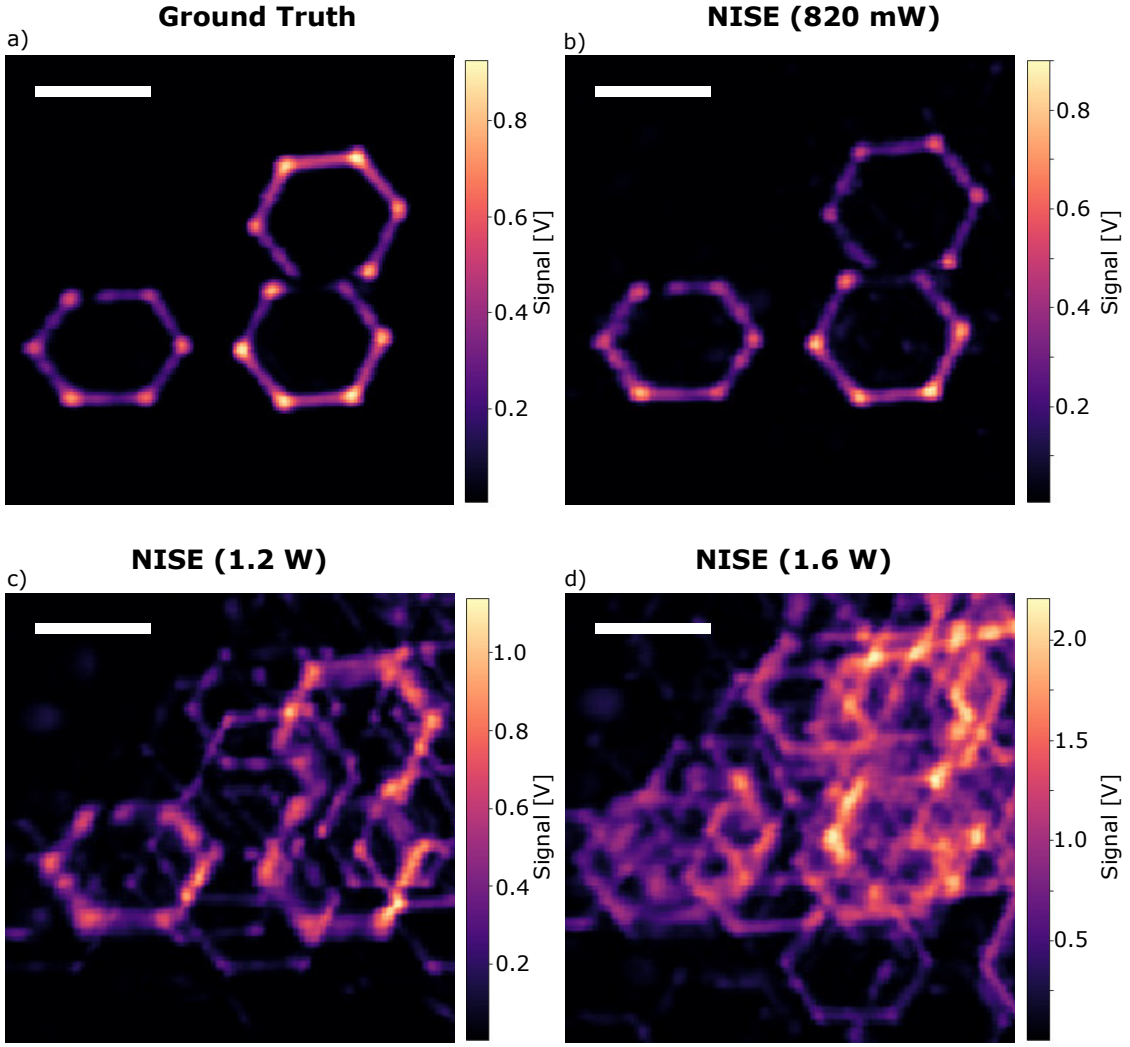

Figure 5.12: NISE with avalanching microcrystals for different excitation powers. (a) The ground-truth image of microcrystals obtained by laser scanning through a 20X objective (NA=0.45) with around 20 mW at the sample. (b) is the result of NISE with a 0.5° holographic diffuser placed between the sample and the objective. With excitation power of ∼820 mW, the image is an unspoiled image of three microcrystals, with similar quality as the ground truth. As the power increase (1.2 W in c) there start to appear twin images originating from less brighter speckles. Additionally, the most intense image of the three microcrystals loses resolution due to saturation. With power increased to 1.6 W the image is contains many twin images making imaging ineffective. Scalebars: 10 μm. The colour corresponds to the voltage measured from the SiPM.

5.4.2 Thick Scatterers

Until now, NISE has been developed and validated with thin scattering layers. The natural next step, and the "holy grail of imaging", is to transit from layers to volumetric scatterers, such as brain tissue, and to image through or within thick scattering media.

This, however, finds no ease in NISE. The difficulty lies in scanning and sectioning. The memory effect shrinks rapidly with thickness and drops roughly exponentially with depth. The speckle pattern is volumetric, and the excitation in 3D would not be confined to a single speckle grain (especially since the mean intensity of the speckle pattern must drop with depth). We are then left with two options: either we solve both issues, or switch to scanning with whatever ballistic component remains, which is not constrained by the memory effect and that is confined in 3D as well. When I attempted imaging through thicker tissue slices ($\sim$700 μm), the power required to excite the ANPs caused tissue damage. This was expected, as the excitation intensity at the ballistic focus decays exponentially with depth, and compensating for this loss inevitably demands an increase in excitation power.

One could instead turn to speckle excitation to try to reach greater depths. Indeed, as shown in the supplementary information of [56], the intensity of the brightest speckle grain decreases with depth z much more slowly than the instensity of the ballistic focus. In particular,

$$\mathbb{E}[I_{\max}(z)] \;\propto\; \frac{\ln(A\,z)}{z} \qquad (z \to \infty), \tag{5.19}$$

where $\mathbb{E}[I_{\max}]$ denotes the expected intensity of the brightest speckle grain, and A is a medium-dependent constant encapsulating its scattering properties and characteristic speckle grain size.

Although this scaling is favorable for maintaining sufficiently high local intensity at depth, for speckle excitation the excitation light is spread over a much larger area than a ballistic focus. As a consequence, the total laser power required to drive the nanoparticles above the avalanching threshold remains high, regardless of the imaging depth.

Given that the nanoparticles used here exhibit avalanching thresholds on the order of hundreds of kW·cm^{-2}, deep biological imaging is ultimately constrained by the risk of photodamage associated with such high excitation intensities. Recent developments in avalanching nanoparticles, however, indicate that lowering these thresholds is feasible [141]. If a luminescent label existed that combined an equally high nonlinear response with a significantly lower excitation threshold, then deep bio-imaging with NISE would become fully practical.

Imaging beyond the memory effect

Two main arguments are in play while turning to imaging with speckle excitation: (i) the resolution is maintained throughout the propagation in the scattering medium, (ii) the intensity of the brightest speckle scales more favorably than the intensity of the ballistic light. The problem we encounter in NISE (and in general, in many methods of imaging through scattering media) is a small memory effect at

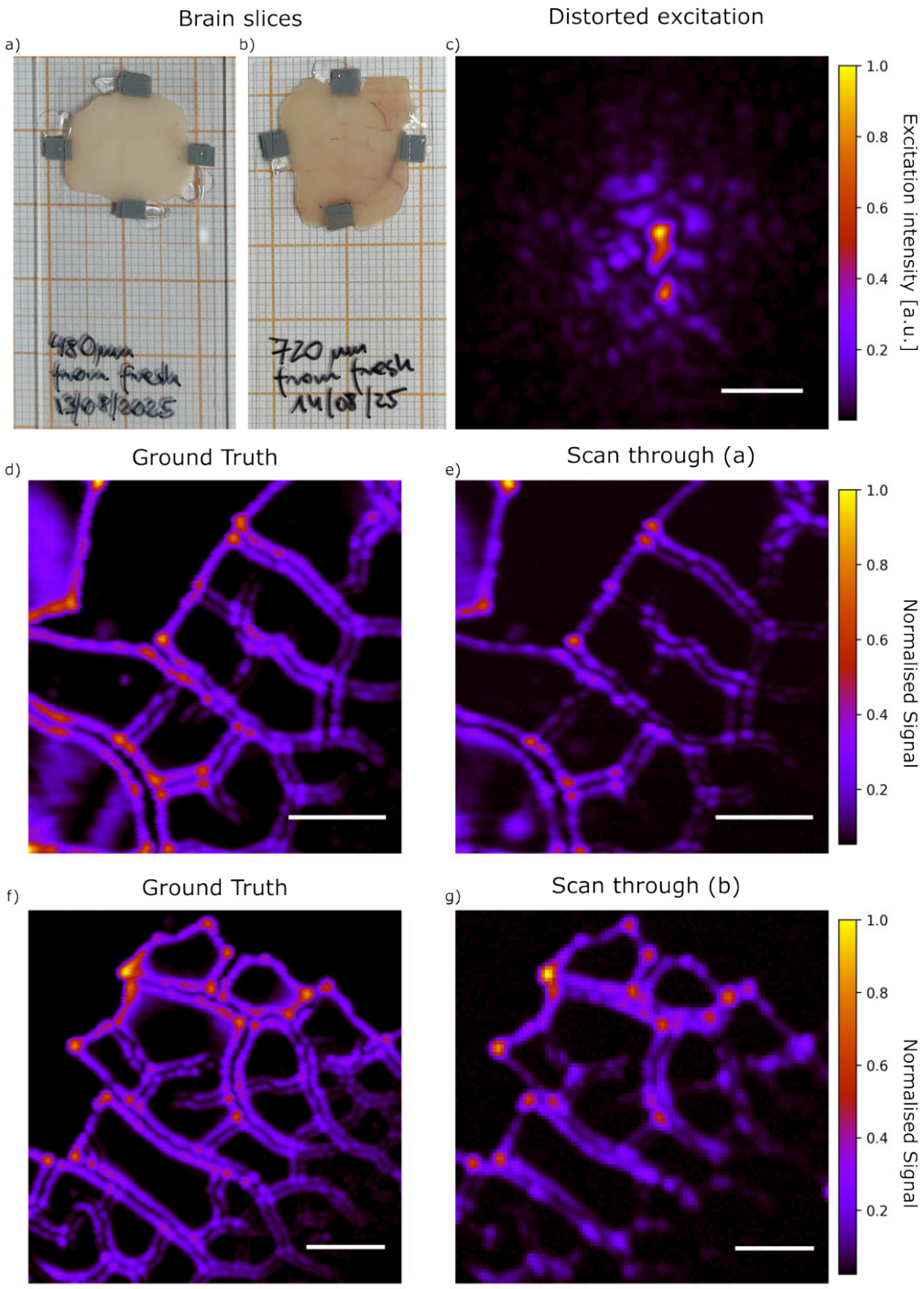

Figure 5.13: Nonlinear imaging through brain tissue. (a) and (b) Photographs of 480 μm and 720 μm-thick calf brain slices, respectively. The tissue was prepared by P. Wasylczyk. (c) Inspection-microscope image of the highly distorted ballistic component recorded through 480 μm of brain tissue. The speckled background arises from the strong scattering of a fraction of the incident beam due to tissue inhomogeneity. (d) and (f) Ground-truth laser-scanning microscope images of the sample acquired without the tissue. (e) and (g) Images acquired through 480 μm and 720 μm of tissue, respectively. The tissue slices were positioned close to the objective (approximately 2 mm from the ANP sample) to minimise the risk of local overheating. The excitation power behind the objective was approximately 0.5 W for (e) and 0.8 W for (g). For imaging through the thickest scatterer (g), the pixel size was increased to $\sim$ 500 nm to have optimal pixel sampling. A scan with a smaller pixel size ($\sim$ 200 nm) suffered from higher detector noise, yet had comparable image resolution to the scan with a larger pixel size. This suggested oversampling at pixel sizes of 200 nm. Scale bars in (c)–(g): 10 μm. Partially adapted from [56].

large depths. For NISE, however, it is not a fundamental limitation. Imaging beyond the memory effect can proceed by patch-wise scanning and stitching. The statistical properties of speckle remain the same regardless of the memory effect. When the speckle pattern is shifted beyond the memory effect, a new brightest speckle grain is most likely to emerge. With this new brightest speckle grain, one could scan within its own memory effect, effectively increasing the field of view (similar to image patching in [142]).

Introducing sectioning

Although speckles are also axially confined, and 3D imaging should be possible, one further limitation for deep NISE is the need for axial sectioning. Deeper planes will typically deliver slightly lower brightest-grain intensities than shallower planes, so an unsectionned acquisition integrates contributions from multiple depths. One idea that crossed my mind was that one could deconvolve deeper scans using a measured axial response to suppress contamination from upper layers. Such deconvolution, however, would introduce an additional lengthy procedure, and I find this solution unsatisfactory. More work is needed in this direction. For example, if co-excitation with an additional laser pulse can trigger the avalanche, one could trigger avalanches in the plane of interest with temporal focusing. Such a solution, however, is application-specific and would work for ANPs; the general solution, does not seem obvious.

Chapter 6

Concussions and Outlook

6.1 Summary

I hope that throughout this thesis, I was able to convey the message of how extraordinary and important application-wise the nonlinearity can be. First, I presented the two-photon microscope that just works. It is fast, stable, and built to work in real-life conditions. Resonant scanning, dual detection, and an open design constitute a flexible platform for custom experiments. We used it to read out neuronal activity in the amygdala and to test ideas like Bessel excitation and two-photon ISM.

Second, I presented yet another clever use of nonlinearity – temporal focusing and I merged it with SOFI for 3D super-resolution imaging. Plane-selective wide-field excitation gives sectioning where wide-field normally fails. SOFI then uses fluorescence fluctuations to obtain resolution beyond the diffraction limit in every dimension. The combination suppresses out-of-focus excitation at the source, localises bleaching to the plane of interest, and unlocks robust 3D imaging with tabletop hardware.

Third, I present the headline result – NISE: Nonlinear Imaging with Speckle Excitation. While turning to sufficiently high nonlinearity, the random speckle pattern converts to an effective excitation, being a single, sub-diffraction spot. Scanning with the pattern enables the acquisition of a super-resolved image of the sample stained with the nonlinear labels. I built a custom microscope to prove the concept. Such an open, fully in-house-built platform enabled additional measurements and full characterisation of NISE, leaving room for further experiments in this regard. I imaged the avalanching particles through the scatterer as if there was no scatterer at all. Compared to other techniques, NISE does not require expensive hardware or highly demanding computations – only the source of a high nonlinearity. Additionally, it is not fundamentally limited by the memory effect that most of the methods in the field use. NISE introduces a novel, unexpected path to overcome scattering – the main challenge in contemporary imaging.

6.2 Nonlinearity for Contemporary Microscopy

This thesis shows that nonlinearity enables a broad range of useful phenomena in optical microscopy, and that the benefits grow as the effective nonlinearity increases.

Important notes about the nonlinearity are as follows. Nonlinearity raises spatial resolution beyond the Abbe limit by making the effective excitation narrower than the linear point-spread function. A nonlinear excitation can provide optical sectioning – a key for deep and volumetric imaging. A small unwanted signal from scattering is strongly suppressed by the nonlinearity, and, for the nonlinearity high enough, the contrast is enhanced even in the worst scenario of no ballistic light. I therefore risk a statement: when truly optical-resolution (below 1μm) images at depths beyond ~ 1.5 mm become available, they will rely on nonlinear effects.

Multiphoton microscopy already illustrates this trajectory. It has transformed in-vivo biophotonics, and the continuing maturation of robust, stable, and increasingly affordable fiber lasers will only broaden its access. Around this core modality, derivative approaches emerge naturally. Beam shaping methods can increase the throughput (e.g. Bessel-beam excitation) or increase the attainable depth (e.g. wavefront-shaping). Pulse shaping, on the other hand, also poses a promising direction (e.g. TF providing selective excitation and reduced bleaching).

Beyond these "regular" nonlinearities lies a new regime opened by photon avalanching nanoparticles. Their local luminescence response to excitation intensity, and, in some cases, extreme nonlinearity, changes the rules. I showed that such giant nonlinearities enable high-contrast imaging through scattering media and super-resolution. As with two-photon excitation, these labels can be just used for techniques developed for single-photon imaging. However, their most interesting potential lies in enabling genuinely new modalities. NISE is one such example, and hopefully, we will soon see more of these.

6.3 Outlook

What has always fascinated me about science is that solving one concrete problem usually reveals a dozen more worth chasing. My PhD felt exactly like that: every setup I built and every measurement I made opened new possibilities and posed new questions seeking answers. Below, I sketch where I would take each platform or technique next and where its problems lie.

6.3.1 TPSM Setup

The main problem of my TPSM implementation is the weak fluorescence signal at 30 FPS. Increasing the excitation power partially compensates for the low signal but simultaneously accelerates fluorophore bleaching, which often renders long-term imaging impractical. Enhancing the signal level without increasing photodamage and pushing the platform's performance toward its optimal operating regime will therefore be the natural next steps. Such improvements would significantly improve usability and overall imaging robustness for end users.

Adaptive optics in the beam path

Placing an SLM or a deformable mirror in the conjugate pupil plane is relatively easy in my open setup. With sensorless metrics (brightness [37], or sharpness [143]), adaptive optics could keep near-diffraction-limited resolution deeper in tissue by correcting specimen-induced aberrations [74], or the aberrations introduced by a GRIN lens [144]. This would yield a better signal-to-noise ratio and presumably lower laser power needed for excitation. With lower power, experiments can take longer and yield more reliable data on neural activity.[1]

Fluorescence Lifetime imaging

The integrated SPAD23 in my setup makes FLIM easily accessible [145, 146]. Although FLIM acquisition would require temporal averaging to collect a sufficient number of photons, it would further expand the platform's versatility, e.g., to image thin brain slices ex vivo. Importantly, providing FLIM and TPSM capabilities within a single instrument lowers the practical entry barrier for new users and simplifies routine operation, which is often desirable in multi-user laboratory environments.

6.3.2 TF Setup

The TF microscope works well, providing sectioned wide-field excitation, yet still with a relatively small field of view. Despite that, the TF+SOFI platform or even TF alone has one particular concern – it is a platform without a specific task or application. Any collaboration to use this setup not only for proof-of-principle studies but also for everyday experiments would greatly reward the time I spent designing and building it.

In the proof-of-principle regime, however, the two directions look immediately promising.

Sectioned wide-field FLIM

A SPAD 512×512 camera synchronised to the laser repetition rate could deliver plane-selective lifetime maps at video-like speeds. This is a natural pairing: TF confines excitation axially, thus reducing bleaching in out-of-focus planes. The SPAD array is capable of reconstructing fluorescence decays pixel by pixel [147]. This combination could pave the way for fast 3D functional FLIM with extended measurement duration due to reduced out-of-focus bleaching.

Functional micromachining in bulk glass

In some applications, such as femtosecond micromachining of glass, nonlinear propagation can lead to self-focusing, limiting the ability to write well-defined patterns in the material. Temporally elongating the pulse outside the focal region can, in principle, suppress these unwanted nonlinearities and improve machining precision [148].

[1] For such experiments, the conjugated galvo system might be better. Redesigning the setup to a galvo-conjugated system constitutes the project of its own.

The TF configuration in my setup could serve as a small-scale testbed for such an approach. Using a high-magnification, high-NA objective as the focusing element would mimic the machining geometry while replacing the low-NA optics typically employed in industrial systems. If the initial experiments showed promising results or revealed the need for further parameter optimisation, the insights gained would be directly transferable to larger-scale laser-machining setups. This pathway could therefore bridge proof-of-concept demonstrations with practical industrial implementation.

6.3.3 NISE

Here, the discussion of the NISE results is in place. The main selling points of NISE are: enabling deep imaging, breaking the depth-resolution limit, and being usable in real-world scenarios, e.g., brain imaging in vivo. It may sound as if NISE is not fulfilling any of these goals. NISE presented in this work provides super-resolution imaging through scattering layers, not deep imaging. The obtained 560 nm resolution is also achievable in TPSM. And the test objects – nanoparticles and microcrystals – may seem disconnected from biological relevance.

This impression changes once the results are placed in the proper context. Imaging through scattering layers is not equivalent to deep imaging. Still, it is a decisive step for any method that aims to operate beyond the depth at which ballistic light vanishes. In this work, I present precisely this: no ballistic component is present in the experiments with a holographic diffuser, yet super-resolution images can still be obtained. NISE operates entirely on the multiply scattered excitation field, therefore making a key conceptual step toward an accurate deep-imaging modality. Worth noting is that, when we turn to ballistic light, maximal imaging depth with ANPs is comparable to that of two-photon imaging (I already presented imaging through 720 μm of brain tissue).

The next aspect is resolution. In NISE, resolution is dictated solely by the speckle size and nonlinearity of the luminophore. The result of 560 nm resolution is limited by the moderate nonlinearity of the avalanching microcrystals. However, nonlinearities of 15–25 are routinely reported in the literature [130, 149–151]. For the nonlinearity of 25, the resolution of NISE in my experiment would be around $1.2\,\mu\text{m}/\sqrt{25} = 240\,\text{nm}$. Using a water-immersion objective with NA$\simeq$ 1, typical for state-of-the-art two-photon high-resolution deep imaging, increases the expected resolution to $\sim$120 nm. At this scale – dendritic spines, critical for understanding learning and synaptic plasticity – become clearly resolvable.

To image dendritic spines inside the brain, one needs to be able to stain them. I could not stain dendritic structures with my nanoparticles, but similar particles are already used in biological contexts. Avalanching nanoparticles have been demonstrated as functional biological labels for super-resolution imaging [152]. Upconverting nanoparticles with a comparable chemical composition are biocompatible and are employed in optogenetics [153, 154]. More importantly, NISE does not rely on avalanching nanoparticles specifically. Any luminophore with sufficiently high nonlinearity is suitable. I expect that such new nonlinear labels will emerge.

Finally, there is one very important aspect of NISE: its experimental implemen-

tation is remarkably simple. The core of the experiment is the scanning microscope – equipment already present in most neurobiology laboratories. If only a compact add-on module and an adjusted staining protocol are required to improve the microscope substantially, then NISE could be deployed broadly without building a dedicated instrument. This ease of adoption is a major advantage and positions NISE as a technique with real translational potential for biological imaging.

For that to happen, a lot needs to be done. Here I will sketch the problems and possible solutions together with other ideas.

Imaging beyond the memory-effect limit (computation)

When we scan beyond the memory range, the brightest speckle grain often dims. However, at the same time, another speckle grain becomes the brightest. A practical path forward is to segment data into tiles and stitch them appropriately. If more than one speckle contributes to the image, iterative deconvolution could recover both the object and the excitation positions. Such a computational approach is beneficial as it does not increase the experimental complexity.

Using special pulsed excitation for lower mean power

Replacing CW with appropriately shaped pulse trains could drive the photon avalanche while reducing the average power critical for the living tissue experiments.

Causing a lower avalanching threshold

Two complementary strategies appear particularly promising for reducing the excitation power required. (i) New emitters with avalanche-like S-curves and significantly lower thresholds [141]. (ii) Co-excitation schemes, similar to those used in upconversion processes [155], that assist the critical transition and shift operation into safer power regimes.

One attractive direction is to investigate whether seeding the avalanche with an auxiliary pulse – tuned to the ground-state absorption – could initiate the transition and reduce the required peak intensity. If such triggering were possible, it would fundamentally relax the power constraints.

Bringing the excitation into biologically safe regimes is essential for any realistic in-vivo imaging application.

Multicolour excitation for sectioning

As NISE gets the excitation sparsity from the nonlinearity, one can think of another scheme that achieves that. Based on the finding of enhanced emission in upconverting nanoparticles [155], that excitation with two wavelengths yields a higher signal than excitation with these wavelengths alone, one could appropriately shine two lasers through a scatterer. Only where the speckle grains coincide, the excitation would be effective, which could make the pattern more sparse. Additionally, for thin scatterers, the speckle patterns for two different wavelengths are not independent

(there exists a spectral memory effect [156]). It may be that the nonlinearity provided by such multicolour excitation will be sufficient to create a single spot or open a new imaging approach using sparse speckle subsets.

More importantly, though, the co-excitation scheme could be used to provide sectioning. The sparsity would also increase in the volume, thus leaving a single speckle in the whole volume for sectioned imaging.

*** Other ideas ***

Fiber endoscopy

Multicore fiber bundles act like thin scatterers, and one can image through them as well [157]. NISE should also work at the distal tip of a fiber bundle. A minimally invasive probe could image at unprecedented depths, with optical super-resolution, using only bucket detection.

Connecting with Wavefront-shaping

ANP nonlinearity is an excellent feedback signal for iterative phase optimisation. Even modest pre-correction that concentrates light into the brightest speckle reduces the required excitation power. Additionally, this could be used for deep imaging, as then the single speckle could be made the brightest in the whole volume, enabling volumetric imaging with limited wave-front shaping.

Using avalanching crystals as guide stars

With the speckle excitation confined to a single point, we already have a good guide-star – a single, subdiffraction spot emitting strong luminescence hidden behind the scatterer. Measuring this luminescence spatially, we know the Point Spread Function of our system (scatterer). Knowing the PSF, we can deconvolve even complex objects.

***

I think that the greatest part of this thesis is that I am leaving more exciting projects than I began with.

6.4 Closing Remarks

The three projects I pursued: TPSM, TF+SOFI, and NISE, taught me a lot. They pushed me to grow as an experimentalist and to learn by doing, including learning by making mistakes. That route works, but it is slow. In my case, the balance tipped too far toward figuring things out alone – whether by temperament or by simple lack of prior knowledge.

This thesis is meant to bend that learning curve for you, dear Reader. I wrote this thesis so that you do not have to reinvent wheels, re-debug the same alignments, or repeat my failures. I tried to show not only what worked, but also what did not, and why. The precise experimental descriptions, alignment routines, and measurement recipes are there so you can get to the edge of human knowledge faster.

Nonlinear microscopy still hides many promising ideas. It rewards curiosity and quick iteration – simple implementations. My hope is that, after reading, you will have more ideas than before, and even more importantly, that you will know how to try them out. If this document helps you in any way in your research (as new ideas, a simple manual, or an introduction to the domain), then it has done its job.

Dziękuję za uwagę i powodzenia.
(Thank you for your attention, and good luck!)

Chapter 7

Appendix - Instructions

And on the seventh chapter Reviewer ended His work which He had done, and He rested on the seventh chapter from all His work which He had done.

7.1 The Rayleigh Criterion

Here, we will precisely derive the Rayleigh criterion for distinguishing two incoherent emitters – perfectly suited for fluorescence microscopy. We use wave propagation and imaging with a 4f system. We model one emitter as a monochromatic point source whose field in the object plane can be represented as a delta distribution. We translate this field to the Fourier space of the first lens with focal length of f_0. Using the Fresnel diffraction integrals with the lens phase factor, the field in f-f configuration is transformed as [57]:

$$E_{\mathcal{F}}\left(\vec{\rho}_{\mathcal{F}}\right) \;=\; -\,i\frac{k}{2\pi f_0}\,e^{i2kf_0}\int_{\mathbb{R}^2}\mathrm{d}^2\vec{\rho}_0\;e^{-\,i\frac{k}{f_0}\,\vec{\rho}_{\mathcal{F}}\cdot\vec{\rho}_0}\;E_0\left(\vec{\rho}_0\right). \tag{7.1}$$

where:

- $k = 2\pi/\lambda$ is the wave number associated with wavelength λ,
- $\vec{\rho_0}$ and $\vec{\rho_{\mathcal{F}}}$ are transverse coordinates in the input and Fourier planes, respectively,
- $E_0(\vec{\rho_0})$ and $E_{\mathcal{F}}(\vec{\rho}_{\mathcal{F}})$ are the complex amplitudes of the electric field in the object plane and in Fourier plane, respectively.
- he highlighted in red $\frac{k}{f_0}\,\vec{\rho}_{\mathcal{F}}$ is the argument of the Fourier transform that is effectively performed by the lens.

Then, the field in the Fourier plane is cut (multiplied) with a circular pupil:

$$\mathrm{P}(\vec{\rho_{\mathcal{F}}}) = \begin{cases} 1, & \text{if } \; |\vec{\rho_{\mathcal{F}}}| \leq a, \\ 0, & \text{otherwise}, \end{cases} \tag{7.2}$$

where a is connected to the numerical aperture of the first lens (or more precisely to the maximal acceptance angle α_{max}). From the geometrical considerations, we have that the size of the pupil $a = f_0\tan(\alpha_{max}) \simeq f_0\sin(\alpha_{max})$ [158]. The multiplication of the field in the Fourier plane by the pupil function is followed by yet another Fourier transform "performed" by the second lens. As the multiplication in the Fourier space

is the convolution in the real space, the result can be written in the convolution form [57]:

$$E_1(\vec{\rho_1}) = \frac{1}{M}\, e^{i\,2k(f_0+f_1)} \int d^2\vec{\rho_0} H\left(\frac{1}{M}\vec{\rho_1} - \vec{\rho_0}\right) E_0(\vec{\rho_0}), \tag{7.3}$$

where:

- M is the magnification of the $4f$ system defined as $-\frac{f_1}{f_0}$, with f_0 and f_1 being the focal lengths of the two lenses,
- $\vec{\rho_0}$ and $\vec{\rho_1}$ are transverse coordinates in the object and image planes, respectively,
- $E_0(\vec{\rho_0})$ and $E_1(\vec{\rho_1})$ are the complex amplitude of the electric field in the object plane and in image plane, respectively.
- $H(\cdot)$ is the amplitude point spread function, that is the scaled version of the Fourier transform of $\mathrm{P}(\cdot)$ from equation 7.2:

$$H\left(\vec{\rho}\right) = \left(\frac{k}{2\pi f_0}\right)^2 \int \mathrm{d}^2\vec{\rho_{\mathcal{F}}} e^{i\frac{k}{f_0}\vec{\rho_0}\cdot\vec{\rho_{\mathcal{F}}}} \mathrm{P}\left(\vec{\rho_{\mathcal{F}}}\right) \tag{7.4}$$

H is acting as a blurring factor and the electric field amplitude image of a single point through the $4f$ system is just proportional to $H(\frac{1}{M}\vec{\rho_1})$. For circular aperture from equation 7.2 it renders as jinc function that is proportional to the Bessel of the first kind divided by its argument:

$$H(\vec{\rho_0}) = \left(\frac{k}{2\pi f_0}\right)^2 \int_{|\vec{\rho}_{\mathcal{F}}|\leq a} \mathrm{d}^2\vec{\rho}_{\mathcal{F}}\ \ e^{\,i\frac{k}{f_0}\vec{\rho}_0\,\cdot\,\vec{\rho}_{\mathcal{F}}} \;=\; \left(\frac{k}{2\pi f_0}\right) \frac{a}{r}\, J_1\!\left(\frac{k}{f_0}\, a\, r\right), \tag{7.5}$$

where $r = |\vec{\rho_0}|$ is the distance from the origin. We can easily recognize the NA of the first lens – $\frac{k}{f_0}a = \frac{2\pi\, n}{\lambda}\sin(\alpha_{max}) = 2\pi\frac{NA}{\lambda}$ and connect it to the maximal resolution. Let us now determine a criterion for the two emitters being distinguishable. The Rayleigh criterion is:

"The two points in the image plane are considered resolvable if the centre of the one point coincides with the first zero of the jinc function."

The first zero of the jinc function $J_1(x)/x$ is around 3.83. Let us approximate it by π for easier calculations. Substituting the condition for the approximated root we arrive to the Abbe expression:

$$|\vec{\rho_{max}}| = 3.83 \cdot \frac{\lambda}{2\pi NA} \simeq \frac{0.61 \cdot \lambda}{NA} \tag{7.6}$$

We should already recognise that we base our result on the measurement of the electric field that we almost never measure. For the intensity measurement I, we just take the square of the expression 7.5 to obtain the Point-Spread-Function (PSF). Return to the main thread 2.1

7.2 Two-photon Microscope Manual

1. **Switch on the chiller:** set the temperature to 19.9 °C.
2. **Switch on the NI acquisition box.**
3. **Switch on the computer.**[1]
4. **Switch on the Sutter stage controller:** click the green *"Move"* button to enable the stage.
5. **Switch on the galvo power supply.**
6. **Open the *Halite920* laser control software:**
   (a) Ensure that the chiller has reached the set temperature.
   (b) Wear protective goggles and remove all jewelry, watches, or reflective objects from your hands.
   (c) If prompted, turn the key on the back of the laser.[2]
   (d) In the software, click and hold the green *"On"* button to power on the laser.
   (e) Set the laser power using the power slider. The typical imaging power is *XX* mW (adjust as required for the sample).
7. **Open *Matlab*.**[3]
   (a) In the command line, type `scanimage` and press Enter.
   (b) In the pop-up window, verify that the default Machine Data File path is: `C:\Users\lbijoch\Videos\Dokumenty\2photon_2022_11_14_newNI.m`
   (c) Press *"Start ScanImage"* and wait for the initialization to complete.
8. **Open the Basler Video Recording software (wide-field preview):**
   (a) Move the black slider to the right (towards the microscope tower) to set detection to wide-field mode.
   (b) Switch on the excitation LED using the control knob.
   (c) Using one-photon fluorescence preview, find the focus and region of interest (ROI) by moving the stage along x, y, and z axes.
   (d) (Optional) Use a phone flashlight for coarse focusing if fluorescence is not visible.
9. **Open *PMT2010*:**
   (a) Select the default serial number.
   (b) Ensure the room lights are off.
   (c) Enable the PMT by moving the main gain slider above zero (this activates the detector).
10. **Switch to two-photon detection:**
    (a) Turn off the wide-field LED.
    (b) Pull the black slider to the left to insert the mirror and redirect the signal to the PMT.
11. **Open the physical laser shutter:** lift the lever upwards (toward the left) to open the beam path.
12. **Start imaging in *ScanImage*:**
    (a) Press *"Focus"* or *"Grab"* to begin image acquisition.

[1] Always power on the NI box first. Otherwise, the computer may not detect the NI device.
[2] The key switch is located on the rear panel of the Halite laser.
[3] A connection (Ethernet) to the Institute network is required for the Matlab license.

Auxiliary Devices

1. **Switch on the power supply for the IR LED.**
2. **Open *Pylon Viewer*:** Select the camera *AC2000-165umNIR*. Ensure that the **Trigger Mode** is enabled, then start acquisition.
3. **Open Arduino sketches:** `acquisition_synchronization_v2.ino` and `pump_and_LED_sending2.ino`.
4. **Set the correct boards:**
   - For the synchronization sketch – select **Teensy 3.5**.
   - For the sending sketch – select **Arduino Micro**.
5. **Upload the sketches:** Connect the devices and upload each sketch to the corresponding board, selecting the appropriate COM ports in the Arduino IDE.
6. **Open *CoolTerm*:** Use this software to record the serial port output and export it as a `.csv` file for later analysis.
7. **Run the synchronization check:** During a TPSM scan, the IR-viewing Basler camera should start recording automatically. Simultaneously, the serial monitor (Teensy output) should display the current TPSM and Basler frame numbers, as well as encoder step counts.
8. **Activate pumps manually (optional):** In the serial monitor terminal for the Arduino Micro, type one of the following commands:
   - `w` – activate the water pump,
   - `s` – activate the sucrose pump,
   - `q` – activate the quinine pump.

7.2.1 Synchronization of the Basler Camera and TPSM

Precise synchronization between the Basler camera and the TPSM is achieved using a Teensy microcontroller board. The Teensy receives a TTL trigger signal from the TPSM frame trigger output, provided by the ScanImage software through the NIDAQ.

Upon detection of the rising edge of this TTL pulse, an interrupt routine is executed on the *Teensy*. This routine immediately generates a corresponding rising-edge synchronization signal to trigger the Basler camera and simultaneously records the arrival time of the incoming TTL pulse for further time management. The delay between the input and output pulses is approximately 10 ns, which is negligible for live-imaging applications operating on millisecond timescales.

Each time the TPSM trigger is detected, the internal counters `twoPh_frames` and `Basframes` are incremented by 1. To support high-speed acquisition (up to 120 FPS), the Teensy can also generate an additional trigger pulses for the Basler camera, incrementing the `Basframes` counter once more.

In addition to synchronization, the Teensy monitors an optical encoder using hardware interrupts. Forward and backward rotations of the encoder are recorded and stored in memory. Three additional digital inputs are dedicated to monitoring the operation of liquid pumps. When a pump is active, its corresponding input pin goes high, and the event is logged. The signal state identifies which pump was operating at the moment of triggering:

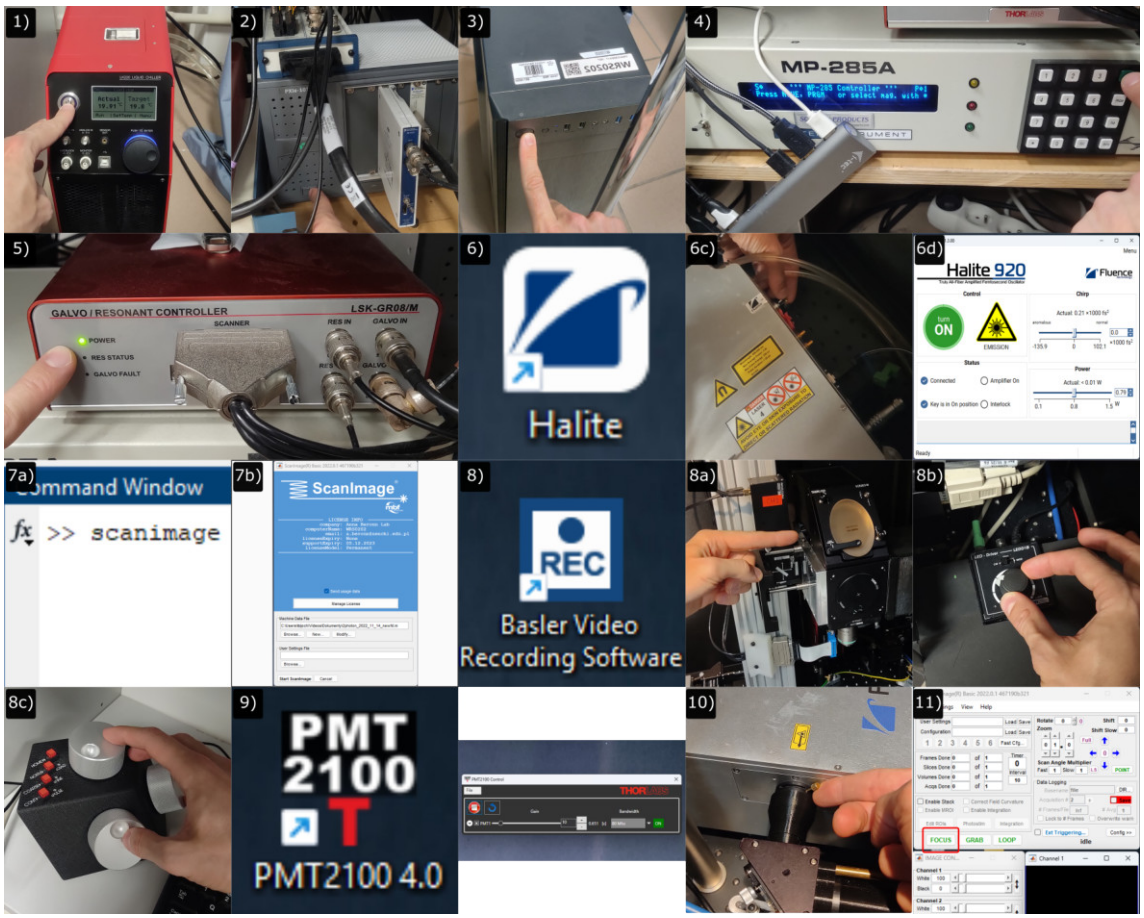

Figure 7.1: Visual manual for the operation of the custom-built Two-Photon Scanning Microscope (TPSM). Photographs illustrate the individual components and software interfaces used during standard operation: (1) chiller, (2) NI acquisition box, (3) control computer, (4) Sutter stage controller, (5) resonant-galvo power supply, (6a) laser control software icon, (6b) laser key switch located at the rear panel of the laser, (6c) laser control software interface, (7a) *Matlab* command line with the `scanimage` command, (7b) *ScanImage* startup window, (8a) *Basler* video recording software for wide-field preview, (8b) black slider setting the detection mode to wide-field, (8c) LED power supply, (8d) manual x–y–z stage controller, (9a) PMT control software icon, (9b) PMT software interface, (10) manual laser shutter lever, and (11) imaging control button in *ScanImage*.

- `0` – no pump active,
- `w` – water pump,
- `s` – sucrose pump,
- `q` – quinine pump.

After each Basler output trigger event, the Teensy transmits a five-column data string via the serial interface. The columns correspond to:

1. Basler frame number (`Basframes`),
2. TPSM frame number (`twoPh_frames`),
3. Encoder forward rotation count,
4. Encoder backward rotation count,
5. Pump status code (`0`, `w`, `s`, or `q`).

This output stream provides a compact and precise synchronization log for subsequent analysis of imaging sequences, locomotive activity, and pump-triggered stimulation events.

7.2.2 Alignment

Figure 7.2 presents a detailed optical layout of the TPSM, with all mirrors and key components labeled. This schematic serves as a reference during alignment and troubleshooting, helping to resolve possible ambiguities in the naming conventions of individual optical elements.

Minor alignment

For minor alignment adjustments, use the two steering mirrors M1 and M2 located directly after the laser output. Remove the plastic covers from the top of the microscope tower that shield the tube lens. Place an IR viewing card in the "upper tower" in front of the M7 mount, and adjust the beam position with M1 so that it passes approximately through the center of the field. Ensure that the galvo mirror is set to its default position by selecting the *"Point"* mode in the *ScanImage* software.

If the beam is steered too far with M1, it may clip on the edge of the resonant mirror. When the beam is centered on this mirror, it should also be approximately centered on the tube lens. Use the clipping to roughly center the beam on the resonant mirror.

Next, place the IR viewing card underneath the objective. Using M2, fine-tune the beam position to achieve a symmetric, vertically propagating beam through the objective. If the rest of the optical path is properly aligned, this quick two-step procedure should restore optimal imaging conditions.

Repeat this alignment sequence several times (typically up to ten iterations) to achieve alignment according to professional standards. After completing the procedure, remember to put back the plastic blanks covering the tube lens.

Aligning the setup for the first time

The following procedure describes the complete optical alignment of the TPSM from the laser output to the detection path.

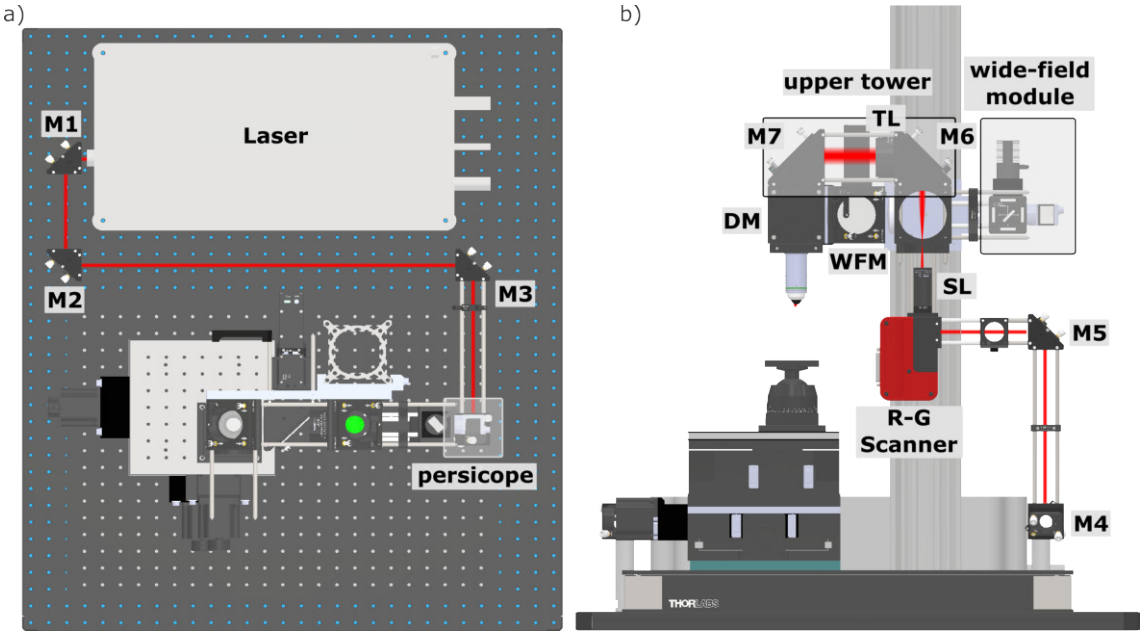

Figure 7.2: Schematic of the TPSM with labeled mirrors and key components. **(a)** Top-view: the excitation beam (depicted in red) is reflected successively from mirrors M1–M3 and enters the periscope through mirror M4. **(b)** Front-view: mirrors M4 and M5 form the periscope, steering the beam toward the Resonant–Galvo Scanner (R–G Scanner). After passing through the Scan Lens (SL), the beam propagates vertically upward to the "upper tower", where it is redirected by two 2-inch elliptical mirrors (M6, M7). The tube lens (TL) is mounted directly to the M6 mirror mount. Following reflection from M7, the beam passes through the long-pass dichroic mirror (DM) and enters the objective. The emitted fluorescence is reflected by the Wide-Field Mirror (WFM), which can be slid into the beam path to direct the fluorescence toward the photomultiplier tubes (PMTs) or retracted to send it to the wide-field camera.

1. **Begin at the laser output.** Verify that the laser beam is roughly centered on each 45° cage kinematic mirror mount using an IR alignment disc. Adjust the mirrors so that the beam propagates parallel to the optical table between M2 and M3.
2. **Align the periscope section.** With M3, center the beam at 45° cage kinematic mount of M4 and with M4, on M5.
3. **Remove the upper tower.** Unscrew the two 2-inch elliptical 45° kinematic mirror mounts of M6 and M7 that hold the Tube Lens and set them aside. Remove the Scan Lens and install the long alignment rods to form a straight optical guide for coarse alignment.
4. **Align to the galvo optical axis.** Using the two periscope mirrors (M4 and M5), steer the beam so that it propagates perfectly upward and coincides with the optical axis of the galvo mirror output. Use the surface of the resonant galvo mirror as an iris for M4: adjust M4 to center the beam on the resonant mirror, and M5 to achieve perfect vertical propagation. Ensure that the galvo power supply is switched on and that the galvo drive voltage is set to 0.0 V.
5. **Verify collinearity through the Scan Lens.** Reinstall the Scan Lens and confirm that the beam travels upward along its optical axis without lateral displacement. If the beam deviates, fine-tune the periscope mirrors until the propagation remains collinear with the Scan Lens axis.
6. **Align the Tube Lens section.** If the Scan Lens alignment is satisfactory, remove it temporarily and reinstall upper tower section. Using all three screws of the kinematic mount of M6, adjust the beam so that it is approximately centered in both mirror housings (M6 and M7). Although not critical for imaging performance, this alignment step simplifies future realignments.
7. **Direct the beam toward the objective position.** With the next mirror, steer the beam so that it passes through the position where the objective will be mounted. Insert the dichroic mirror to account for its small beam displacement.
8. **Reassemble the imaging path.** Reinstall the Scan Lens and Tube Lens. If necessary, translate the entire galvo scanner assembly to ensure that the beam remains collimated after passing through the Tube Lens.
9. **Check the scanning performance.** Activate the scanning mode either through the *ScanImage* software or by applying a constant voltage to the resonant mirror and a sinusoidal voltage to the galvo mirror. Set the maximal scan amplitudes and adjust the M6 and M7 mirrors to minimize clipping across the scan field.
10. **Align the objective.** Insert the objective lens and adjust its z-position so that any clipping visible after the objective (seen as dim edges in the scanned field) appears symmetric.
11. **Verify the imaging path.** Place a fluorescent sample under the objective. Switch to wide-field excitation and detection by sliding out the wide-field mirror (WFM). While scanning, observe the wide-field camera preview and adjust the camera position so that the focus for the 920 nm excitation beam coincides with the fluorescence image. The most efficient procedure is to find the two-photon focus with the stage while performing the scan. The strong two-photon

signal will be visible only when the sample is in 920 nm focus (with a thin sample only). With focus set, shift the wide-field module until the one-photon fluorescence image becomes sharp.

12. **Optimize the detection path.** Switch on the PMT and, using the kinematic mirror that directs fluorescence to the detector, maximize the live signal from the sample.

After completing these steps, the entire TPSM system should be fully aligned and ready for imaging.

7.3 TF Setup Manual

7.3.1 Everyday Operation

1. **Switch on the laser.** Turn the key and enable the amplifier in the control software to reach maximal power (100%).[4]
2. **Wear protective goggles.** This step is mandatory before the shutter is opened as the laser power is hazardous.
3. **Open the laser shutter.** Move the shutter handle to the left. Use an IR viewing card to trace the beam path and verify that the alignment is approximately correct.
4. **Prepare the imaging system.** Switch on the camera and open the corresponding acquisition software (e.g., *Micro-Manager*). With the LED illumination on, locate the focus and define the region of interest (ROI) on the sample using single-photon fluorescence.
5. **Switch to two-photon excitation.** Turn off the LED source and increase the camera exposure time to visualize the two-photon signal. Gradually increase the excitation power by rotating the half-wave plate to its optimal position, either in software or manually using the actuator control buttons.
6. **Optimize the temporal focus.** Adjust the Dispersion Delay Line (DDL, see Fig. 7.3) to maximize the in-focus signal. In *Micro-Manager*, select the ROI and display the mean intensity (Ctrl+m) to monitor the signal level quantitatively.
7. **Begin imaging.** After optimization, the system is ready for acquisition. The sample focus can be adjusted either with the manual micrometer screw or the piezo-driven focusing stage, with the latter being controlled via the software interface (e.g., *Micro-Manager*).

7.3.2 Minor Alignment

During alignment procedures, the optical components are labeled as shown in Fig. 7.3. On the first telescope (L1, L2), the excitation beam should pass through the center of each lens. Adjust the first two steering mirrors (M1, M2) to ensure this condition.

Place a dedicated alignment iris on a short post fixed to the optical table (I1). This iris must be removed after alignment, as it blocks the beam during operation. Close the iris aperture to reduce the beam diameter and make fine alignment easier.

Next, position a second dedicated iris on I2 position – a post behind the Line-Scan Module (LSM). The beam should remain centered on this iris regardless of the LSM displacement along the dovetail rail.

Verify that the beam does not clip on any mirror inside the delay line (M8, M9). Do not change the position of the diffraction grating (DG) under any circumstances. Check that the beam reflects from the central region of each mirror (M8–M14) and passes through the center of every lens (L3–L5). If necessary, use the two mirrors before the grating (M5, M6) to correct the beam position. Once this part of the path

[4]This setting ensures constant pulse dispersion and duration. The power control in the Halite laser is achieved by varying the amplification level, which also affects pulse characteristics.

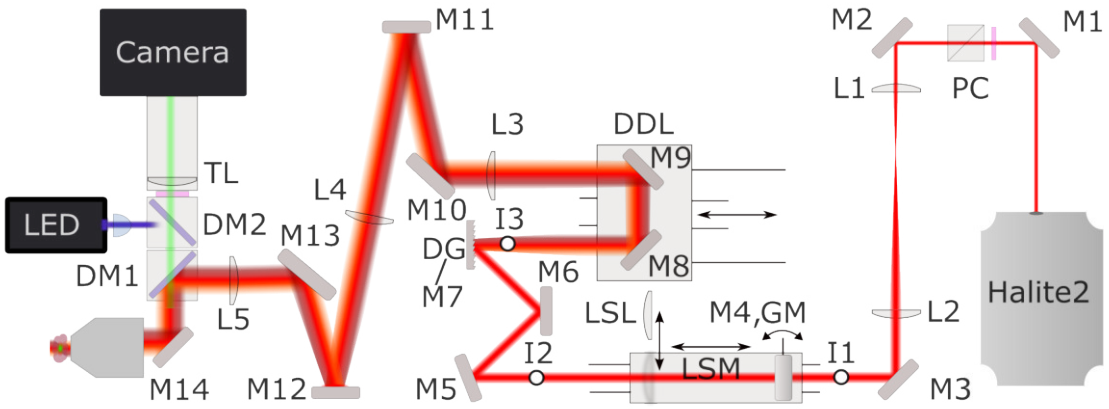

Figure 7.3: Scheme of Temporal Focusing setup with labels. The orientation of the scheme corresponds to the orientation and position of the elements on the optical table.

is aligned, it should not be necessary to touch M8 and M9, and it is recommended to avoid adjusting them.

The next three mirrors (M11, M12, M13) may be used for fine alignment of the beam on subsequent elements – e.g., adjust M11 to center the beam on lens L4, or M13 to center it on the dichroic mirror cube.

When the excitation beam is properly aligned up to the entrance of the microscope body, use a thinned infrared viewing card to observe the beam near the objective's entrance pupil (after M14). If the "rainbow line" of the dispersed beam is not centered, fine-tune M12 until it is centered at the objective pupil.

7.3.3 From Scratch Alignment

Before starting the alignment, remove the LED used for single-photon excitation. Insert a visible alignment beam, for example a red laser pointer, into the excitation path through the dichroic mirror (DM2) using two steering mirrors. Ensure that the beam propagates parallel to the optical table surface.

If adjustment of mirror M14 is required, temporarily remove it and align the visible beam through an iris positioned at the correct height. Reinsert M14, and place an alignment disc or SM1-threaded iris in the objective position. Adjust the position of M14 along its cage rods to align one degree of freedom. Use one screw of the visible beam steering mirror to correct the second degree of freedom.

Next, mount the objective alignment mirror with the SM1–M25 adapter in place of the objective. Adjust M14 so that the reflection of the alignment beam returns directly to the laser source. If necessary, repeat fine shifts of M14 along the rods until back-reflection is perfectly overlapped with the incoming beam and the beam is in the middle of the objective alignment mirror.

Install the wide-field camera and verify that the attenuated visible beam is focused approximately at the center of the camera sensor. Once this is achieved, proceed with the alignment of the remaining excitation optics.

Remove all lenses (L1–L5) from the beam path. Using the dichroic mirror DM1,

center the beam on the position corresponding to L5. Then, with mirrors M13 and M12, center the beam on the middle of the L4 mount. Continue with M11 and M10 to center the beam on the L3 mount and the M9 kinematic cage mount. Ensure that the beam remains parallel to the displacement axis of the dispersion delay line (DDL).

Place an additional iris (I3) before the diffraction grating. Align M9 and M8 so that the beam passes through the center of I3 independently of the DDL translation. Adjust the angle of the diffraction grating so that the zeroth-order reflection follows the visible alignment beam path. This ensures that the grating surface is perpendicular to the optical axis.

Insert lens L5 and verify that the focus of the visible beam lies near the surface of M11. Lens L4 should then collimate the beam, while L3 should focus it onto the diffraction grating for an appropriate DDL position.

Enable the femtosecond laser and, using mirrors M1 and M2, set the beam height and ensure it is parallel to the optical table (use iris I1 as reference). With mirrors M3 and M4, adjust the beam position so that its path does not shift with movement of the Line-Scan Module (LSM).

If necessary, modify the galvo mirror voltage or switch off the power supply and position the galvo manually. Use iris I2 to adjust the horizontal alignment so that the beam travels along the line of threaded holes on the optical table. With mirrors M5 and M6, align the femtosecond beam to the diffraction grating at the same position defined earlier by the visible beam.

Finally, fine-tune both the beam position and the angle of incidence on the grating to ensure that the first order diffraction beam remains stationary during DDL translation. Set the distance between the cylindrical lens (LSL) and the galvo mirror using a caliper to the reference value. Insert lenses L1 and L2 and confirm correct beam collimation without lateral displacement. Mount the objective on the piezo-stage, and the wide-field LED. Next, define the temporal focus by translating DDL and maximizing in-focus signal from a thin, uniform sample of fluorophores. Perform z-scan with the sample and record the mean signal for every z-position. Ensure that the maximum coincides with the focus. If needed use the built-in laser compressor.

7.3.4 Temporal Focusing Line-Scan Operation

The line-scan mode of the temporal focusing microscope requires careful optical alignment and synchronization between the galvo mirror and the camera. The following procedure outlines the steps necessary to align and operate the system in this configuration.

First, ensure that the excitation beam is well aligned along the optical axis. Insert the cylindrical lens (LSL) into the line-scan module (LSM). Fix the correct distance between the LSL and the galvo mirror by tightening the designated cage rod. If this distance has been lost, use a caliper to restore it.

Prepare a thin, uniform fluorescent sample for alignment verification. Remove the diffraction grating and place a flat mirror in its position (M7). Adjust the LSM position along the optical axis to obtain the narrowest possible excitation line in the

wide-field image observed on the camera.

Once the line is optimized, reinstall the diffraction grating. Use the dispersion delay line (DDL) to maximize the fluorescence signal. Iterate between adjusting the LSM position and the DDL until the signal is maximized and the line remains sharp. When approaching the optimal configuration, fix the LSM in the position corresponding to the tightest excitation line and fine-tune the temporal focus using the built-in laser compressor.

After the optical alignment is completed, turn on the galvo mirror power supply. Connect the galvo control input either to the NI-DAQ card output or to a function generator. Using long exposure (e.g. 100 ms) and relatively high frequency sinusoidal driving voltage (e.g. 30 Hz) perform a simple z-scan to verify the axial sectioning obtained with the scanning excitation beam. If the maximum signal intensity does not coincide with the optical focus, adjust the laser compressor to shift the temporal focus accordingly.

Connect a synchronization cable from the control system to the camera's external trigger input.

For continuous operation, apply a sinusoidal or saw-tooth waveform to the galvo control input with the frequency adjusted to the camera exposure. Simultaneously, send TTL synchronization pulses to the camera to trigger frame acquisition. Adjust the TTL delay to ensure a stable image on the camera corresponding to a complete galvo period. Fine adjustments of this delay and waveform parameters may be required to eliminate motion artifacts and maintain temporal synchronization.

7.4 NISE Setup Manual

7.4.1 Everyday Operation

Always wear protective goggles whenever the laser is powered on.
The laser have such power, that even anodized black aluminum beam blocker reflects substantial amount of light that can even melt plastic. For this reason, be extremely careful when working with full power of the laser and never take off the protective goggles when the laser is on.

Depending on the experimental configuration, one of the following laser modules is used:

- **High-Power (HP) Laser:** The HP laser is powered by a rack-mounted cassette module located beneath the optical table. Switch on the main power (rear-panel switch), turn the key to the *"On"* position, and adjust the output power using the front-panel knob. Even 3% of the maximum power is sufficient for beam tracking. This laser has no built-in shutter, therefore a mechanical beam blocker must always be placed in the beam path when not in use. For reliable operation, allow approximately 10 minutes of warm-up time, although in practice the laser is typically stable immediately after startup.
- **High-Stability (LP) Laser:** The LP laser is powered by a compact supply unit located on the right-hand side of the table. Switch on the main power (front-panel switch), turn the key to the *"On"* position, and slowly increase the current using the control knob until the display crosses 2.00 A. If the display remains at 0.0 A, the module may be disabled by a TTL input at the rear-panel connector. In this case, either change the signal in the control software or disconnect the BNC cable. The laser head is equipped with a manual shutter: to open it, place a finger under the round part of the laser head and push the small protruding plate firmly upward until it clicks. Take care not to touch the nearby telescope (T1) during this step.

Beam verification and setup: Use the IR viewing card to verify that the beam is visible and correctly directed. Ensure that the mirror on the magnetic base corresponds to the selected laser module. Switch on the camera and the SiPM detector. Remove the 45° turning mirror from the second magnetic cube and insert the 3D-printed dummy insert to cover the SiPM input and suppress stray light entering the camera's tube lens. Wait for the camera to initialize and run it using e.g. *Micro-Manager*.

Bright-field focusing: Place the sample in the holder. Switch on the bright-field illumination using the LED switch located on the left side of the table. Find the sample focus on the camera preview. If necessary, adjust the position of the bright-field illumination module to achieve Köhler illumination (by imaging the field iris) or move the module backward to reduce illumination intensity.

Finding the laser focus: After the bright-field focus is established, enable the laser beam by removing the beam block or opening the shutter. The 1064 nm excitation focus should coincide with the sharp bright-field image, however with highly nonlinear samples the focus usually needs to be adjusted. For zero-voltage steering of both galvo mirrors, the excitation spot is typically located near the center

of the camera field. A dense fluorescent region in the sample helps to exactly localize the excitation focus via visible luminescence. Medium laser power (half-wave plate set to half attenuation, 3% in HP laser or 2.00A in LP laser) is recommended as it is easier to find the excitation spot. Reducing the strength of the bright-field illumination can also be beneficial, as the luminescence must be brighter than the BF illumination in order to notice it.

Fine focusing: Once the excitation spot is located, move to the region of interest (ROI) and fine-tune the z-focus. Gradually lower the excitation power and maximize the luminescence intensity by adjusting the sample position along the z-axis. Acquire a test scan in the software and optimize the excitation power to achieve the best image quality.

Excitation inspection: For inspection of the excitation beam profile, connect the secondary inspection camera and run the corresponding software. Translate the inspection module to obtain the smallest focus on the inspection camera. I suggest taking out the absorptive filter for higher out-of-focus signal that helps finding the focus. Ensure that in the filter slider of the module no spectral filter is inserted (such configuration can be used for invasive luminescence preview).

Software

The software and the documentation are available on GitHub. Here I describe the structure of the code and provide minimal working examples.

The program is written in `Python` and contains five classes, each with a slightly different purpose:

- **LaserPower (parent)** – power control, laser communication, and power measurements.
- **Scan (inherits LaserPower)** – steering of galvo mirrors, reading voltage from the SiPM, methods for taking scans, and image construction.
- **PowerDependency (inherits LaserPower)** – used for measurements of S-shapes.
- **CameraScan (inherits Scan)** – used for measurements where a camera is used as a detector.
- **DoubleCameraMeasurements (inherits from the classes above)** – handles scan saving, operation of additional motorized stages, and all "front-end" functionality.

Such structure forms the core for a potential GUI application, with all the necessary methods already implemented in the `DoubleCameraMeasurements` class. At present, the easiest way to control the experiment is directly from the Python terminal. After initializing the `DoubleCameraMeasurements` class, the most useful functions are shown below.

Most useful functions:

```
# initialize the class
dcm = DoubleCameraMeasurements(current=2.51, objective="20X",
    number_of_pixels=100, pixel_size=0.15, pixel_duration=5.5,
    is_new=True)

dcm.power_on()  # enable the LP laser

horizontal_voltage = 0  # unit [V]
vertical_voltage = 0    # unit [V]
dcm.put_galvos_to_position(horizontal_voltage, vertical_voltage)

# turn the half-wave plate so that the power is maximal:
dcm.set_angle(dcm.ANGLE_MAX)

# turn the half-wave plate so that the power is minimal:
dcm.set_angle(dcm.ANGLE_MIN)

dcm.measure_power()  # output the current power in the focus

# take the scan and automatically save the results:
dcm.take_scan("SiPM")
```

```
# parameters of the scan set earlier:
dcm.number_of_pixels = 100   # image with 100x100 pixels
dcm.pixel_duration = 3       # pixel dwell time in ms
# set pixel size in um for objective specified earlier (20X):
dcm.pixel_size = 0.2

# measure the S-shape in a given range of angles:
start_angle = dcm.ANGLE_MIN + 5
stop_angle  = dcm.ANGLE_MAX - 1
dcm.take_simple_s_shape(start_angle, stop_angle, number_of_points=50)
```

7.4.2 Minor Alignment

The biggest advantage of relays is that they softens the requirements for precise alignment. Essentially, the most important part is that the beam to coincides with the optical axis of the objective[5]. To check such alignment one should remove the objective and put a IR viewing target in the place of the objective. The large beam should be precisely in the center of the target. After the replacement of the target with "objective alignment reflective mirror", the reflected beam should be trackable till the laser. If both are not the case, then proceed to the alignment routine. See Figure 7.4 for the naming conventions. With a steering mirrors of particular laser (LM1 and M2 or HM1,HM2,HM3) set the beam to pass through the center of the first iris (I1). The second checkpoint is the center of L1 lens after the vertical galvo mirror (use the IR viewing target). With this set (remember that galvo voltages should be set to 0V for the alignment) turn to space between I2 iris and M8 mirror. In this part the beam should be centered on the L6. Use M2 to center the beam on the IR viewing target on L6. If the beam is not centered in the entrance to the objective, center its position with M8. If the beam deflects after placement of the objectibe, try beam walk with M7 and M8 – but that should not be necessary.

7.4.3 From Scratch Alignment

When everything is wrong, cover the laser first and remove all the lenses. Put galvos to position 0,0 volts, ensure that the power supply for galvo mirrors is switched on (it is placed under the table). While removing lenses near the galvo, remove L2 first, and next L1. If the laser was switched on, the tight focus on the galvo mirror surface damages the mirror coating. Align the laser along straight line parallel to the table (i.e. with two irises of the same height) – here it is crucial for T2 to not alter the beam height. The beam should travel above the threaded holes. You can use the housing of M4 mirror in the periscope, as an alignment checkpoint. Then unscrew the galvo from the periscope, and mount long rods in the mirror housing. Use cage plate and IR viewer to set the appropriate tip-tilt of M4 mirror. The beam should travel perfectly upwards. Mount the galvo mirror on the periscope, and set its tilt angle either by hand or by applying voltage, and then saving it as a bias voltage

[5]However, objectives usually have good off-axis corrections, so this is not a requirement for good imaging but rather an alignment in accordance with best experimental practice.

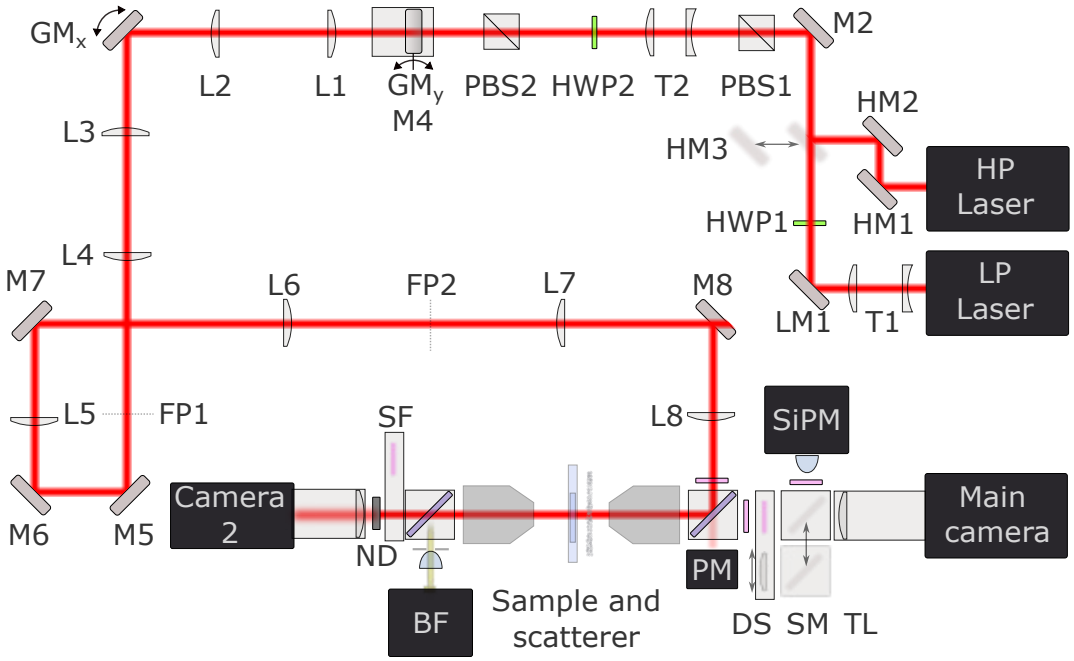

Figure 7.4: Detailed scheme of the setup for NISE. The beam from the low-power laser (LP laser) is expanded by telescope T1 and guided by mirrors LM1 and M2 with I1 iris as the first alignment checkpoint, and mount of M4 mirror as second one. Half-wave plate HP1 sets the polarization of the laser beam so that it is not attenuated by PBS1. The unpolarized high-power laser (HP laser) is introduced into the excitation path using mirrors HM1, HM2, and removable HM3. The polarization is then defined by PBS1. Telescope T2 increases the beam diameter. The half-wave plate (HWP2) and PBS2 are used to control the power of both lasers. Mirror M4 steers the beam upward toward the galvo mirror GM_y. A $4f$ system composed of lenses L1 and L2 images the surface of GM_y onto the second galvo mirror (GM_x). After GM_x, another $4f$ system, consisting of lenses L3 and L4, forms the galvo-conjugated plane FP1. This plane is imaged by lenses L5 and L6 onto FP2, with reflections from mirrors M5, M6, and M7 along the imaging path. Iris I2 can be used for minor alignment. FP2 is then imaged onto the back focal plane of the objective using lenses L7 and L8, with the beam turning at mirror M8 placed between these lenses. After L8, the beam passes through a narrowband laser filter (LF) and reflects from the dichroic mirror DM1 toward the objective. The leakage through DM1 is collected by a power meter (PM). The excitation light can be imaged using the inspection module and inspection camera. An absorptive neutral density filter (ND) can be inserted to attenuate the laser intensity reaching the camera. Conversely, a short-pass filter (SF) can be used for luminescence inspection. A secondary dichroic mirror (DM2), reflecting most of the laser light, is used to introduce the bright-field illumination (BF). Iris FI can be used as field iris to set the Köhler illumination. To observe a wide-field image, the SM mirror is replaced with a dummy insert. The tube lens (TL) images the sample onto the main camera sensor. The detection slider (DS) allows insertion of an additional short-pass filter or a collection lens to improve light collection efficiency for SiPM detection. An additional notch filter (NF) attenuates residual excitation light in both the camera and SiPM detection arms.

(I did not use this route). With periscope mirror and galvo mirror, you have two degrees of freedom to make the beam parallel to the table. Left-right misalignment should be compensated with the mirrors upstream e.g. M2 (only one screw, to not change the beam angle w.r.t the table). After setting the correct height, insert the lenses (switch off the laser and insert L1 first). The lenses (L1 and L2) are mounted on precisely machined posts with height corresponding to the beam height after the periscope. The distance from galvo to the lens can be set using the caliper and the effective focal lengths. Usually the focal lengths are given for visible wavelengths thus if no precise value is available then the measurement of the effective focal length should be done. Check the precise scaling by inserting the camera in the focus of L1 and turn the galvo from -0.7 to 0.7 V (-0.7° to 0.7°). The displacement of the spot with respect to the voltage should be linear with proportionality being the focal length. Place the second lens (L2) to create the static image (irrespective to the galvo angle) in its focal length. Put second galvo precisely in this place and set its default angle to reflect the beam at the right angle. Continue downstream with rest of the 4f relays ensuring good recolimation of the beam. The crucial part is the galvo conjugation with L1 and L2, second 4f relay (L3,L4) mounted precisely will ensure uniform position scaling with galvo angle for both horizontal and vertical galvos. As the post to mount the lenses have fixed heights and the horizontal galvo have no possible tip, the beam after the the part with galvos can be not parallel to the table anymore. Set the beam to be parallel to the table with M5 and M6 mirrors. These mirrors are mounted on a common plate, which can be moved to adjust the precise distance to next relays. These relays (L5,L6 and L7,L8) are most easily set from backwards. First insert L8. With the objective inserted, the beam after the objective should be collimated[6]. Be careful with the laser power here, as the focused beam in the objective can easily burn it. Alternatively find the focus with IR viewing target threaded into the side of the magnetic cube. Insert all the lenses based on collimation. As these are 4f relays, after single telescope, the beam must be in the same place. Adjust the position (height, or shift) of the lens if the resulting beam in the imaging plane is displaced substantially. In case of L8 adjust M8 mirror. If the beam was set to pass through the middle of every lens mount, then no adjustments will be needed. After all the relays set, ensure the proper conjugation by placing the camera instead of the objective and reducing the beam size with the iris before the galvos. The beam should be stationary in all conjugated planes for $\pm 0.7°$ of galvo deflection (with the shortest focal lengths of the singlet lenses being 100 mm). Insert the expanding telescope T2 and fit the beam size at the entrance pupil of the objective to the size of the aperture (chose appropriate lenses). Put a sample of nanoparticles, find a dense, relatively uniform region, and adjusting the telescope collimating lens, shift the focus of the beam axially, so that it coincides with the focus of the bright-field. Calibrate the bright-field magnification (use test-target), then take the scan and compare bright-field image with the scan to introduce proper scaling factor (you can input it in objective dictionary as effective focal length 'f').

[6]note that the Reileigh range is short for small beams, so do not suspect the same size of the beam at the distance larger than 10 cm

Bibliography

[1]A. Tbakhi and S. S. Amr, "Ibn al-haytham: father of modern optics", Annals of Saudi Medicine **27**, 464–467 (2007).

[2]E. Hecht, *Optics Global Edition* (Pearson Deutschland, 2016), p. 728.

[3]T. H. MAIMAN, "Stimulated optical radiation in ruby", Nature **187**, 493–494 (1960).

[4]P. P. Sorokin and M. J. Stevenson, "Stimulated infrared emission from trivalent uranium", Phys. Rev. Lett. **5**, 557–559 (1960).

[5]P. A. Franken, A. E. Hill, C. W. Peters, and G. Weinreich, "Generation of optical harmonics", Phys. Rev. Lett. **7**, 118–119 (1961).

[6]R. W. Boyd, *Nonlinear optics*, 4th, Definitive reference on nonlinear optical phenomena and applications. (Academic Press, 2020).

[7]M. Ebrahim-Zadeh and I. T. Sorokina, eds., *Mid-infrared coherent sources and applications*, 1874-6535 (Springer, 2007).

[8]D. E. Spence, P. N. Kean, and W. Sibbett, "60-fsec pulse generation from a self-mode-locked ti:sapphire laser", Opt. Lett. **16**, 42–44 (1991).

[9]W. Sibbett, A. A. Lagatsky, and C. T. A. Brown, "The development and application of femtosecond laser systems", Opt. Express **20**, 6989–7001 (2012).

[10]L. Gallmann, C. Cirelli, and U. Keller, "Attosecond science: recent highlights and future trends", Annual Review of Physical Chemistry **63**, 447–469 (2012).

[11]D. Strickland and G. Mourou, "Compression of amplified chirped optical pulses", Optics Communications **56**, 219–221 (1985).

[12]F. Krausz and M. Ivanov, "Attosecond physics", Rev. Mod. Phys. **81**, 163–234 (2009).

[13]S. D. Smith, "Lasers, nonlinear optics and optical computers", Nature **316**, 319–324 (1985).

[14]D. C. Burnham and D. L. Weinberg, "Observation of simultaneity in parametric production of optical photon pairs", Phys. Rev. Lett. **25**, 84–87 (1970).

[15]M. H. Key, "Laboratory production of x-ray lasers", Nature **316**, 314–319 (1985).

[16]R. J. Silbey, "Principles of nonlinear optical spectroscopy by shaul mukamel (university of rochester). oxford university press: new york. 1995. xviii + 543 pp. $65.00. isbn 0-19-509278-3.", Journal of the American Chemical Society **118**, 12872–12872 (1996).

[17]H. Ito, "Chemical amplification resists: history and development within ibm", IBM J. Res. Dev. **44**, 119–130 (2000).

[18]W. R. Zipfel, R. M. Williams, and W. W. Webb, "Nonlinear magic: multiphoton microscopy in the biosciences", Nature Biotechnology **21**, 1369–1377 (2003).

[19]P. Luu, S. E. Fraser, and F. Schneider, "More than double the fun with two-photon excitation microscopy", Communications Biology **7**, 364 (2024).

[20]A. Chandra, V. Kumar, U. C. Garnaik, R. Dada, I. Qamar, V. K. Goel, and S. Agarwal, "Unveiling the molecular secrets: a comprehensive review of raman spectroscopy in biological research", ACS Omega **9**, 50049–50063 (2024).

[21]P. Campagnola, "Second harmonic generation imaging microscopy: applications to diseases diagnostics", Analytical Chemistry **83**, PMID: 21446646, 3224–3231 (2011).

[22]M. G. L. Gustafsson, "Nonlinear structured-illumination microscopy: wide-field fluorescence imaging with theoretically unlimited resolution", Proceedings of the National Academy of Sciences **102**, 13081–13086 (2005).

[23]A. P. Mosk, A. Lagendijk, G. Lerosey, and M. Fink, "Controlling waves in space and time for imaging and focusing in complex media", Nature Photonics **6**, 283–292 (2012).

[24]S. W. Hell and J. Wichmann, "Breaking the diffraction resolution limit by stimulated emission: stimulated-emission-depletion fluorescence microscopy", Opt. Lett. **19**, 780–782 (1994).

[25]W. Denk, J. H. Strickler, and W. W. Webb, "Two-photon laser scanning fluorescence microscopy", Science **248**, 73–76 (1990).

[26]N. G. Horton, K. Wang, D. Kobat, C. G. Clark, F. W. Wise, C. B. Schaffer, and C. Xu, "In vivo three-photon microscopy of subcortical structures within an intact mouse brain", Nature Photonics **7**, 205–209 (2013).

[27]J. W. Goodman, *Speckle phenomena in optics: theory and applications*, Second (SPIE Press, 2020).

[28]R. Horstmeyer, H. Ruan, and C. Yang, "Guidestar-assisted wavefront-shaping methods for focusing light into biological tissue", Nature Photonics **9**, 563–571 (2015).

[29]H. Yu, J. Park, K. Lee, J. Yoon, K. Kim, S. Lee, and Y. Park, "Recent advances in wavefront shaping techniques for biomedical applications", Current Applied Physics **15**, 632–641 (2015).

[30]J. Bertolotti and O. Katz, "Imaging in complex media", Nature Physics **18**, 1008–1017 (2022).

[31]S. Gigan, O. Katz, H. B. de Aguiar, E. R. Andresen, A. Aubry, J. Bertolotti, E. Bossy, D. Bouchet, J. Brake, S. Brasselet, Y. Bromberg, H. Cao, T. Chaigne, Z. Cheng, W. Choi, T. Čižmár, M. Cui, V. R. Curtis, H. Defienne, M. Hofer, R. Horisaki, R. Horstmeyer, N. Ji, A. K. LaViolette, J. Mertz, C. Moser, A. P. Mosk, N. C. Pégard, R. Piestun, S. Popoff, D. B. Phillips, D. Psaltis, B. Rahmani, H. Rigneault, S. Rotter, L. Tian, I. M. Vellekoop, L. Waller, L. Wang, T. Weber, S. Xiao, C. Xu, A. Yamilov, C. Yang, and H. Yılmaz, "Roadmap on wavefront shaping and deep imaging in complex media", Journal of Physics: Photonics **4**, 042501 (2022).

[32]A. Labeyrie, "Attainment of diffraction limited resolution in large telescopes by fourier analyzing speckle patterns", Astronomy and Astrophysics **6**, 85–87 (1970).

[33]A. P. Gibson, J. C. Hebden, and S. R. Arridge, "Recent advances in diffuse optical imaging", Physics in Medicine & Biology **50**, R1 (2005).

[34]Y. H. M.D. and Y. Yamada, "Overview of diffuse optical tomography and its clinical applications", Journal of Biomedical Optics **21**, 091312 (2016).

[35]I. M. Vellekoop and A. P. Mosk, "Focusing coherent light through opaque strongly scattering media", Opt. Lett. **32**, 2309–2311 (2007).

[36]I. Freund, M. Rosenbluh, and S. Feng, "Memory effects in propagation of optical waves through disordered media", Physical review letters **61**, 2328 (1988).

[37]O. Katz, E. Small, Y. Guan, and Y. Silberberg, "Noninvasive nonlinear focusing and imaging through strongly scattering turbid layers", Optica **1**, 170–174 (2014).

[38]I. M. Vellekoop, "Feedback-based wavefront shaping", Opt. Express **23**, 12189–12206 (2015).

[39]D. B. Conkey, A. M. Caravaca-Aguirre, and R. Piestun, "High-speed scattering medium characterization with application to focusing light through turbid media", Opt. Express **20**, 1733–1740 (2012).

[40]B. Blochet, L. Bourdieu, and S. Gigan, "Focusing light through dynamical samples using fast continuous wavefront optimization", Opt. Lett. **42**, 4994–4997 (2017).

[41]D. Feldkhun, O. Tzang, K. H. Wagner, and R. Piestun, "Focusing and scanning through scattering media in microseconds", Optica **6**, 72–75 (2019).

[42]C.-L. Hsieh, Y. Pu, R. Grange, and D. Psaltis, "Digital phase conjugation of second harmonic radiation emitted by nanoparticles in turbid media", Opt. Express **18**, 12283–12290 (2010).

[43]A. Boniface, B. Blochet, J. Dong, and S. Gigan, "Noninvasive light focusing in scattering media using speckle variance optimization", Optica **6**, 1381–1385 (2019).

[44]X. Xu, H. Liu, and L. V. Wang, "Time-reversed ultrasonically encoded optical focusing into scattering media", Nature Photonics **5**, 154–157 (2011).

[45]Y. Liu, P. Lai, C. Ma, X. Xu, A. A. Grabar, and L. V. Wang, "Optical focusing deep inside dynamic scattering media with near-infrared time-reversed ultrasonically encoded (true) light", Nature Communications **6**, 5904 (2015).

[46]S. M. Popoff, G. Lerosey, R. Carminati, M. Fink, A. C. Boccara, and S. Gigan, "Measuring the transmission matrix in optics: an approach to the study and control of light propagation in disordered media", Phys. Rev. Lett. **104**, 100601 (2010).

[47]S. Popoff, G. Lerosey, M. Fink, A. C. Boccara, and S. Gigan, "Image transmission through an opaque material", Nature Communications **1**, 81 (2010).

[48]G. Osnabrugge, R. Horstmeyer, I. N. Papadopoulos, B. Judkewitz, and I. M. Vellekoop, "Generalized optical memory effect", Optica **4**, 886–892 (2017).

[49]J. Bertolotti, E. G. van Putten, C. Blum, A. Lagendijk, W. L. Vos, and A. P. Mosk, "Non-invasive imaging through opaque scattering layers", Nature **491**, 232–234 (2012).

[50]O. Katz, E. Small, and Y. Silberberg, "Looking around corners and through thin turbid layers in real time with scattered incoherent light", Nature Photonics **6**, 549–553 (2012).

[51]A. Makowski, W. Zwolinski, P. Szczypkowski, B. Gorzkowski, S. Gigan, and R. Lapkiewicz, *Low photon number non-invasive imaging through time-varying diffusers*, 2024.

[52]O. Haim, J. Boger-Lombard, and O. Katz, "Image-guided computational holographic wavefront shaping", Nature Photonics **19**, 44–53 (2025).

[53]Y. Baek, H. B. de Aguiar, and S. Gigan, "Phase conjugation with spatially incoherent light in complex media", Nature Photonics **17**, 1114–1119 (2023).

[54]Ł. Bijoch, P. Szczypkowski, J. Wiśniewska, M. Pawłowska, K. Hajdukiewicz, R. Łapkiewicz, and A. Beroun, "Opposing effects of rewarding and aversive stimuli on d1 and d2 types of dopamine-sensitive neurons in the central amygdala", bioRxiv, `10.1101/2024.11.07.622413` (2024).

[55]P. Szczypkowski, M. Pawlowska, and R. Lapkiewicz, "3d super-resolution optical fluctuation imaging with temporal focusing two-photon excitation", Biomed. Opt. Express **15**, 4381–4389 (2024).

[56]P. Szczypkowski, A. Makowski, W. Zwoliński, K. Prorok, P. Wasylczyk, A. Bednarkiewicz, and R. Lapkiewicz, *Overcoming light scattering with high optical nonlinearity*, 2025.

[57]J. Mertz, *Introduction to optical microscopy*, 2nd (Cambridge University Press, Cambridge, 2019).

[58]E. Abbe, "Beiträge zur theorie des mikroskops und der mikroskopischen wahrnehmung", Archiv für Mikroskopische Anatomie **9**, 413–468 (1873).

[59]L. Loetgering, *Computational imaging*, Lecture Notes, 2023.

[60]Rayleigh, "Xxxi. investigations in optics, with special reference to the spectroscope", The London, Edinburgh, and Dublin Philosophical Magazine and Journal of Science **8**, 261–274 (1879).

[61]E. Betzig, "Proposed method for molecular optical imaging", Opt. Lett. **20**, 237–239 (1995).

[62]E. Betzig, G. H. Patterson, R. Sougrat, O. W. Lindwasser, S. Olenych, J. S. Bonifacino, M. W. Davidson, J. Lippincott-Schwartz, and H. F. Hess, "Imaging intracellular fluorescent proteins at nanometer resolution", Science **313**, 1642–1645 (2006).

[63]F. Balzarotti, Y. Eilers, K. C. Gwosch, A. H. Gynnå, V. Westphal, F. D. Stefani, J. Elf, and S. W. Hell, "Nanometer resolution imaging and tracking of fluorescent molecules with minimal photon fluxes", Science **355**, 606–612 (2017).

[64]K. C. Gwosch, J. K. Pape, F. Balzarotti, P. Hoess, J. Ellenberg, J. Ries, and S. W. Hell, "Minflux nanoscopy delivers 3d multicolor nanometer resolution in cells", Nature Methods **17**, 217–224 (2020).

[65]M. G. L. Gustafsson, "Surpassing the lateral resolution limit by a factor of two using structured illumination microscopy", Journal of Microscopy **198**, 82–87 (2000).

[66]T. Dertinger, R. Colyer, G. Iyer, S. Weiss, and J. Enderlein, "Fast, background-free, 3d super-resolution optical fluctuation imaging (sofi)", Proceedings of the National Academy of Sciences **106**, 22287–22292 (2009).

[67]A. Sroda, A. Makowski, R. Tenne, U. Rossman, G. Lubin, D. Oron, and R. Lapkiewicz, "Sofism: super-resolution optical fluctuation image scanning microscopy", Optica **7**, 1308–1316 (2020).

[68]A. Krupinski-Ptaszek, A. Makowski, A. Mielnicka, M. Pawłowska, R. Tenne, and R. Lapkiewicz, "Super-resolution microscopy based on the inherent fluctuations of dye molecules", Biomed. Opt. Express **16**, 910–921 (2025).

[69]C. J. R. Sheppard, S. B. Mehta, and R. Heintzmann, "Superresolution by image scanning microscopy using pixel reassignment", Opt. Lett. **38**, 2889–2892 (2013).

[70]R. S. Fischer, Y. Wu, P. Kanchanawong, H. Shroff, and C. M. Waterman, "Microscopy in 3d: a biologist's toolbox", Trends in Cell Biology **21**, 682–691 (2011).

[71]F. Helmchen and W. Denk, "Deep tissue two-photon microscopy", Nature Methods **2**, 932–940 (2005).

[72]L. Kou, D. Labrie, and P. Chylek, "Refractive indices of water and ice in the 0.65- to 2.5-μm spectral range", Appl. Opt. **32**, 3531–3540 (1993).

[73]M. Wang, M. Kim, F. Xia, and C. Xu, "Impact of the emission wavelengths on in vivo multiphoton imaging of mouse brains", Biomed. Opt. Express **10**, 1905–1918 (2019).

[74]T. Wang, C. Wu, D. G. Ouzounov, W. Gu, F. Xia, M. Kim, X. Yang, M. R. Warden, and C. Xu, "Quantitative analysis of 1300-nm three-photon calcium imaging in the mouse brain", eLife **9**, edited by R. Yasuda and C. Dulac, e53205 (2020).

[75]T. Wang, D. G. Ouzounov, M. Wang, and C. Xu, "Quantitative comparison of two-photon and three-photon activity imaging of gcamp6s-labeled neurons in vivo in the mouse brain", in Optics in the life sciences congress (2017), BrM4B.4.

[76]D. Kobat, M. E. Durst, N. Nishimura, A. W. Wong, C. B. Schaffer, and C. Xu, "Deep tissue multiphoton microscopy using longer wavelength excitation", Opt. Express **17**, 13354–13364 (2009).

[77]D. Huang, E. A. Swanson, C. P. Lin, J. S. Schuman, W. G. Stinson, W. Chang, M. R. Hee, T. Flotte, K. Gregory, C. A. Puliafito, and J. G. Fujimoto, "Optical coherence tomography", Science **254**, 1178–1181 (1991).

[78]K. Karnowski, A. Ajduk, B. Wieloch, S. Tamborski, K. Krawiec, M. Wojtkowski, and M. Szkulmowski, "Optical coherence microscopy as a novel, non-invasive method for the 4d live imaging of early mammalian embryos", Scientific Reports **7**, 4165 (2017).

[79]X. Wang, Y. Pang, G. Ku, X. Xie, G. Stoica, and L. V. Wang, "Noninvasive laser-induced photoacoustic tomography for structural and functional in vivo imaging of the brain", Nature Biotechnology **21**, 803–806 (2003).

[80]D. A. Boas, D. H. Brook, E. L. Miller, C. A. Dimarzio, M. Kilmebr, R. Gaudett, and Q. Zhang, "Imaging the Body with Diffuse Opticle Tomogaphy", IEEE Signal Processing Magazine **18**, 57–75 (2001).

[81]M. Göppert-Mayer, "Über elementarakte mit zwei quantensprüngen", Annalen der Physik **401**, 273–294 (1931).

[82]P. Szczypkowski, "Two-photon wide-field microscopy with temporal focusing", Masters thesis (University of Warsaw, Warsaw, Poland, Sept. 2021).

[83]P. Colarusso and C. Brideau, *Ewhat is two-photon microscopy?*, (2022) `https://bliqphotonics.com/what-is-two-photon-microscopy/` (visited on 09/20/2025).

[84]C. Tischbirek, A. Birkner, H. Jia, B. Sakmann, and A. Konnerth, "Deep two-photon brain imaging with a red-shifted fluorometric ca²⁺ indicator", Proceedings of the National Academy of Sciences **112**, 11377–11382 (2015).

[85]P. Theer and W. Denk, "On the fundamental imaging-depth limit in two-photon microscopy", J. Opt. Soc. Am. A **23**, 3139–3149 (2006).

[86]P. Theer, M. T. Hasan, and W. Denk, "Two-photon imaging to a depth of 1000 µm in living brains by use of a ti:al2o3 regenerative amplifier", Opt. Lett. **28**, 1022–1024 (2003).

[87]N. C. Bruce, F. E. W. Schmidt, J. C. Dainty, N. P. Barry, S. C. W. Hyde, and P. M. W. French, "Investigation of the temporal spread of an ultrashort light pulse on transmission through a highly scattering medium", Appl. Opt. **34**, 5823–5828 (1995).

[88]O. Katz, E. Small, Y. Bromberg, and Y. Silberberg, "Focusing and compression of ultrashort pulses through scattering media", Nature Photonics **5**, 372–377 (2011).

[89]H. Kawano, Y. Nabekawa, A. Suda, Y. Oishi, H. Mizuno, A. Miyawaki, and K. Midorikawa, "Attenuation of photobleaching in two-photon excitation fluorescence from green fluorescent protein with shaped excitation pulses", Biochemical and Biophysical Research Communications **311**, 592–596 (2003).

[90]P. Yao, R. Liu, T. Broggini, M. Thunemann, and D. Kleinfeld, "Construction and use of an adaptive optics two-photon microscope with direct wavefront sensing", Nature Protocols **18**, 3732–3766 (2023).

[91]J. R. Lakowicz, *Principles of fluorescence spectroscopy*, 3rd (Springer, 2006).

[92]A. K. Dunn, V. P. Wallace, M. Coleno, M. W. Berns, and B. J. Tromberg, "Influence of optical properties on two-photon fluorescence imaging in turbid samples", Appl. Opt. **39**, 1194–1201 (2000).

[93]J. B. Pawley, ed., *Handbook of biological confocal microscopy*, 3rd (Springer, 2006).

[94]O. Tzang, D. Feldkhun, A. Agrawal, A. Jesacher, and R. Piestun, "Two-photon psf-engineered image scanning microscopy", Opt. Lett. **44**, 895–898 (2019).

[95]S. V. Koho, E. Slenders, G. Tortarolo, M. Castello, M. Buttafava, F. Villa, E. Tcarenkova, M. Ameloot, P. Bianchini, C. J. R. Sheppard, A. Diaspro, A. Tosi, and G. Vicidomini, "Two-photon image-scanning microscopy with spad array and blind image reconstruction", Biomed. Opt. Express **11**, 2905–2924 (2020).

[96]G. Thériault, Y. D. Koninck, and N. McCarthy, "Extended depth of field microscopy for rapid volumetric two-photon imaging", Opt. Express **21**, 10095–10104 (2013).

[97]J. L. Fan, J. A. Rivera, W. Sun, J. Peterson, H. Haeberle, S. Rubin, and N. Ji, "High-speed volumetric two-photon fluorescence imaging of neurovascular dynamics", Nature Communications **11**, 6020 (2020).

[98]J. Giblin, S. Kura, J. L. U. Nunuez, J. Zhang, G. Kureli, J. Jiang, D. A. Boas, and I. A. Chen, "High throughput detection of capillary stalling events with Bessel beam two-photon microscopy", Neurophotonics **10**, 035009 (2023).

[99]L. Lu, B. T. Hope, J. Dempsey, S. Y. Liu, J. M. Bossert, and Y. Shaham, "Central amygdala erk signaling pathway is critical to incubation of cocaine craving", Nature Neuroscience **8**, 212–219 (2005).

[100]B. S. McEwen, "Physiology and neurobiology of stress and adaptation: central role of the brain", Physiological Reviews **87**, PMID: 17615391, 873–904 (2007).

[101]E. Knapska, V. Lioudyno, A. Kiryk, M. Mikosz, T. Górkiewicz, P. Michaluk, M. Gawlak, M. Chaturvedi, G. Mochol, M. Balcerzyk, D. K. Wojcik, G. M. Wilczynski, and L. Kaczmarek, "Reward learning requires activity of matrix metalloproteinase-9 in the central amygdala", Journal of Neuroscience **33**, 14591–14600 (2013).

[102]M. Toth, "Mechanisms of non-genetic inheritance and psychiatric disorders", Neuropsychopharmacology **40**, 129–140 (2015).

[103]J. Kim, X. Zhang, S. Muralidhar, S. A. LeBlanc, and S. Tonegawa, "Basolateral to central amygdala neural circuits for appetitive behaviors", Neuron **93**, 1464–1479.e5 (2017).

[104]Ł. Bijoch, J. Klos, M. Pękała, K. Fiołna, L. Kaczmarek, and A. Beroun, "Diverse processing of pharmacological and natural rewards by the central amygdala", Cell Reports **42**, 113036 (2023).

[105]Y. Bando, C. Grimm, V. H. Cornejo, and R. Yuste, "Genetic voltage indicators", BMC Biology **17**, 71 (2019).

[106]Y. Han, J. Yang, Y. Li, Y. Chen, H. Ren, R. Ding, W. Qian, K. Ren, B. Xie, M. Deng, Y. Xiao, J. Chu, and P. Zou, "Bright and sensitive red voltage indicators for imaging action potentials in brain slices and pancreatic islets", Science Advances **9**, eadi4208 (2023).

[107]C. Grienberger, A. Giovannucci, W. Zeiger, and C. Portera-Cailliau, "Two-photon calcium imaging of neuronal activity", Nature Reviews Methods Primers **2**, 67 (2022).

[108]D. Oron, E. Tal, and Y. Silberberg, "Scanningless depth-resolved microscopy", Opt. Express **13**, 1468–1476 (2005).

[109]G. Zhu, J. van Howe, M. Durst, W. Zipfel, and C. Xu, "Simultaneous spatial and temporal focusing of femtosecond pulses", Opt. Express **13**, 2153–2159 (2005).

[110]C.-Y. Chang, Y. Y. Hu, C.-Y. Lin, C.-H. Lin, H.-Y. Chang, S.-F. Tsai, T.-W. Lin, and S.-J. Chen, "Fast volumetric imaging with patterned illumination via digital micro-mirror device-based temporal focusing multiphoton microscopy", Biomed. Opt. Express **7**, 1727–1736 (2016).

[111]E. Tal, D. Oron, and Y. Silberberg, "Improved depth resolution in video-rate line-scanning multiphoton microscopy using temporal focusing", Opt. Lett. **30**, 1686–1688 (2005).

[112]M. Pawlowska, R. Tenne, B. Ghosh, A. Makowski, and R. Lapkiewicz, "Embracing the uncertainty: the evolution of sofi into a diverse family of fluctuation-based super-resolution microscopy methods", Journal of Physics: Photonics **4**, 012002 (2021).

[113]A. Girsault, T. Lukes, A. Sharipov, S. Geissbuehler, M. Leutenegger, W. Vandenberg, P. Dedecker, J. Hofkens, and T. Lasser, "Sofi simulation tool: a software package for simulating and testing super-resolution optical fluctuation imaging", PLOS ONE **11**, 1–13 (2016).

[114]P. Dedecker, S. Duwé, R. K. Neely, and J. Zhang, *Localizer: Localization Microscopy Toolkit for IGOR Pro*, `https://www.wavemetrics.com/project/Localizer`, Accessed: 2025-10-24, 2025.

[115]J. Mertz, "Strategies for volumetric imaging with a fluorescence microscope", Optica **6**, 1261–1268 (2019).

[116]A. H. VOIE, D. H. BURNS, and F. A. SPELMAN, "Orthogonal-plane fluorescence optical sectioning: three-dimensional imaging of macroscopic biological specimens", Journal of Microscopy **170**, 229–236 (1993).

[117]T. V. Truong, W. Supatto, D. S. Koos, J. M. Choi, and S. E. Fraser, "Deep and fast live imaging with two-photon scanned light-sheet microscopy", Nature Methods **8**, 757–760 (2011).

[118]R. M. Power and J. Huisken, "A guide to light-sheet fluorescence microscopy for multiscale imaging", Nature Methods **14**, 360–373 (2017).

[119]C. Dunsby, "Optically sectioned imaging by oblique plane microscopy", Opt. Express **16**, 20306–20316 (2008).

[120]D. Meshulach and Y. Silberberg, "Coherent quantum control of two-photon transitions by a femtosecond laser pulse", Nature **396**, 239–242 (1998).

[121]A. Escobet-Montalbán, R. Spesyvtsev, M. Chen, W. A. Saber, M. Andrews, C. S. Herrington, M. Mazilu, and K. Dholakia, "Wide-field multiphoton imaging through scattering media without correction", Science Advances **4**, eaau1338 (2018).

[122]C. Zheng, J. K. Park, M. Yildirim, J. R. Boivin, Y. Xue, M. Sur, P. T. C. So, and D. N. Wadduwage, "De-scattering with excitation patterning enables rapid wide-field imaging through scattering media", Science Advances **7**, eaay5496 (2021).

[123]N. Wijethilake, M. Anandakumar, C. Zheng, P. T. C. So, M. Yildirim, and D. N. Wadduwage, "Deep-squared: deep learning powered de-scattering with excitation patterning", Light: Science & Applications **12**, 228 (2023).

[124]E. MEI, P. FOMITCHOV, R. GRAVES, and M. CAMPION, "A line scanning confocal fluorescent microscope using a cmos rolling shutter as an adjustable aperture", Journal of Microscopy **247**, 269–276 (2012).

[125]E. Baumgart and U. Kubitscheck, "Scanned light sheet microscopy with confocal slit detection", Opt. Express **20**, 21805–21814 (2012).

[126]B. Torrado, B. Pannunzio, L. Malacrida, and M. A. Digman, "Fluorescence lifetime imaging microscopy", Nature Reviews Methods Primers **4**, 80 (2024).

[127]A. J. Bowman, C. Huang, M. J. Schnitzer, and M. A. Kasevich, "Wide-field fluorescence lifetime imaging of neuron spiking and subthreshold activity in vivo", Science **380**, 1270–1275 (2023).

[128]A. J. Bowman, B. B. Klopfer, T. Juffmann, and M. A. Kasevich, "Electro-optic imaging enables efficient wide-field fluorescence lifetime microscopy", Nature Communications **10**, 4561 (2019).

[129]A. Macioch, "Spad arrays for fluorescence lifetime microscopy", Bachelor's thesis (University of Warsaw, Warsaw, Poland, Sept. 2025).

[130]C. Lee, E. Z. Xu, Y. Liu, A. Teitelboim, K. Yao, A. Fernandez-Bravo, A. M. Kotulska, S. H. Nam, Y. D. Suh, A. Bednarkiewicz, B. E. Cohen, E. M. Chan, and P. J. Schuck, "Giant nonlinear optical responses from photon-avalanching nanoparticles", Nature **589**, 230–235 (2021).

[131]I. N. Papadopoulos, J.-S. Jouhanneau, J. F. A. Poulet, and B. Judkewitz, "Scattering compensation by focus scanning holographic aberration probing (f-sharp)", Nature Photonics **11**, 116–123 (2017).

[132]T. Čižmár and K. Dholakia, "Exploiting multimode waveguides for pure fibre-based imaging", Nature Communications **3**, 1027 (2012).

[133]L. Zhu, F. Soldevila, C. Moretti, A. d'Arco, A. Boniface, X. Shao, H. B. de Aguiar, and S. Gigan, "Large field-of-view non-invasive imaging through scattering layers using fluctuating random illumination", Nature Communications **13**, 1447 (2022).

[134]G. Weinberg, E. Sunray, and O. Katz, "Noninvasive megapixel fluorescence microscopy through scattering layers by a virtual incoherent reflection matrix", Science Advances **10**, eadl5218 (2024).

[135]O. Katz, P. Heidmann, M. Fink, and S. Gigan, "Non-invasive single-shot imaging through scattering layers and around corners via speckle correlations", Nature Photonics **8**, 784–790 (2014).

[136]Z. Yaqoob, D. Psaltis, M. S. Feld, and C. Yang, "Optical phase conjugation for turbidity suppression in biological samples", Nature Photonics **2**, 110–115 (2008).

[137]P. Lai, L. Wang, J. W. Tay, and L. V. Wang, "Photoacoustically guided wavefront shaping for enhanced optical focusing in scattering media", Nature Photonics **9**, 126–132 (2015).

[138]B. Judkewitz, R. Horstmeyer, I. M. Vellekoop, I. N. Papadopoulos, and C. Yang, "Translation correlations in anisotropically scattering media", Nature Physics **11**, 684–689 (2015).

[139]M. Abramowitz and I. A. Stegun, eds., *Handbook of mathematical functions with formulas, graphs, and mathematical tables*, Vol. 55, Applied Mathematics Series, See Eq. (6.1.41) for $\Gamma(x+a)/\Gamma(x) \sim x^a$ as $x \to \infty$ (National Bureau of Standards, Washington, D.C., 1964).

[140]S. Aggarwal, "Recent advances in fundamental research on photon avalanches on the nanometre scale", Nanoscale **17**, 6329–6361 (2025).

[141]M. Szalkowski, A. Kotulska, M. Dudek, Z. Korczak, M. Majak, L. Marciniak, M. Misiak, K. Prorok, A. Skripka, P. J. Schuck, E. M. Chan, and A. Bednarkiewicz, "Advances in the photon avalanche luminescence of inorganic lanthanide-doped nanomaterials", Chem. Soc. Rev. **54**, 983–1026 (2025).

[142]A. Boniface, J. Dong, and S. Gigan, "Non-invasive focusing and imaging in scattering media with a fluorescence-based transmission matrix", Nature Communications **11**, 6154 (2020).

[143]D. Débarre, E. J. Botcherby, T. Watanabe, S. Srinivas, M. J. Booth, and T. Wilson, "Image-based adaptive optics for two-photon microscopy", Opt. Lett. **34**, 2495–2497 (2009).

[144]C. Wang and N. Ji, "Characterization and improvement of three-dimensional imaging performance of grin-lens-based two-photon fluorescence endomicroscopes with adaptive optics", Opt. Express **21**, 27142–27154 (2013).

[145]M. Castello, G. Tortarolo, M. Buttafava, T. Deguchi, F. Villa, S. Koho, L. Pesce, M. Oneto, S. Pelicci, L. Lanzanó, P. Bianchini, C. J. R. Sheppard, A. Diaspro, A. Tosi, and G. Vicidomini, "A robust and versatile platform for image scanning microscopy enabling super-resolution flim", Nature Methods **16**, 175–178 (2019).

[146]E. Sisamakis, M. Tillmann, F. Koberling, T. Roehlicke, M. Wahl, I. M. Antolovic, U. Ortmann, V. Reiter-Scherer, and R. Erdmann, "Small spad-arrays for confocal fluorescence lifetime imaging", Biophysical Journal **123**, 432a (2024).

[147]V. Zickus, M.-L. Wu, K. Morimoto, V. Kapitany, A. Fatima, A. Turpin, R. Insall, J. Whitelaw, L. Machesky, C. Bruschini, D. Faccio, and E. Charbon, "Fluorescence lifetime imaging with a megapixel spad camera and neural network lifetime estimation", Scientific Reports **10**, 20986 (2020).

[148]Q. Li, W. Li, W. Chu, Y. Cao, W. Zhang, H. Ma, Z. Jin, and Y. Dai, "Effect of spatio-temporal coupling on ultrafast laser direct writing in glass", Chin. Opt. Lett. **17**, 081402 (2019).

[149]C. Wang, Z. Wen, R. Pu, B. Pan, B. Wang, K. Zheng, Y. Du, and Q. Zhan, "Tandem photon avalanches for various nanoscale emitters with optical nonlinearity up to 41st-order through interfacial energy transfer", Advanced Materials **36**, 2307848 (2024).

[150]M. Zhang, P. Huang, W. Zheng, X. Song, X. Shang, W. Zhang, D. Yang, X. Yi, and X. Chen, "Lanthanide-doped kmgf3 upconversion nanoparticles for photon avalanche luminescence with giant nonlinearities", Nano Letters **23**, 8576–8584 (2023).

[151]A. Skripka and E. M. Chan, "Unraveling the myths and mysteries of photon avalanching nanoparticles", Mater. Horiz. **12**, 3575–3597 (2025).

[152]H. Dong, L.-Q. Guan, S. Qiao, Y. Liang, Z. Zhu, J.-W. Zhang, X.-Y. Wang, Y. Ni, X. Guo, Z.-Y. Lyu, X.-F. Yang, L.-D. Sun, Q. Zhan, and C.-H. Yan, "Parallel photon avalanche nanoparticles for tunable emission and multicolour sub-diffraction microscopy", Nature Photonics **19**, 692–700 (2025).

[153]Y. Lin, Y. Yao, W. Zhang, Q. Fang, L. Zhang, Y. Zhang, and Y. Xu, "Applications of upconversion nanoparticles in cellular optogenetics", Acta Biomaterialia **135**, 1–12 (2021).

[154]L. Zou, Z.-H. Chen, R. Fang, X. Liu, K. Xu, J. Ding, J. Wang, F. Zhang, Y. Fang, and H. Tian, "Upconversion nanoparticle-delivery flexible optrodes for long-lasting multichannel electrophysiology and transcranial nir optogenetics", ACS Nano **19**, 10966–10976 (2025).

[155]P. Rajchel-Mieldzioć, A. Bednarkiewicz, K. Prorok, and P. Fita, "Strong emission enhancement via dual-wavelength coexcitation in ybtm-doped upconverting nanoparticles for near-infrared and subdiffraction imaging", ACS Nano **19**, 26932–26941 (2025).

[156]R. Zhang, J. Du, Y. He, D. Yuan, J. Luo, D. Wu, B. Ye, Z.-C. Luo, and Y. Shen, "Characterization of the spectral memory effect of scattering media", Opt. Express **29**, 26944–26954 (2021).

[157]N. Badt and O. Katz, "Real-time holographic lensless micro-endoscopy through flexible fibers via fiber bundle distal holography", Nature Communications **13**, 6055 (2022).

[158]D. L. Fried, "Anisoplanatism in adaptive optics", J. Opt. Soc. Am. **72**, 52–61 (1982).

Acknowledgments

Here, I want to express my gratitude to all the people who accompanied me on my way through my PhD journey.

Foremost, I would like to thank my supervisor, Radek Lapkiewicz, for being not just a supervisor but a true mentor, a wisdom-teller, a humble person with amazing physical intuition, who stimulated me to think and act. Thank you for creating a flexible, open environment, for always being willing to discuss new ideas, and for your genuine care for people, your support and your commitment to pursuing interesting science.

I would also like to thank Prof. Stacewicz for agreeing to supervise this thesis and for his valuable feedback – both on the manuscript and on my scientific path.

I am really thankful that I met all my collaborators and friends from the laboratory and from the faculty.

Thank you, Przemek Słota, for always being willing to assess my new ideas, for countless hours of conversations, for teaching me how to use the milling machine and the lathe, for lending me every possible piece of equipment, and for always being open to talk and help.

Thank you, Adrian Makowski, for your extraordinary attitude to science for being both funny and open-minded, and for teaching me a lot about how to work efficiently in science.

Thank you, Aleksander Krupiński-Ptaszek, for all our conversations about the experimental setups, helping to understand SOFI and for your encouragement when I felt down. Thank you for sharing your code and helping with the two-photon ISM with data analysis and experiments.

Thank you, Monika Pawłowska, for tolerating my stubbornness and occasional insubordination – and still choosing to work with me.

Thank you, Sanjukta Kundu, for being the spirit of the group, always ready to talk and share.

Thank you, Bohnishikha Ghosh, for your good advice.

Thank you, Bernard Gorzkowski, for always being willing to give feedback on presentations and texts.

Thank you, Wojciech Zwoliński, for countless conversations about theory and for always showing a fresh perspective on physical phenomena.

Thank you, Prof. Piotr Wasylczyk, for your wise words and for your help in preparing the NISE manuscript – thanks to your advice, I became confident in writing.

And thank you, Jakub Lewandowski, for all the sweets, cakes, ideas, and for being open to discuss and listen.

Another group of people who significantly increased my happiness during the

PhD are my colleagues from the Nencki Institute of Experimental Biology. Thank you, Łukasz Bijoch, Justyna Wiśniewska, and Anna Beroun, for sharing your knowledge in such an understandable way, for being open to my physics-driven perspective, and for always being willing to help. Thank you, Aleksandra Mielnicka, for assisting with sample preparation despite your tight schedule, and Urszula Szachowicz for always being exceptionally kind and professional.

I want to sincerely thank Benjamin Judkewitz for generously sharing the TPSM design. The whole project with the Nencki Institute of Experimental Biology was possible thanks to him.

I also want to express my gratitude to Prof. Artur Bednarkiewicz and Dr Katarzyna Prorok from the Institute of Low Temperature and Structure Research of the Polish Academy of Sciences for sharing the avalanching particles and for synthesising a tremendous amount of different samples to make NISE work.

Next, I would like to mention my students from the Interdisciplinary Club for Tournaments and Competitions, with whom it was a joy to work. Leading the team for the International Physicists' Tournament was one of the most rewarding experiences of my life. Thank you: Kamil Dutkiewicz, Kuba Trzaska, Michał Zdziennicki, Stasiek Rakowski, Tomasz Mazur, Jakub Hevler, Paweł Kałwak, Debora Choińska, Kuba Grabarczyk, Michał Świątek, Nina Mitroczuk, Jakub Schindler, Małgorzata Flis, Igor Nowik, Maciej Szyszko, Jakub Kośmicki, Magdalena Orłowska, Sara Gałan, Piotr Łukawski, Wiktor Kondrusiewicz, and Michał Puza – for showing me how hard work on physics problems can be both rewarding and genuinely fun.

Last but certainly not least, I want to thank my family. Thank you to my parents for always being supportive and never judgmental. Thank you to my uncle Władek for the simple yet powerful advice to write at least one hour every day – advice that turned out to be incredibly effective.

And above all, I am profoundly grateful to my wife. Thank you for being by my side through every phase of this PhD – for your patience, your strength, your warmth, and your unwavering belief in me. Thank you for every moment of calm you brought into the chaos, for project management, for every encouraging word, for every sacrifice – big and small – that made this work possible. You were my anchor, my companion, my balance, and my source of joy throughout these years.

Thank you not only for being the perfect wife and girlfriend on this journey, but also for becoming the wonderful mother of Hania, to whom I am also grateful, for giving me the strongest motivation to finish this thesis.

Funding

This research was supported by multiple funding agencies whose contributions are gratefully acknowledged. The work was funded by the Foundation for Polish Science under the FIRST TEAM project "Spatiotemporal photon correlation measurements for quantum metrology and super-resolution microscopy" (POIR.04.04.00-00-3004/17-00) and the FIRST TEAM grant FENG.02.02-IP.05-0253/23. Additional support was provided by the National Science Centre, Poland, through grant 2022/47/B/ST7/03465.

This work also benefited from the QuantERA II ERA-NET Cofund in Quantum Technologies via the projects QM3 (QuantERAII/02/QM3/03/2024) and EXTRASENS (QuantERAII/02/EXTRASENS/02/2024). Further financial support came from the Horizon Europe Marie Skłodowska-Curie Actions (project FLORIN, ID 101086142).

I also gratefully acknowledge the infrastructural and organisational support of the Narodowe Laboratorium Fotoniki i Technologii Kwantowych (NLPQT), which provided essential research facilities enabling the experimental work presented in this thesis.

Auxiliary information

List of Publications:

- **Pawel Szczypkowski**, Monika Pawłowska, Radek Lapkiewicz, "3D Super-resolution Optical Fluctuation Imaging with Temporal Focusing Two-photon Excitation," Biomedical Optics Express (2024)
  The author introduced the idea, built the experimental setup, prepared the samples (staining with q-dots), performed the experiments and data analysis, prepared the manuscript with RL.

- Lukasz Bijoch, **Pawel Szczypkowski**, Justyna Wiśniewska, Monika Pawłowska, Karolina Hajdukiewicz, Radek Lapkiewicz, Anna Beroun, "Opposing effects of rewarding and aversive stimuli on D1 and D2 types of dopamine-sensitive neurons in the central amygdala". bioRxiv (2024)
  The author, together with MP, constructed and tested the two-photon microscope. Together with LB, I prepared the experimental control and synchronisation. Reviewed the manuscript.

- Adrian Makowski, Wojciech Zwoliński, **Pawel Szczypkowski**, Bernard Gorzkowski, Sylvain Gigan, Radek Lapkiewicz, "Low Photon Number Non-Invasive Imaging Through Time-Varying Diffusers", Arxiv (2025)
  The author provided key input on constructing the experimental platform, contributed to data acquisition and development of the theory, and wrote the supplementary section detailing the experimental setup.

- **Pawel Szczypkowski**, Adrian Makowski, Wojciech Zwoliński, Katarzyna Prorok, Piotr Wasylczyk, Artur Bednarkiewicz, Radek Lapkiewicz, "Overcoming light scattering with high optical nonlinearity", Arxiv (2025) *The author designed and constructed the experimental setup, performed the experiment, analysed the data, managed the manuscript preparation, prepared the manuscript figures, and the text.*

- Sanjukta Kundu, Balakrishnan Viswanathan, **Pawel Szczypkowski**, Gabriela Barreto Lemos, Radek Lapkiewicz, and Mayukh Lahiri, "Verification of continuous variable entanglement with undetected photons," In preparation (2025)
  The author contributed to the experiment, data presentation and interpretation, manuscript writing and prepared schematic figures.

List of Conferences:

- Integrated Optics - Sensors, Sensing Structures, and Methods - IOS'2022, oral presentation: "Towards two-photon bio-imaging with GRIN lenses and image guides"
- Focus on Microscopy 2022 (Online), poster and flash poster (pre-recorded short presentation): "Temporal focusing for Super-resolution Optical Fluctuation Imaging (SOFI) in thick samples"
- Polska Konferencja Optyczna 2022 (Polish Optical Conference), oral presentation: "Ogniskowanie czasowe impulsów dla super-rozdzielczej mikroskopii dwufotonowej" ("Temporal focusing for super-resolution, two-photon microscopy")
- Focus on Microscopy 2023, poster "3D-bio wide-field imaging in epi-geometry"
- Neurons in Action 2023, poster: "Easy 3D imaging using SOFI and temporal focusing"
- Polska Konferencja Optyczna 2023 (Polish Optical Conference), oral presentation "Nadrozdzielcza Dwufotonowa Mikroskopia 3D" ("Super-resolution two-photon 3D Microscopy")
- Focus on Microscopy 2025, oral presentation: "High-nonlinearity-enabled direct non-invasive imaging through scattering layers"
- Polska Konferencja Optyczna 2025 (Polish Optical Conference), oral presentation "Obrazowanie przez ośrodki rozpraszające dzięki wysokiej nieliniowości optycznej" ("Imaging through scattering media with high optical nonlinearity")

Awards and Scholarships During the PhD

- 2021-2023, Research scholarship in the project "Spatiotemporal photon correlation measurements for quantum metrology and super-resolution microscopy", financed by the Foundation for Polish Science
- 2023-2024 Research scholarship in the project "Super-resolution imaging in scattering media based on fluorescence intensity correlations" financed by the National Science Center
- 2025 - Research scholarship in the project "Spatiotemporal light manipulation for microscopy and photon counting cameras", financed by the Foundation for Polish Science
- 4th place in the International Physics Tournament 2022 (Team Leader)
- 1st place in the International Physics Tournament 2023 (Team Leader)
- 5th place in the International Physics Tournament 2024 (Team Leader)

- 5th place in the International Physics Tournament (Team Leader)
- Dean's Award of the Faculty of Physics, University of Warsaw, for outstanding performance in teaching laboratory classes "General Physics Laboratory I R" (academic year 2023/2024).
- Best Student Oral Presentation Award, Polish Optical Conference 2025

Software and AI tools used

Data acquisition and analysis were performed mostly using Python, mainly using packages NumPy, SciPy, and Matplotlib (IDEs: Google Colaboratory, Spyder, VS Code). Images were prepared either with Matplotlib Python or with ImageJ. Results from chapter 4 (SOFI calculation) were obtained with scripts in Matlab based on [114]. Figure 3.3 was prepared with Autodesk Inventor 2025 Pro using students/educational license.
Figures were prepared in Inkscape.
The text was written in LaTeX using Overleaf.
Generative AI tools (OpenAI GPT-5) were used for grammar verification, LaTeX formatting and debugging, and improving stylistic clarity. The latex template was based on the PhD thesis of Nathalie Nagl: "A New Generation of Ultrafast Oscillators for Mid-Infrared Applications" (2020) supervised by Prof. Dr. Ferenc Krausz and Prof. Dr. Ursula Keller. I used this thesis also as an inspiration for the structure of my thesis (e.g. including sections: Thesis outline, or Closing remarks).

All scientific reasoning, data interpretation, and conclusions were developed independently by me. All conceptual content, theoretical derivations, experimental results, and data interpretations presented in this thesis are my original work if not credited. The AI tools were used under my supervision and did not contribute to the scientific findings or conclusions. OpenAI GPT-5 was acquainted with my writing style (via bachelor's, master's thesis and publications). Then I wrote the text in a loose structure with sentences describing the merit of the information I wanted to convey. This created a detailed, sentence-by-sentence outline of every section of the thesis. I generated (with OpenAI GPT-5) the coherent version of the text based on this outline I wrote. Next, I refined the text by rewriting, adding or removing sentences (most of the text changed). In the end, I used Grammarly to improve the text's correctness further. I find such use of generative AI advantageous for scientific writing, as more effort and pressure are placed on the merit – the information – than on the style of writing.

Declaration of Authorship

I, **Paweł Szczypkowski**,
hereby declare that the doctoral thesis entitled

"Spatiotemporal Light Manipulation for Nonlinear Microscopy"

is my own original work. All sources and contributions by others have been properly acknowledged. No part of this thesis has been submitted for another degree or qualification at this or any other institution.

Ja, **Paweł Szczypkowski**,
oświadczam że rozprawa doktorska pt.

"Spatiotemporal Light Manipulation for Nonlinear Microscopy"

została napisana przeze mnie samodzielnie. Wszystkie źródła i wkład innych osób zostały wskazane. Praca nie była przekładana w celu uzyskania innego stopnia lub tytułu.

Date/Data: _____ Signature/Podpis: _____

Paweł Szczypkowski